ornl

ORNL/TM-9673

OAK RIDGE NATIONAL LABORATORY

MARTIN MARIETTA

CERAMIC TECHNOLOGY FOR ADVANCED HEAT ENGINES PROJECT SEMIANNUAL PROGRESS REPORT FOR PERIOD OCTOBER 1984–MARCH 1985

Prepared for
U.S. Department of Energy
Assistant Secretary for Conservation and Renewable Energy
Office of Transportation Systems
Advanced Materials Development Program

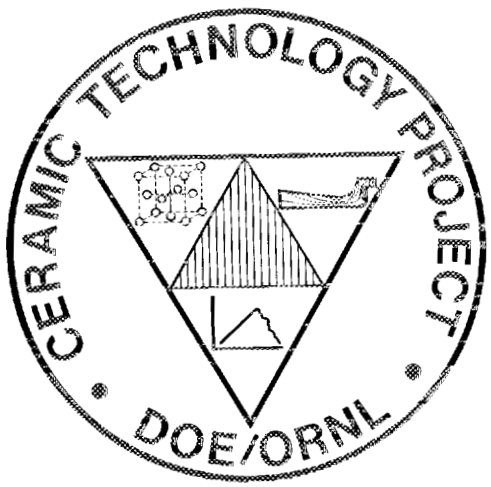

OPERATED BY
MARTIN MARIETTA ENERGY SYSTEMS, INC.
FOR THE UNITED STATES
DEPARTMENT OF ENERGY

Available from the National Technical Information Service
U.S. Department of Commerce
5285 Port Royal Road, Springfield, VA 22161
NTIS price codes—Printed Copy: A04 Microfiche A01

ORNL/TM-9673

METALS AND CERAMICS DIVISION

CERAMIC TECHNOLOGY FOR ADVANCED HEAT ENGINES PROJECT SEMIANNUAL PROGRESS REPORT FOR PERIOD OCTOBER 1984–MARCH 1985

D. R. Johnson
Project Manager

Date of Publication: September 1985

Prepared for
U.S. Department of Energy
Assistant Secretary for Conservation and Renewable Energy
Office of Transportation Systems
Advanced Materials Development Program

Prepared by the
OAK RIDGE NATIONAL LABORATORY
Oak Ridge, Tennessee 37831
operated by
MARTIN MARIETTA ENERGY SYSTEMS, INC.
for the
U.S. DEPARTMENT OF ENERGY
under Contract No. DE-AC05-84OR21400

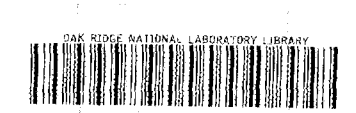

CONTENTS

SUMMARY

The Ceramic Technology For Advanced Heat Engines Project was developed by the Department of Energy's Office of Transportation Systems (OTS) in Conservation and Renewable Energy. This project, part of the OTS's Advanced Materials Development Program, was developed to meet the ceramic technology requirements of the OTS's automotive technology programs.

Significant accomplishments in fabricating ceramic components for the Department of Energy (DOE), National Aeronautics and Space Administration (NASA), and Department of Defense (DOD) advanced heat engine programs have provided evidence that the operation of ceramic parts in high-temperature engine environments is feasible. However, these programs have also demonstrated that additional research is needed in materials and processing development, design methodology, and data base and life prediction before industry will have a sufficient technology base from which to produce reliable cost-effective ceramic engine components commercially.

An assessment of needs was completed, and a five-year project plan was developed with extensive input from private industry. The objective of the project is to develop the industrial technology base required for reliable ceramics for application in advanced automotive heat engines. The project approach includes determining the mechanisms controlling reliability, improving processes for fabricating existing ceramics, developing new materials with increased reliability, and testing these materials in simulated engine environments to confirm reliability. Although this is a generic materials project, the focus is on structural ceramics for advanced gas turbine and diesel engines, ceramic bearings and attachments, and ceramic coatings for thermal barrier and wear applications in these engines. This advanced materials technology is being developed in parallel and close coordination with the ongoing DOE and industry proof-of-concept engine development programs. To facilitate the rapid transfer of this technology to U.S. industry, the major portion of the work is being done in the ceramic industry, with technological support from government laboratories, other industrial laboratories, and universities.

This project is managed by ORNL for the Office of Transportation Systems, Heat Engine Propulsion Division, and is closely coordinated with complementary ceramics tasks funded by other DOE offices, NASA, DOD, and industry. A joint DOE and NASA technical plan has been established, with DOE focus on automotive applications and NASA focus on aerospace applications. A common work breakdown structure (WBS) was developed to facilitate coordination. The work described in this report is organized according to the following WBS project elements:

0.0 Management and Coordination

1.0 Materials and Processing

- 1.1 Monolithics
- 1.2 Ceramic Composites
- 1.3 Thermal and Wear Coatings
- 1.4 Joining

2.0 Materials Design Methodology

- 2.1 Modeling
- 2.2 Contact Interfaces
- 2.3 New Concepts

3.0 Data Base and Life Prediction

- 3.1 Structural Qualification
- 3.2 Time-Dependent Behavior
- 3.3 Environmental Effects
- 3.4 Fracture Mechanics
- 3.5 NDE Development

4.0 Technology Transfer

- 4.1 Technology Transfer

This report includes contributions from all currently active project participants. The contributions are arranged according to the WBS outline.

0.0 PROJECT MANAGEMENT AND COORDINATION

D. R. Johnson
Oak Ridge National Laboratory

Objective/scope

This task includes the technical management of the project in accordance with the project plans and management plan approved by the Department of Energy (DOE) Oak Ridge Operations Office (ORO) and the Office of Transportation Systems. This task includes preparation of annual field task proposals, initiation and management of subcontracts and interagency agreements, and management of ORNL technical tasks. Monthly management reports and bimonthly reports are provided to DOE; highlights and semiannual technical reports are provided to DOE and program participants. In addition, the program is coordinated with interfacing programs sponsored by other DOE offices and federal agencies, including the National Aeronautics and Space Administration (NASA) and the Department of Defense (DOD). This coordination is accomplished by participation in bimonthly DOE and NASA joint management meetings, annual interagency heat engine ceramics coordination meetings, DOE contractor coordination meetings, and DOE Energy Materials Coordinating Committee (EMaCC) meetings, as well as special coordination meetings.

Technical progress

A computer data base and milestone commitment system have been developed for the program. The purpose of the data base is to facilitate program management and coordination. Each task in the Ceramic Technology Project is described by 44 attributes, which include WBS element, project name, responsible organization, program manager, principal investigator, objective, contract number, funding by year, technical monitor, period of performance, milestones, and milestone performance. The data base is stored in ORNL's Digital Equipment Corporation PDP-10 computer and is available to the project manager via a terminal in his office.

The milestone commitment system is part of the data base. It facilitates tracking of milestones by management, and communication between the principal investigators and the project manager with respect to the milestones. Milestones in the Ceramic Technology Project are initiated by the program participants for approval by the project office. The milestones are usually submitted to the project as a contractual requirement soon after a subcontract is signed.

To assure that the principal investigator (PI) understands and accepts his milestones, for each milestone a computer-generated letter is sent to the PI asking for his acceptance. Figure 1 shows a sample milestone acceptance letter. The letter is signed by the PI and returned to the project office. The PI's concurrence is logged into the data base and the letter kept in the contract file.

OAK RIDGE NATIONAL LABORATORY
Operated by Martin Marietta Energy Systems, Inc.

Post Office Box X
Oak Ridge, Tennessee 37831
Nov-09-1984

D. R. Richerson
Garrett Turbine Engine Co.
111 South 34th ST
Phoenix, AZ 85010

Dear D. R. Richerson

Subject: CERAMIC TECHNOLOGY FOR ADVANCED HEAT ENGINE PROJECT

Milestone: 2.2.1
Complete Task 2, strength of baseline and coated specimens.

The proposed completion date for the milestone listed above is Sep-30-1985. A status inquiry letter will be sent to you periodically until the milestone is completed. Please acknowledge this letter as indicated below and return the original of the letter to me.

Sincerely,

D. R. Johnson
Manager, Ceramic Technology Project
Oak Ridge National Laboratory
Post Office Box X
Building 4508, M/S 113
Oak Ridge, Tennessee 37831
Telephone : (615)-576-6832

Acknowledgment:

_____
Signature Date

Fig. 1. Sample milestone acceptance letter.

Once a milestone has been acknowledged, a computer-generated letter is periodically sent inquiring about the status of the milestone. The frequency of the status inquiry letters varies from quarterly to monthly, depending on the time period before the milestone due date. If the expected progress toward the milestone is on schedule, the PI can check "on schedule" and sign and return the letter. If the milestone has been completed, the PI can check "completed" and cite the periodic or topical report in which the results are published. If a problem in meeting the milestone on time is anticipated, the PI can explain and request a deferral of the due date. Once the completed milestone status letter is received by the project office, the indicated status is logged in and the letter filed. Subsequent milestone status inquiry letters include a record of the previous responses by the PI. Figure 2 is a sample milestone status inquiry letter.

The milestone data can be sorted in several ways (such as milestone due date, responsible organization, or WBS number) and reports generated by the computer.

OAK RIDGE NATIONAL LABORATORY
Operated by Martin Marietta Energy Systems, Inc.

Post Office Box X
Oak Ridge, Tennessee 37831
Nov-09-1984

D. R. Richerson
Garrett Turbine Engine Co.
111 South 34th ST
Phoenix, AZ 85010

Dear D. R. Richerson

Subject: CERAMIC TECHNOLOGY FOR ADVANCED HEAT ENGINE PROJECT

Milestone: 2.2.1
Complete Task 2, strength of baseline and coated specimens.

The completion date for the milestone listed above is Sep-30-1985. Please indicate the status, sign and return the original of the letter to me.

Sincerely,

D. R. Johnson
Manager, Ceramic Technology Project
Oak Ridge National Laboratory
Post Office Box X
Building 4508, M/S 113
Oak Ridge, Tennessee 37831
Telephone : (615)-576-6832

PREVIOUS COMMENTS:

STATUS:	DATE	REPORT NUMBER	COMMENTS
COMPLETED	_____	_____	_____
ON SCHEDULE	_____	_____	_____
OTHER (EXPLAIN)	_____		

_____
Signature Date

Fig. 2. Sample milestone status inquiry letter.

1.0 MATERIALS AND PROCESSING

INTRODUCTION

This portion of the project is identified as project element 1.0 within the work breakdown structure (WBS). It contains four subelements: (1) Monolithics, (2) Ceramic Composites, (3) Thermal and Wear Coatings, and (4) Joining. Ceramic research conducted within the Monolithics subelement currently includes work activities on green state ceramic fabrication, characterization, and densification and on structural, mechanical, and physical properties of these ceramics. Research conducted within the Ceramic Composites subelement currently includes silicon carbide and oxide-based composites, which, in addition to the work activities cited for Monolithics, include fiber synthesis and characterization. Research conducted in the Thermal and Wear Coatings subelement is currently limited to oxide-base coatings and involves coating synthesis, characterization, and the determination of the mechanical and physical properties of the coatings. Research conducted in the Joining subelement currently includes studies of processes to produce strong stable joints between zirconia ceramics and iron-base alloys.

A major objective of the research in the Materials and Processing project element is to systematically advance the understanding of the relationships between ceramic raw materials such as powders and reactant gases, the processing variables involved in producing the ceramic materials, and their resultant microstructures and physical and mechanical properties. Success in meeting this objective will provide U.S. companies with new or improved ways for producing economical highly reliable ceramic components for advanced heat engines.

1.1 MONOLITHICS

1.1.1 Silicon Carbide

Silicon Carbide Powder Synthesis and Characterization
M. A. Janney and L. A. Harris (Oak Ridge National Laboratory)

This effort is currently being supported under the task "Materials for Waste Heat Utilization," which is sponsored by the Office of Industrial Programs, Conservation and Renewable Energy. A final report on this subject was issued. (M. A. Janney, G. C. Wei, C. R. Kennedy, and L. A. Harris, *Carbothermal Synthesis of Silicon Carbide*, ORNL-6169, May 1985.)

Synthesis of High-Purity Sinterable Silicon Carbide (SiC) Powders

J. M. Halstead and V. Venkateswaren [SOHIO Engineered Materials Company (Carborundum)] and B. L. Mehosky (SOHIO Research and Development)

Objective/Scope

The objective of this program is to develop a volume scaleable process to produce high purity, high surface area sinterable silicon carbide powder.

The program is organized in two phases. Phase I includes the following elements:

- Verify the technical feasibility of the gas phase synthesis route.
- Identify the best silicon feedstock on the basis of performance and cost.
- Optimize the production process at the bench scale.
- Fully characterize the powders produced and compare with commercially available alternatives.
- Develop a theoretical model to assist in understanding the synthesis process, optimization of operating conditions and scale-up.

Phase II, when authorized, will scale the process to 5-10X the bench scale quantities in order to perform confirmatory experiments, produce process flowsheets and to perform economic analysis.

Technical Highlights

Background, Organization and Workplan

Background - The Gas Phase Synthesis Route

Given the objective of producing a submicron silicon carbide powder purer and with more controllable properties than could be produced via the Acheson process, Sohio-Carborundum evaluated three candidate process routes:

1) Sol-Gel
2) Polymer Pyrolysis
3) Gas Phase Reactions.

A gas phase route utilizing plasma heating was chosen as having the most proven technology, the highest product yield and good scaleability potential.

Further, Carborundum had previously sponsored proprietary research in gas phase synthesis and had demonstrated the feasibility of the approach.

Organization

The program is managed by the Structural Ceramics Division of Sohio Engineered Materials Company (Carborundum) which acts as the subcontractor. Technical direction comes from Sohio-Carborundum's Niagara Falls R&D Center and on-site resources are provided by Sohio's (Warrensville) R&D Center.

Program management is accomplished via continuous dialogue among the parties. Outside resources are utilized where appropriate to strengthen the program. Existing subcontractors include Plasma Materials, Inc. (plasma torch) and International Plasma Engineering, Inc. (theoretical modeling).

Analytical services are available both in Niagara Falls and Warrensville.

Workplan

A breakdown of major tasks and milestones is shown in Figure 1. Subtasks have been developed for Task 4 - Screening Experiments and will be developed for Task 5 - Extended Parametric Studies.

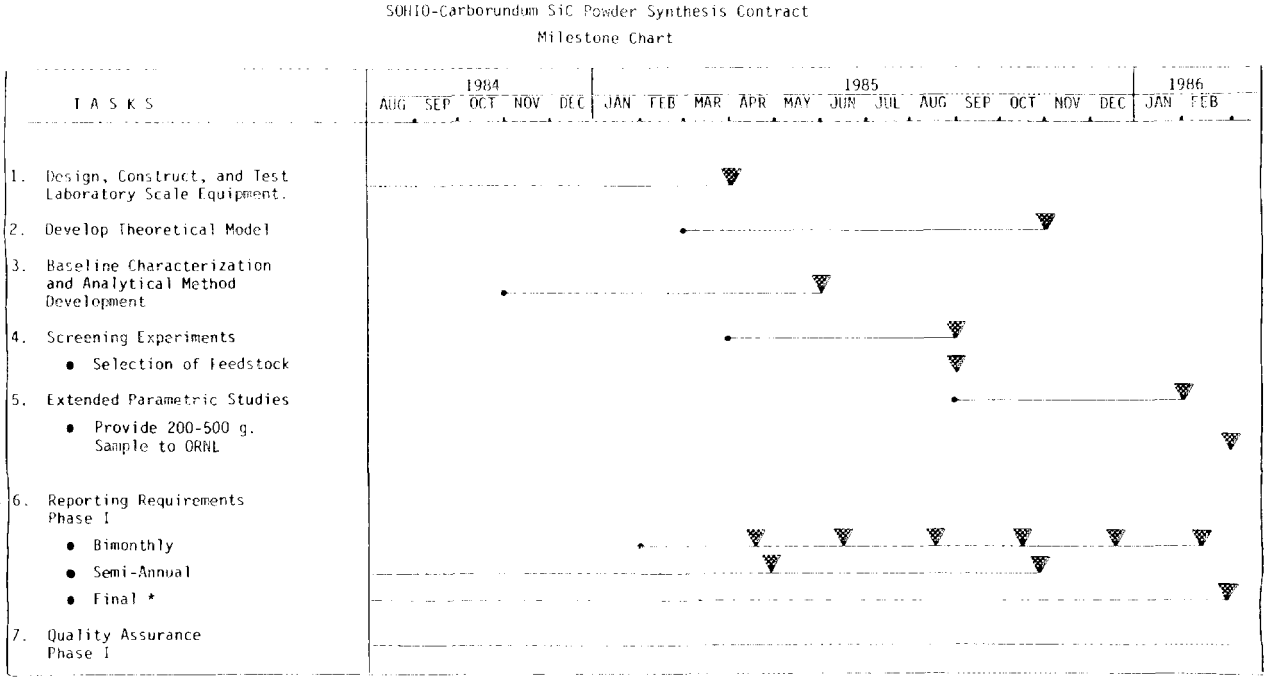

* Only required if decision is made not to go on to Phase II.

Revised 3/15/85

Figure 1. Milestone Chart

Task 1. Design, Construct and Test Laboratory Scale Equipment.

The Sohio Research and Development Center at Warrensville, Ohio was chosen as the site for the laboratory scale gas phase synthesis system due to the ready availability of applicable engineering and technical resources. The proximity to other related research which is being performed by Sohio on behalf of Sohio-Carborundum's structural ceramics effort was also a factor.

The design phase involved a complete review of the preliminary conceptual design and specifying appropriate subsystems in order to evaluate and control critical process parameters.

The conceptual design is shown in Figure 2.

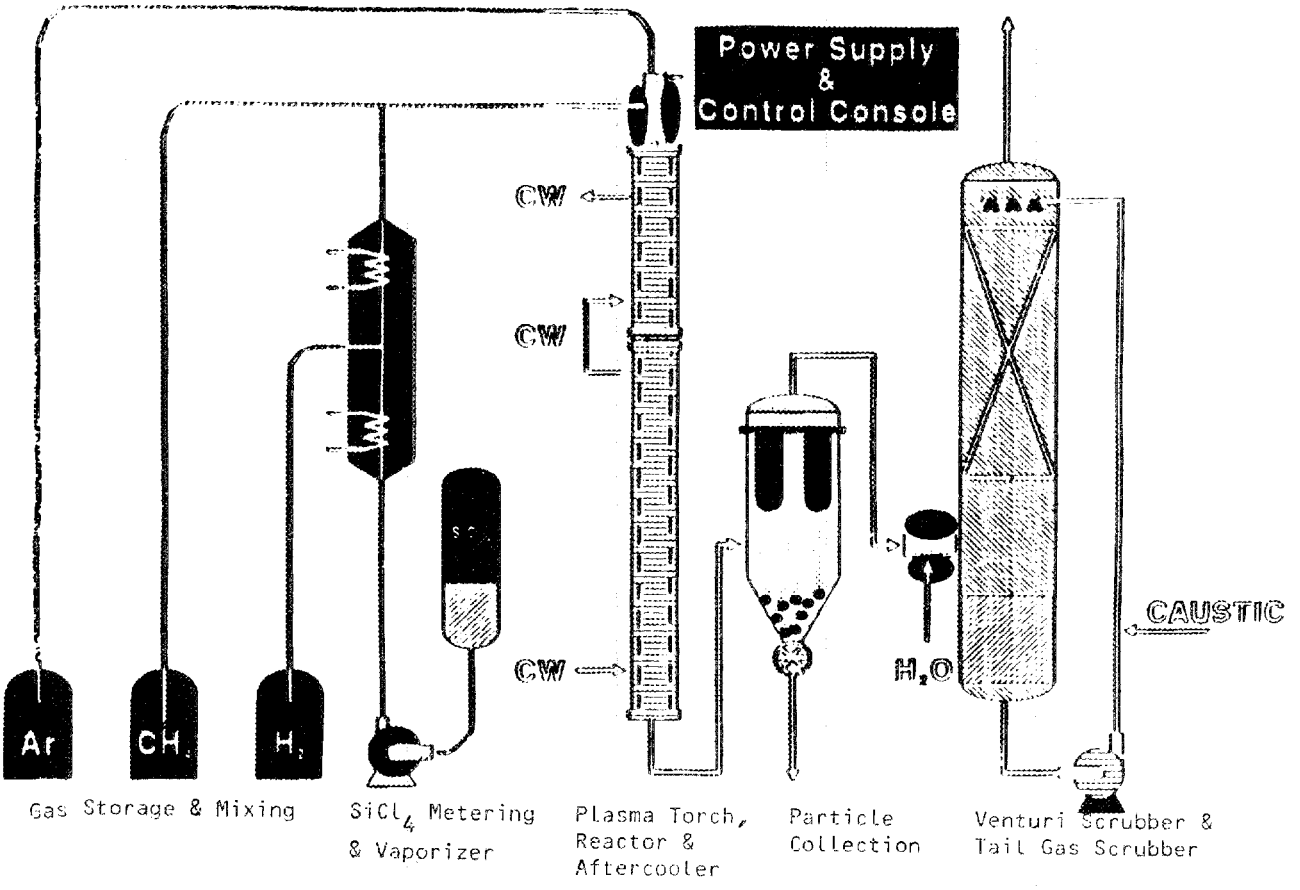

Figure 2. Conceptual Design and Simplified Process Flow Chart

The process involves using a plasma torch to instantaneously heat silicon and carbon containing gases such as silicon tetrachloride ($SiCl_4$) and methane (CH_4) and reacting them to form SiC. The hydrogen gas then acts as a scavenger for the chlorine and forms hydrochloric acid (HCl) which is removed in the scrubber.

Particle collection methods will be investigated in Phase I and the best choice will be implemented for Phase II.

The following issues were identified and evaluated in the design of the system.

- Gas and feedstock delivery train.
  - o Capacity
  - o Automatic shutdown system
  - o Purging capability
- Reactant vaporizer/gas mixing unit.
  - o Preheat of gases
  - o Atomizing nozzle
- Plasma generator and instrumentation.
  - o Temperature control
  - o Variable geometry capability
  - o Maximization of electrical efficiency
  - o Argon/hydrogen operation considerations
- Reactor and aftercooler.
  - o Aspect ratio
  - o Cooling capability
  - o Reactant introduction
  - o Hydrodynamic considerations
- Product collector and off-gas scrubber.
  - o Neutralization capability
  - o Collection efficiency
  - o Pressure drop

Once the design of the system and its components was complete, site preparation and sourcing of components was initiated.

The key subsystems are as follows:

Plasma Torch Subsystem

- Torch
- Rectifier/Power Supply
- Reactor Vessel

Gas and Silicon Supply Subsystem	Hydrogen	Argon	Methane
- Primary Gas	X	X	
- Secondary Gas	X	X	
- Tertiary Gas	X		X
- Auxiliary Gas Stream			
- Silicon Source Metering and Vaporizer			

Control and Data Acquisition Subsystem

- Gas Flow Control
- Power Control
- Data Acquisition

Downstream Subsystem

- Particle Collection
- Effluent Collection/Treatment

Figure 3 shows the plot plan for the laboratory scale equipment, while Figure 4 is a photographic overview.

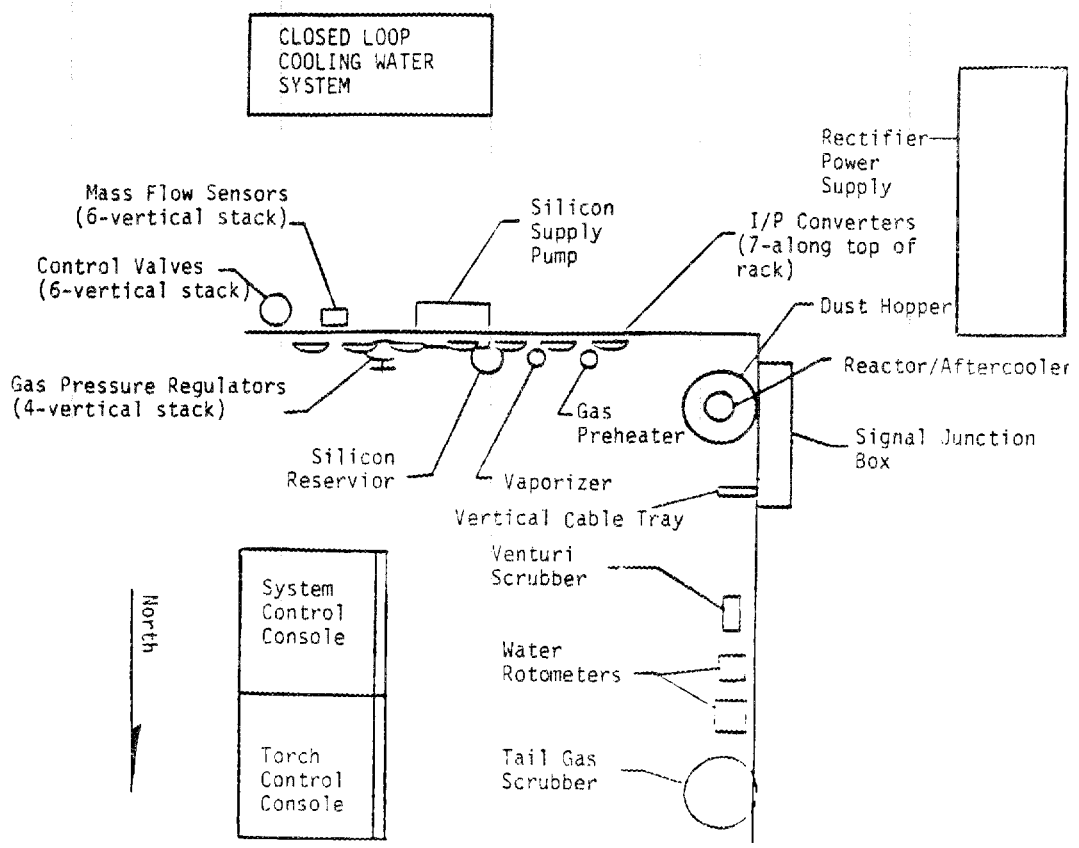

Figure 3. Plot Plan for Laboratory Scale System

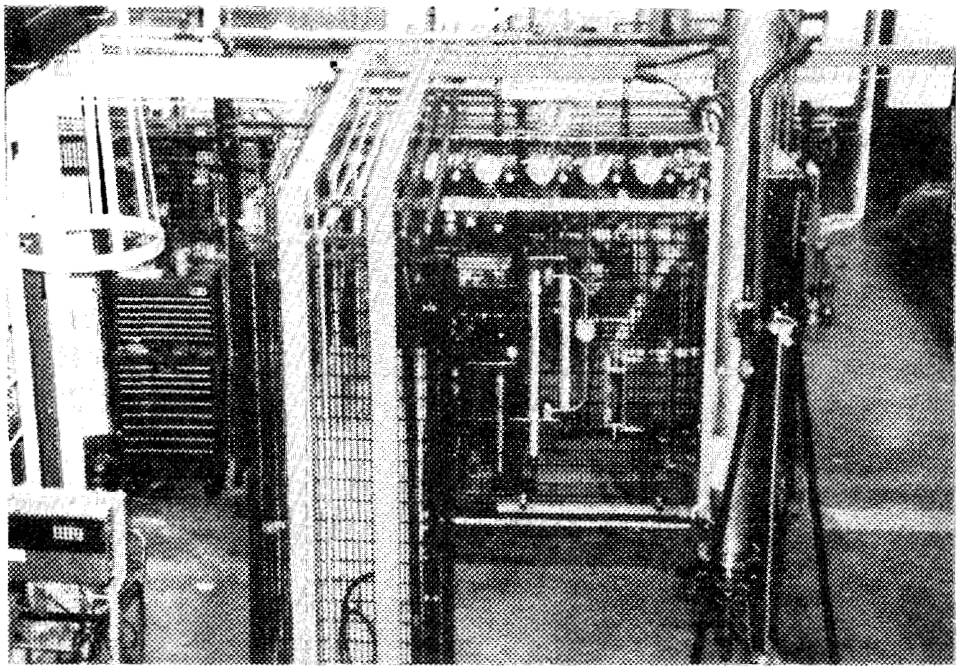

Figure 4. Photographic Overview of Laboratory Scale System

Plasma Torch Subsystem

The heart of the system is the plasma torch. This was obtained from Plasma Materials Inc. with whom Sohio-Carborundum has previously worked. The torch is rated at 50KW. This is significantly higher than required for this application, but the unit has excellent turn-down capability and will be sufficient for future scale-up. It is installed atop the reactor vessel which is constructed of copper and wrapped with copper tubing in which the cooling water flows. Thermocouples are installed along the entire length of the reactor.

The DC power supply has a 120KW nameplate rating. A simple thimble type collector with an isolation valve is affixed to the lower end of the reactor. Alternative powder collection techniques will be evaluated in preparation for Phase II scale-up.

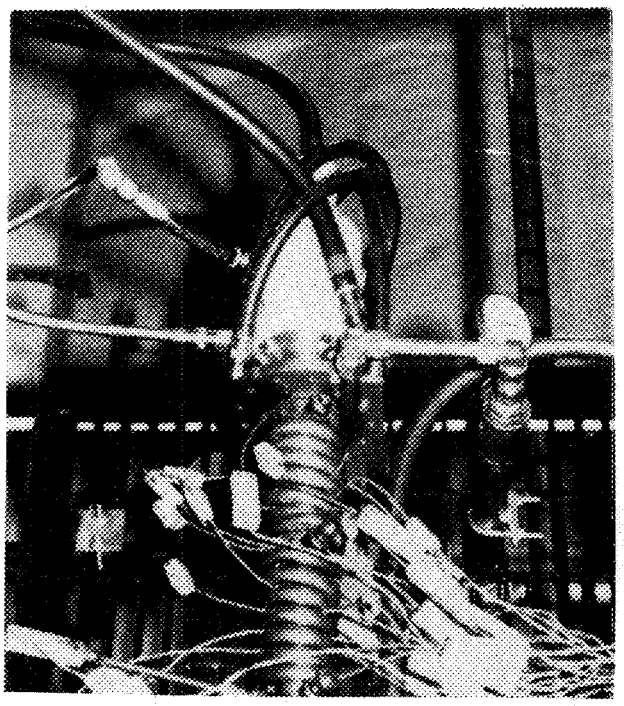

Figure 5. Plasma Torch Atop Water Cooled Reactor

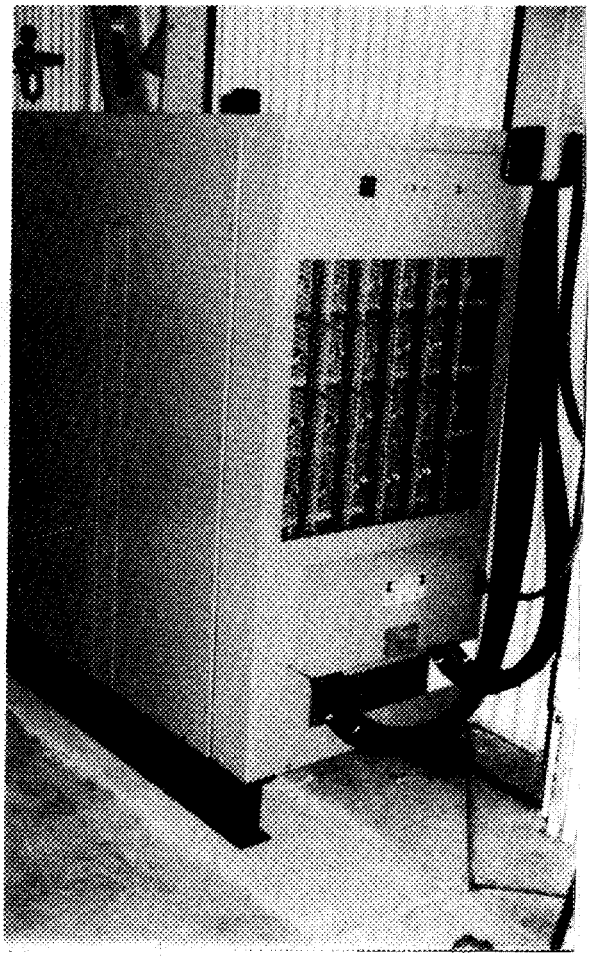

Figure 6. Rectifier/Power Supply for Plasma Torch

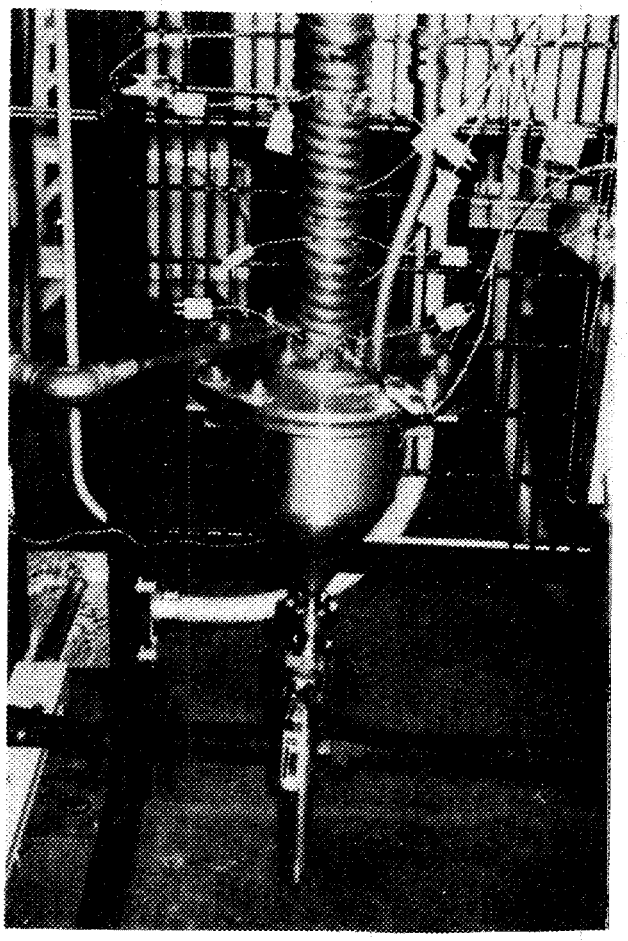

Figure 7. Exit End of Reactor with Simple Thimble Collector and Isolation Valve

Gas and Silicon Supply Subsystem

Piping and controls for primary, secondary and tertiary gas streams (hydrogen, argon and methane) are installed. An additional gas stream may be metered into either primary or secondary gas streams.

The silicon source is introduced to the system through the vaporizer and combined with the reactant gases prior to entering the reactor.

Figure 8 shows the gas and silicon supply subsystem.

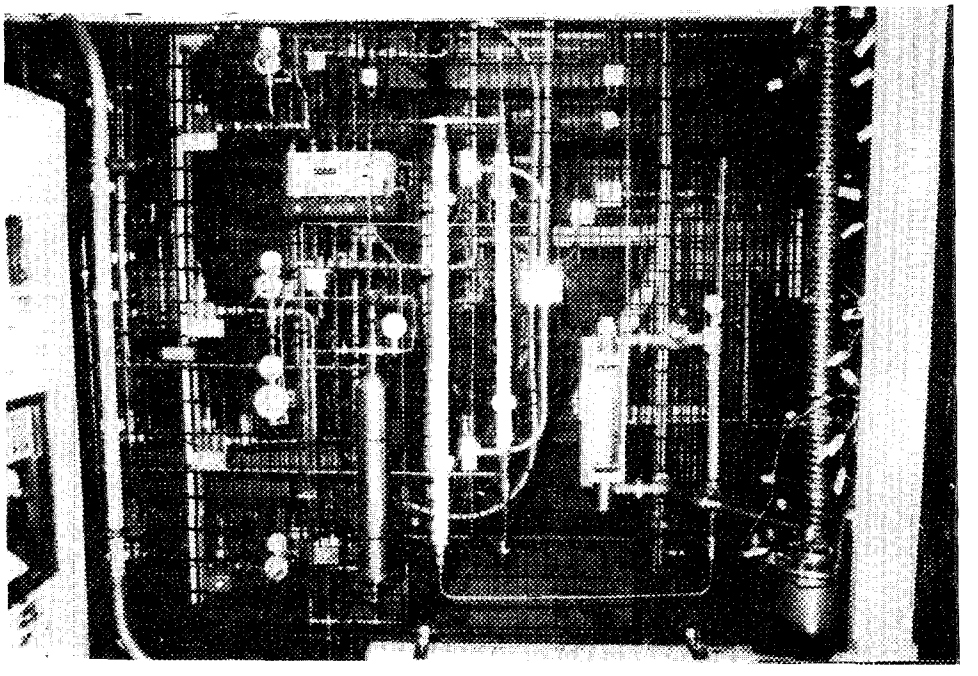

Figure 8. Gas and Silicon Supply Subsystem

Control and Data Acquisition Subsystem

The Control and Data Acquisition Consoles are shown in Figure 9. The torch control (on left) was designed and supplied by the torch manufacturer, Plasma Materials, Inc.

The System Control Console was designed and assembled by Sohio. The system control includes flow control (mass flow), power control, and a data logger capable of 32 data points logged every two seconds.

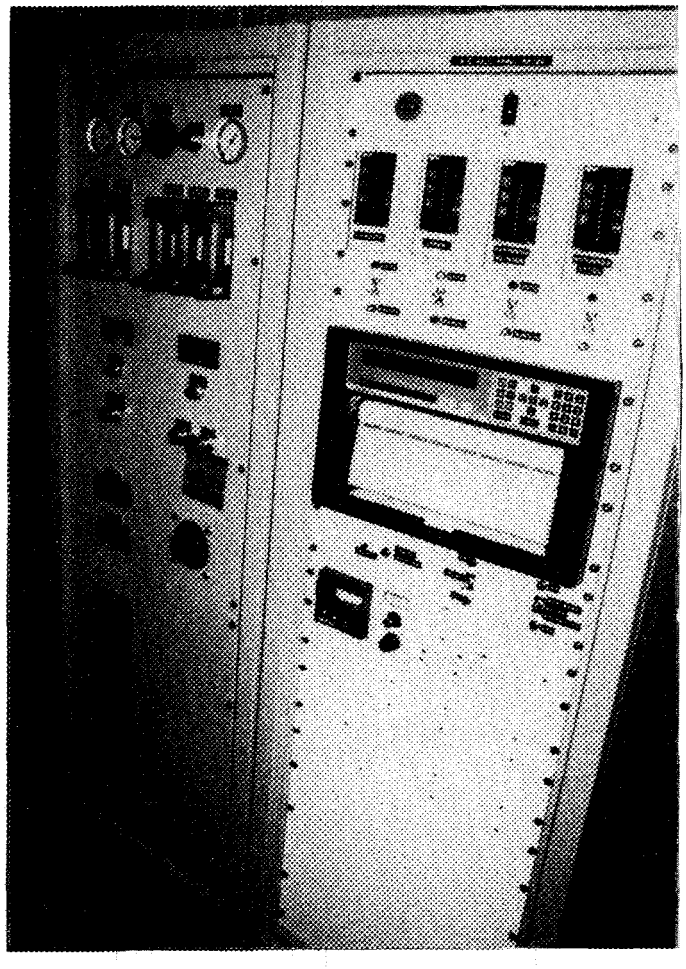

Figure 9. Control Console. Left, Torch Control; Right, System Control

Downstream Subsystem

Particle collection has not yet been defined. Investigation of various schemes will be done during Phase I in preparation for the installation of the "best" system for Phase II scale-up.

Reaction effluent, HCl in particular, is routed through venturi and tail gas scrubbers as shown in Figure 10.

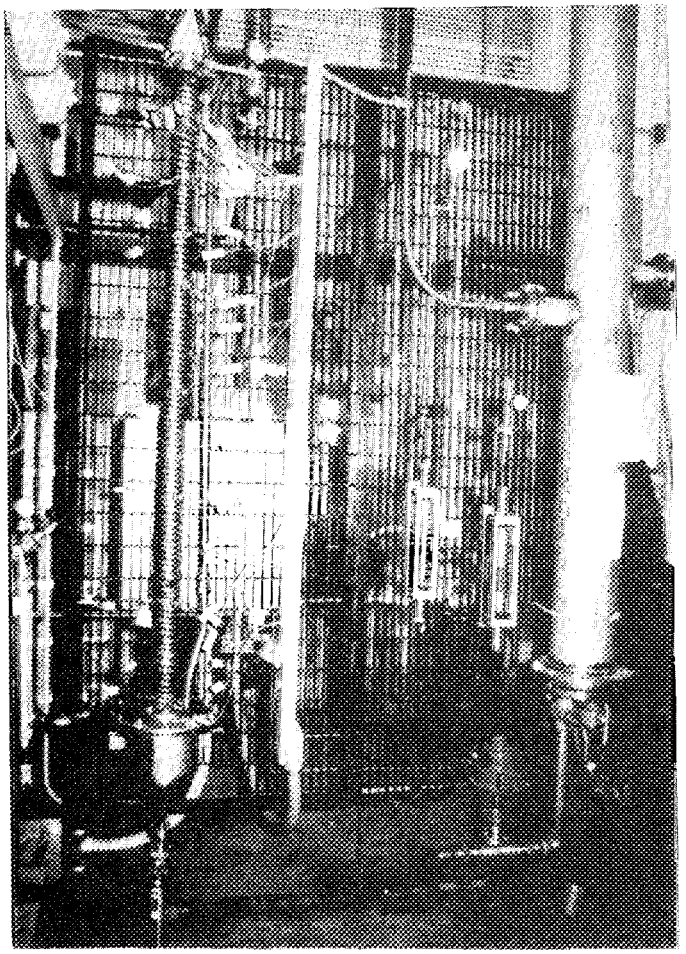

Figure 10. Portion of Module Showing Reactor (left) and Tail Gas Scrubber (right)

Cooling water for the reactor is recirculated utilizing the heat exchanger shown in Figure 11, and ultimately is used by and drained from the tail gas scrubber.

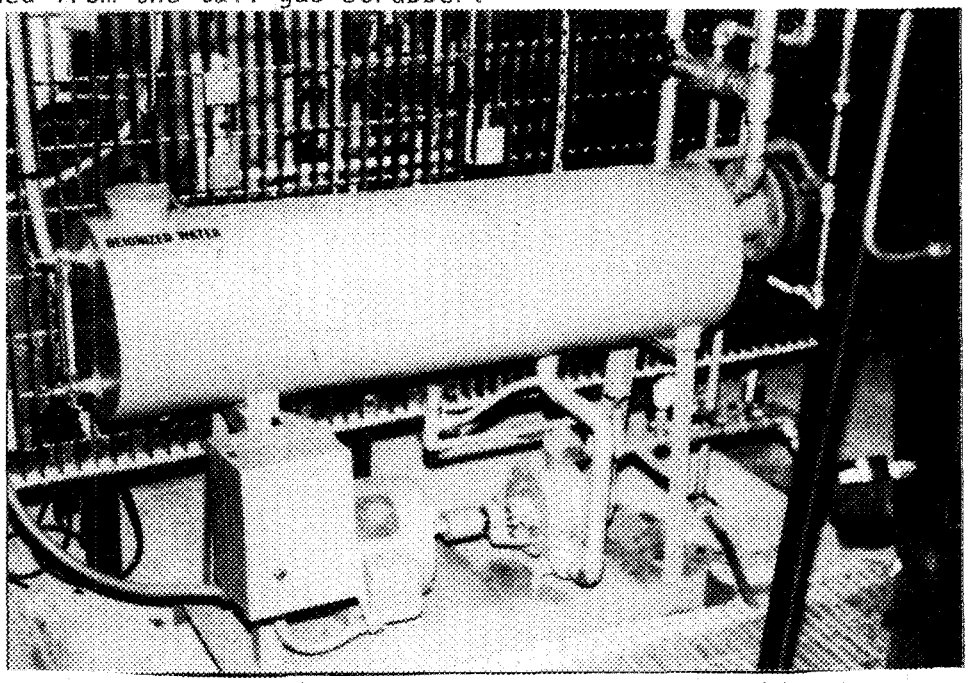

Figure 11. Heat Exchanger for Recycling Loop of Reactor Cooling Water

System Check-out and Operation

Once the assembly of the system was complete, a thorough operation and safety analysis, called a "What If" Review, was conducted. This covered all safety issues related to the operation of the system and material hazards.

This check-out included:

- o Review of process flow design
- o Tour of the installation
- o Discussion of the operating theory
- o Definition of experimental work planned
- o Detailed review of shutdown logic
- o Line by line "walkthrough" of system using piping and instrumentation diagram
- o Detailed review of start-up and shutdown procedures
- o Utility failure modes and effects.

The outside vendor, Plasma Materials, Inc., inspected the installation and the plasma torch was operated successfully on a mixture of argon and nitrogen.

The system is considered complete and ready for initiation of Task 4 activities.

Task 2. Development of a Theoretical Model

The development of a theoretical model is intended to correlate particle surface area with major operational parameters. This is an expansion of previous Carborundum sponsored work and will assist in developing a fundamental understanding of a process reactions, assist in the extended parametric studies and scale-up tasks.

After consulation with the ORNL Technical Monitor, the modeling work was subcontracted to International Thermal Plasma Engineering, Inc. (Professor Boulous - University of Sherbrooke, Quebec, et al). The subcontractor was selected from a group of four proposals based on weighted selection criteria as follows:

	Total Possible Points in each Category
General Modeling Experience	20
Plasma Modeling Experience	30
Outline of Proposal	10
Cost of Proposal	20
Elapsed Time of Request	20
TOTAL	100

The successful bidder was awarded 80 to 100 possible points and was chosen as strongest or tied for strongest in each category except cost and was second in cost.

Task 2 will last eight months. Interim reports will be issued at approximately three month increments.

Task 3. Baseline Characterization and Analytical Method Development

The objectives for this task include:

- o Firmly establish the methodologies to be used for powder characterization
- o Define basic powder characteristics which may be utilized to assess property control and improvements as the program progresses.

Initially, two commercially produced SiC powders were to be characterized: H.C. Starck, Inc. (West Germany), A10 Grade; and Sohio-Carborundum submicron alpha SiC.

As both of the above powders are alpha phase, it has been decided to characterize one beta phase powder in addition. This will most likely be Starck B-10 grade.

The parameters to be characterized and the methodologies used include the following:

Characteristic	Methodology
o Pressureless sinterability	- Percentage of theoretical density achieved with and without sintering aids.
o Surface area	- B.E.T. surface analysis.
o Degree of agglomeration	- Tap density.
o Particle size distribution	- Horiba particle size analyzer.
o Bulk composition	- Wet chemistry.
o Phase distribution	- X-ray diffraction.

The results of the baseline characterization of the first two powders is as follows:

	Starck A10	Sohio-Carborundum
Pressureless Sinterability (percentage of theoretical density)		
- without sintering aids	63.6%	51.01%
- with sintering aids	96.2%	99.88%
Surface Area	14.3 m^2/g	9.47 m^2/g
Degree of Agglomeration		
- Tap density	0.847 g/cm^3	0.962 g/cm^3

Particle Size Distribution

Size μm	Cumulative Percentage greater than the indicated particle size: Starck A10	Sohio-Carborundum
>7	0	0
7-6	2.4	0.4
6-5	11.4	3.8
5-4	23.4	7.0
4-3	29.8	9.8
3-2	38.2	24.3
2-1.8	41.4	27.3
1.8-1.6	45.7	32.2
1.6-1.4	50.9	39.1
1.4-1.2	58.0	49.9
1.2-1.0	66.4	65.4
1.0-0.8	68.2	67.1
0.8-0.6	76.7	76.2
0.6-0.4	85.7	87.9
0.4-0.2	97.2	97.7
0.2-0	100.0	100.0
-Mean Particle Size	1.4 μm	1.2 μm

Bulk Composition

	Starck A10	Sohio-Carborundum
Chemical Analysis (wt %)		
Total Carbon	30.3	29.95
Free Carbon (corrected for oxidation)	1.54	0.36
Total Oxygen	0.76	0.27
Free Silicon	0.29	0.09
Si + SiO_2	1.73	0.60
SiO_2 (calculated from O_2)	1.44	0.51
SiC (calculated)	96.10	98.80
Emission Spectroscopy (wt %)		
	Aluminum .01	Aluminum <.01
	Calcium <.01	Calcium <.01
	Iron 0.03	Iron <.01
	Magnesium <.01	Magnesium <.01
	Titanium .01	Titanium <.01
		Vanadium <.01

	Starck A10	Sohio-Carborundum
Elements less than .005%	Boron Chromium Copper Manganese Nickel Zirconium Cobalt Molybdenum Vanadium	Boron Chromium Copper Manganese Nickel Zirconium
Phase Distribution		
Major	6HSiC	6HSiC
Low Trace	15R/4H	15R

The beta phase powder (Starck B-10) will be obtained and characterized in a subsequent reporting period.

Task 4. Screening Experiments

Task 4 has been divided into subtasks for management and reporting purposes. The first subtask will be to characterize the operation of the plasma torch using an Argon/Hydrogen blend. It should be noted that the original workscope included a short series of experiments to investigate the feasibility of using a hydrogen plasma in lieu of argon. This could prove advantageous as hydrogen is a reactant (to scavenge chlorine from the silicon source) and the argon (necessary only as a carrier of energy) could potentially be eliminated.

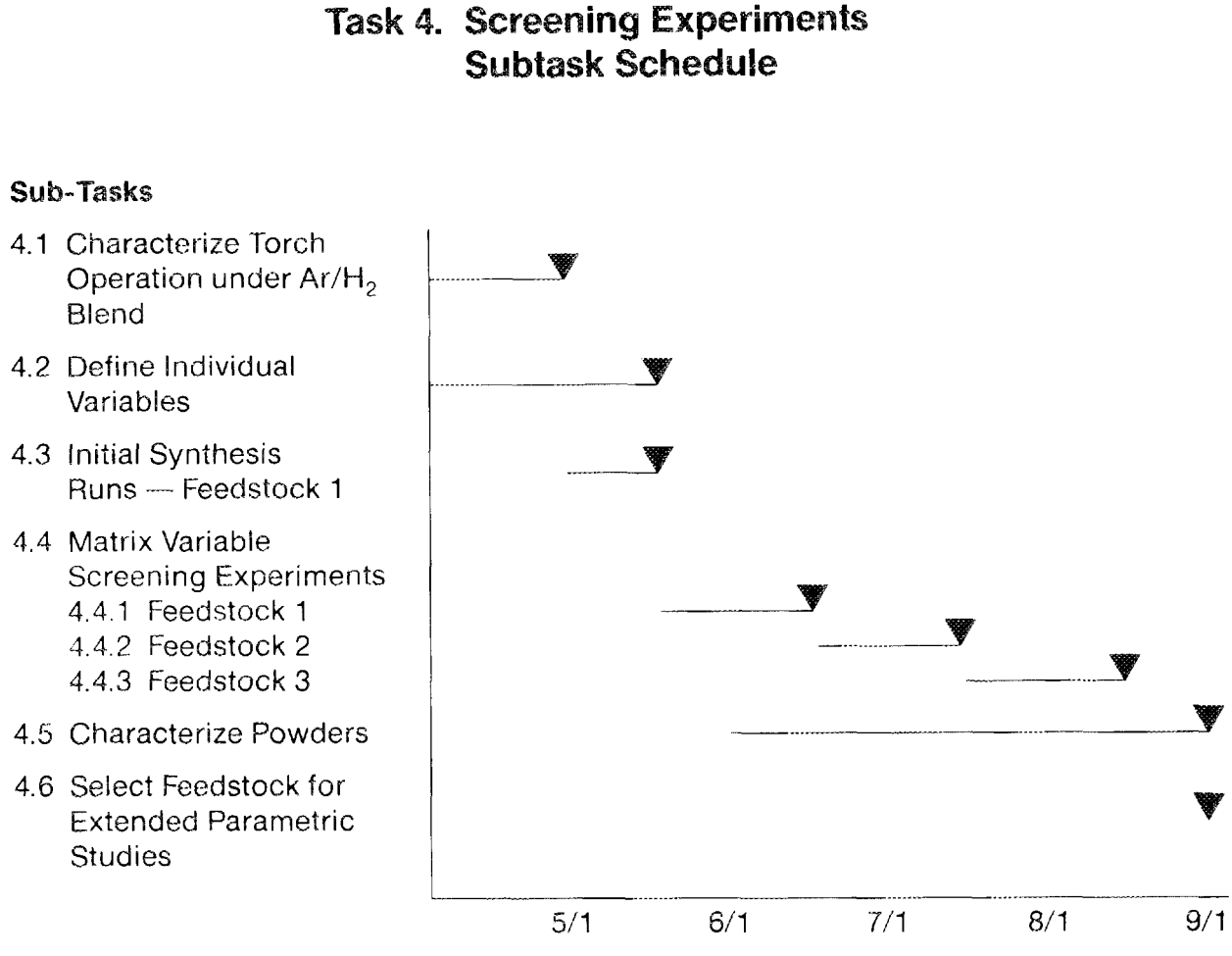

Figure 12. Subtask Schedule for Screening Experiments

As both Sohio-Carborundum and the torch vendor, Plasma Materials, were confident that the torch would operate with a very rich Hydrogen to Argon blend, it was decided to accomplish this subtask first.

Concurrent with that subtask, careful consideration will be given to the choice of the individual variables for the screening experiments. The candidate feedstocks will be as described in the statement of work, but the values (or range of values) for temperature, carbon/silicon ratio and reactant concentration must be selected.

Initial synthesis runs will also be made utilizing Feedstock 1 before the screening experiments actually get started. This will be to further check-out the operation of the system under actual operating conditions and to establish a baseline for the later experiments.

The matrix variable screening experiments depicted in Figure 13 will then begin. The candidate feedstocks are as follows:

Feedstock 1 : silicon tetrachloride ($SiCl_4$)
Feedstock 2 : dimethyl dichlorosilane [$(CH_3)_2$ $SiCl_2$]
Feedstock 3 : methyl trichlorosilane (CH_3 $SiCl_3$)

In each instance, the carbon source will be methane. Twenty four screening experiments are planned as noted in the experiment matrix.

Proposed Test Matrix: Screening Experiments

Reactant	Temperature	Carbon/Silicon Ratio	Reactant Concentration
Reactant 1	Hi	Hi	Hi
			Lo
		Lo	Hi
			Lo
	Lo	Hi	Hi
			Lo
		Lo	Hi
			Lo
Reactant 2	Hi	Hi	Hi
			Lo
		Lo	Hi
			Lo
	Lo	Hi	Hi
			Lo
		Lo	Hi
			Lo
Reactant 3	Hi	Hi	Hi
			Lo
		Lo	Hi
			Lo
	Lo	Hi	Hi
			Lo
		Lo	Hi
			Lo

Figure 13. Screening Experiment Test Matrix

At the end of each experiment, the resulting powders will be thoroughly characterized for pressureless sinterability, degree of agglomeration, particle-size distribution, bulk composition, and phase distribution. Safety and yield considerations will also weigh in the ultimate selection of the feedstock to be carried into the extended parametric studies.

Status of Milestones

	Milestones	Status
Task 1.	Design, Construct and Test Laboratory Scale Equipment	- 98% complete as of April 1; on schedule.
Task 2.	Develop Theoretical Model	- Initiated March 1; on schedule.
Task 3.	Baseline Characterization and Analytical Model Development	- Two-thirds complete; on schedule.
Task 4.	Screening Experiments	- Initiated April 1; on schedule.
	o Selection of Feedstock	- Scheduled for September 1.
Task 5.	Extended Parametric Studies	- To be initiated September 1.
	o Provide 200-500g Sample to ORNL	- Scheduled for March 1, 1986.
Task 6.	Reporting Requirements	- On schedule.
Task 7.	Quality Assurance	- Ongoing.

Communications/Visits/Travel

John Poole of Plasma Materials, Inc. visited the reactor installation at Sohio's Warrensville (Ohio) Laboratory to evaluate the installation and performance of the plasma torch.

The first bi-monthly Technical Report was issued April 11.

Dr. V. (Venkat) Venkateswaran will give a brief presentation on this work during the Heat Engine Symposium of the ACerS Annual Meeting on Wednesday, May 8 in Cincinnati, Ohio.

Problems Encountered

None.

Publications

None.

1.1.2 Silicon Nitride

Sintered Silicon Nitride — G. E. Gazza (Army Materials and Mechanics Research Center)

Objective/scope

The in-house program is concentrating on sintering compositions in the Si_3N_4-Y_2O_3-SiO_2 System using a two-step sintering method where the N_2 gas pressure is raised from 1-2 MPa to 7-8 MPa during the densification process. During the sintering under high pressure nitrogen, the environment is extremely reducing and the oxygen content of the starting materials is significantly reduced by the formation of SiO. The use of cover powder over the samples reduces the oxygen loss. Milling time also influences "green" density and resultant sintered density by changing the particle size distribution of starting powders, reducing agglomeration and producing a more equiaxed particle morphology. Milling studies are being conducted with three different sources of starting Si_3N_4 powder.

Technical Progress

Reaction bonded Si_3N_4 bars containing ¢%Y_2O_3-1%Fe_2O_3 (supplied by Garrett Turbine Engine Co.) were sintered to high density using a two-step pressure/temperature sintering cycle. Some bars were pre-oxidized to alter the starting SiO_2 content. Stress-rupture, oxidation and modulus of rupture data, as shown in Table 1, were obtained on sintered bars.

During sintering experiments with specimen compositions within the Si_3N_4-$Y_2Si_2O_7$-Si_2N_2O and Si_3N_4-$Y_2Si_2O_7$-$Y_5(SiO_4)_3N$ compatibility triangles, it was observed that the composition of the cover powder (in particular the % SiO_2) significantly affected the weight change (gain or loss) measured on the specimen after sintering. Compositional adjustments in the cover powder could be made so only very small weight changes were observed in sintered bodies.

The Si_3N_4 corner of the Si_3N_4-Y_2O_3-SiO_2 phase diagram is shown in Figure 1.[3,4] The dots indicate the matrix of compositions being studied. Additional compositions (not shown) have recently been added for study.

Two-step pressure - temperature cycles are being used to densify the compositions of interest. The effect of raising the nitrogen gas pressure in the second step of the cycle on specimen density is illustrated in Figure 2. A 9.9 volume % addition of Y_2O_3 and SiO_2 was used for these compositions.

Scale-up of certain compositions within each compositional compatibility triangle is proceeding. Initial dimensions are 4.75 cm diam. x 1.50 cm thick (green body) which densifies to approximately 3.80 cm diam. x 1.25 cm thick. Specimens are being machined from these bodies for mechanical property evaluation.

Room temperature modulus of rupture, high temperature stress-rupture, oxidation resistance and fracture toughness are being measured for various sintered Si_3N_4-Y_2O_3-SiO_2 compositions.

Three-dimensional processing maps are being constructed which show topographical variation of sintered densities with different total volume percent addition and Y_2O_3/SiO_2 molar ratio. Theoretical densities were also calculated for the matrix of compositions being studied and a topographical map was constructed using these values with appropriate volume percent addition and Y_2O_3/SiO_2 molar ratios.

Milestones

Evaluation of modulus of rupture, stress-rupture, oxidation resistance and fracture toughness of sintered compositions is proceeding.

Publications

(1) Influence of Y_2O_3/SiO_2 Ratio on Sintering of Silicon Nitride, to be published in the Proceedings of the 22nd Automotive Technology Development Contractor's Coord. Meeting, October 29 - November 2, 1984.

(2) Effect of Oxidation on the Densification of Sinterable RBSN, report in process.

Presentations

(1) Influence of Y_2O_3/SiO_2 Ratio on Sintering of Silicon Nitride, 22nd Automotive Tec. Dev. Contractor's Coord. Meeting, Nov. 1984.

(2) Effect of Oxidation on the Densification of Sinterable RBSN, 37th Pacifica Coast Regional Meeting, American Ceramic Society, Basic Sci. Div., San Fran., CA, Oct. 31, 1984.

TABLE 1

CREEP, OXIDATION & MOR DATA

STRESS-RUPT TEMP ^{o} C	TIME (hrs.)	$\varepsilon(hr^{-1})$ (%PERM STRAIN)	OXID. RATE CONST. ($kg\ ^{2}m^{-4}s^{-1}$)	MOR @ RT AFTER S.R. TEST
700	750	n.m.	n.m.	570
1000	750	n.m.	$2.0x10^{-13}$	390-510
1200	1000	$1.0\text{-}2x10^{-6}$ (0.1-0.2%)	$6.5x10^{-13}$	486-670

(STSR FROM 800C PRIOR TO ALL TESTS @ 1000C and 1200C)

σ=300 MPa

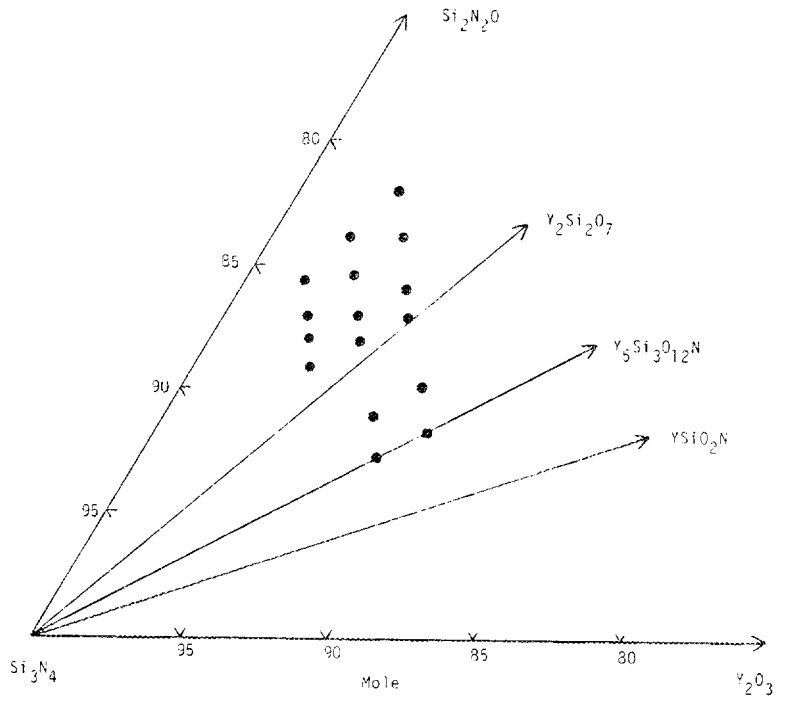

Figure 1 Section of Si_3N_4-Y_2O_3-SiO_2 Phase Diagram Showing Location of Compositions

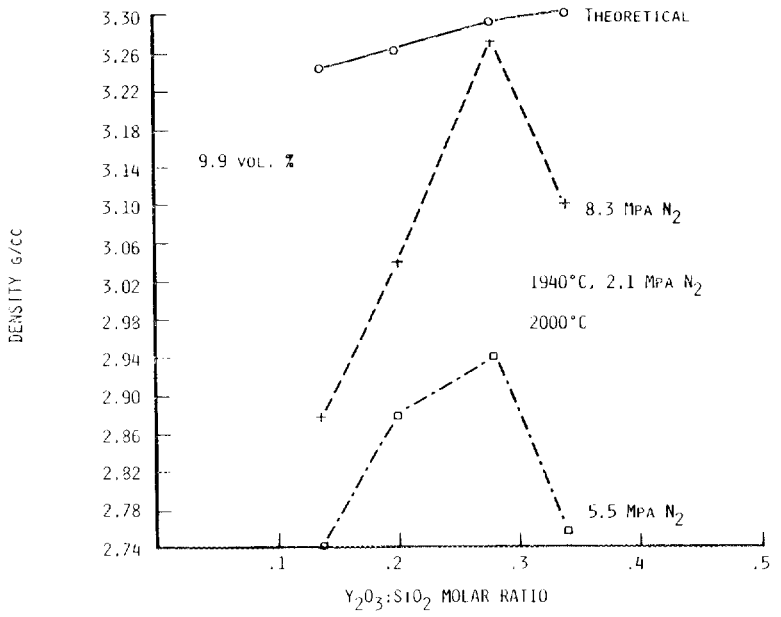

Figure 2 Effect of High Nitrogen Gas Pressure on Densification

1.2 CERAMIC COMPOSITES

1.2.1 Silicon Carbide Matrix

SiC-Matrix Ceramic Composites

M. A. Janney (Oak Ridge National Laboratory)

Objective/scope

The goals of this work are to develop new SiC-matrix composites with improved strength and toughness and to develop the processing capabilities to form these materials into useful shapes.

Technical progress

SiC-TiB_2 composites

Two recent investigations[1,2] have demonstrated strength and toughness increases in SiC by the inclusion of TiC particles as a dispersed phase. Toughening and strengthening were attributed to crack deflection caused by the interaction of the crack front with a residual stress field that surrounded the TiC particles. The origin of this stress field was the difference in thermal expansion and elastic modulus between SiC and TiC. On the basis of this toughening mechanism, it was reasoned that a SiC matrix composite with TiB_2 as the dispersed phase would also show increased toughness and strength. The stress at the interface between the TiB_2 particles and the SiC matrix can be calculated from Eq. (1):[3]

$$\sigma_{m\theta} = -\frac{1}{2}\sigma_{ph} = \frac{-(\alpha_p - \alpha_m)\,\Delta T}{\frac{1+\nu_m}{2E_m} + \frac{1-\nu_p}{2E_p}}, \qquad (1)$$

where

$\sigma_{m\theta}$ = tangential matrix stress at the particle-matrix interface,
σ_{ph} = hydrostatic stress in the particle,
ΔT = temperature range over which stresses are not relieved by a diffusive process,
ν = Poisson's ratio (m - matrix, p - particle),
E = Young's modulus.

Using E_m = 440 GPa, E_p = 550 GPa, ν_m = 0.19, ν_p = 0.10, $\alpha_m = 5 \times 10^{-6}/°C$, $\alpha_p = 8 \times 10^{-6}/°C$, and ΔT = 1000°C, one calculates $\sigma_{m\theta}$ = 1380 MPa, which is approximately twice the value of 500 MPa obtained for the SiC-TiC system.

Materials and methods

SiC*-TiB_2† specimens were prepared for hot pressing at 0.0 and 15.1 vol % (20 wt %) TiB_2 with 1 wt % elemental boron‡ and 0.5 wt % carbon black** as sintering aids. The composition was wet vibro milled in isopropanol with 1 wt % polyvinylpyrollidone†† as dispersant using 1/4-in.-diam × 4-in.-long α-SiC rods.‡‡ Samples were hot pressed in carbon dies lined with graphite foil at 2000°C for 45 min at 35 MPa (5 kpsi) to final dimensions of 38 mm in diam by 25 mm high.

Four-point-bend loading was used to measure fracture strength. Samples were cut from each hot-pressed billet perpendicular to the hot-pressing direction and then were ground parallel to the long axis with a 140/170-grit resin-bonded diamond wheel to 2.3 × 2.5 × 25 mm dimension. The tensile face was ground to a 30-μm finish, and the tensile edges were beveled to eliminate edge flaws. The bars were tested at a crosshead speed of 0.51 mm/min. The outer and inner test spans were 1.9 cm (0.75 in.) and 0.64 cm (0.25 in.), respectively.

Some of the test bars described above were oxidized at 1000, 1200, and 1400°C in static air for 24 h. Strength was measured at ambient temperature after oxidation. Specimens were also examined metallographically to determine the extent of oxidation and to characterize the oxidation products.

Results

Both the 0 vol % and the 15.1 vol % TiB_2 samples were hot pressed to approximately 96.5% theoretical density. Figure 1 shows both the as-polished and the etched microstructure of the SiC—15.1 vol % TiB_2 composite. The TiB_2 particles were essentially equiaxed and ranged in size from four to eight micrometers. The SiC grains were also equiaxed with an average size of about three to five micrometers; there was no evidence of discontinuous grain growth in the etched microstructure.

The strength of the SiC—15.1 vol % TiB_2 composite was significantly higher than that of the base SiC (Fig. 2). The mean strength, $\bar{\sigma}$, increased by 28% from 380 to 485 MPa with essentially no change in the Weibull modulus (11.3 vs 12.6). The strength of the SiC—15.1 vol % TiB_2 composite was significantly higher than the 350-MPa strength reported by Murata and Weber[4] for similar compositions produced by sintering.

---

*A-10, H. C. Starck Company, Berlin, Federal Republic of Germany.

†KBI Division, Cabot Corporation, Reading, Pa.

‡330 AE, Var-Lac-Oid Chemical Company, Elizabeth, N.J.

**Philblack N774, Phillips Chemical Company, Borger, Tex.

††PVPK15, GAF Corporation, New York.

‡‡Kindly supplied by Carborundum Company, Niagara Falls, N.Y.

Y-200972

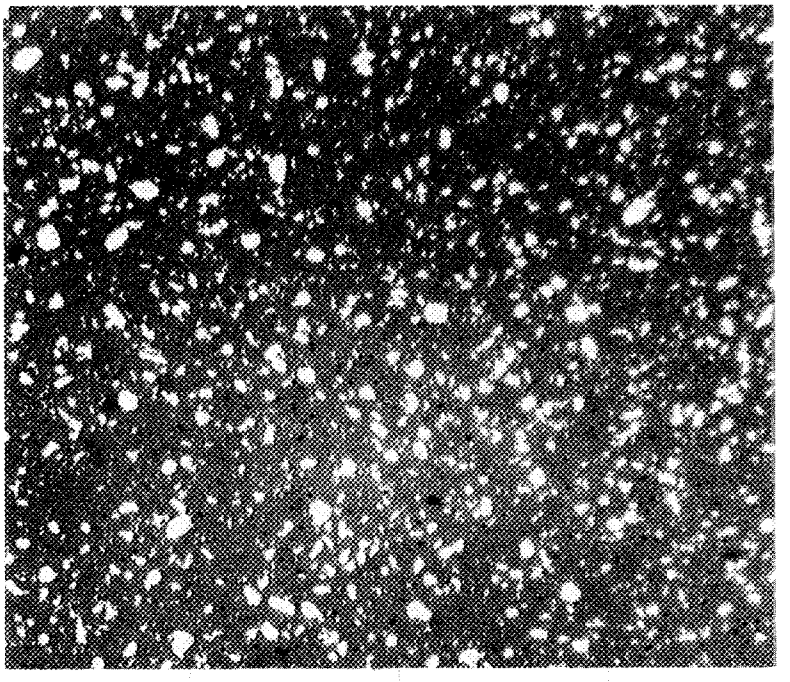

(a)

50 μm

Y-197807

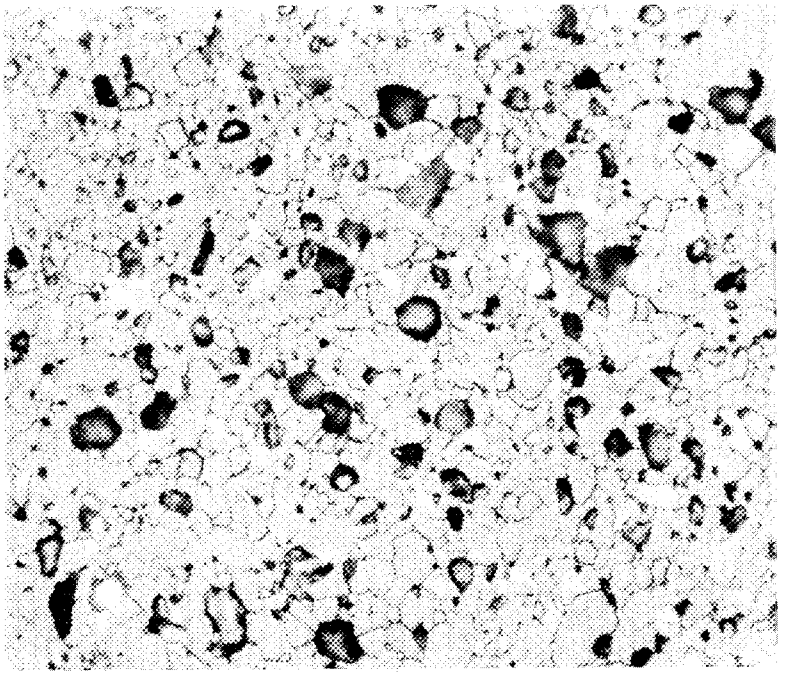

(b)

20 μm

Fig. 1. SiC—15.1 vol % TiB_2 composite was hot pressed to 96.5% theoretical density. (*a*) As polished. (*b*) Murikami's etch.

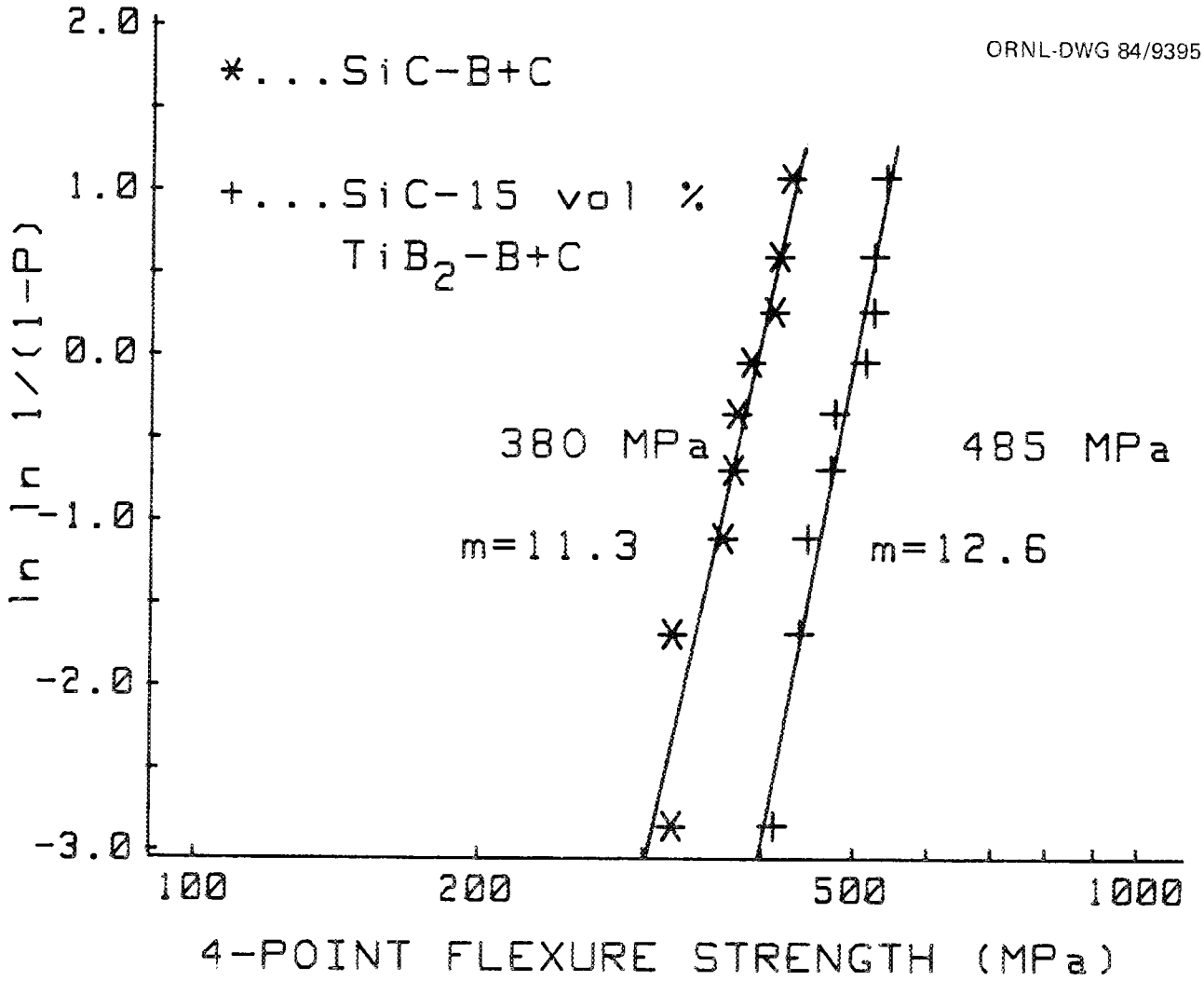

Fig. 2. Strength of SiC increased on TiB_2 addition.

Oxidation at 1000, 1200, and 1400°C for 24 h in air produced varying degrees of attack as shown in Fig. 3. The maximum depth of attack was ~10 μm at 1000°C, ~20 μm at 1200°C, and > 250 μm at 1400°C. The oxidation product on the surface consisted of bubbles of glass which contained a bright crystalline phase. Within the composite both the TiB_2 particulate phase and the SiC matrix were attacked. Interconnected porosity and a glass phase extended deep into the composite at the highest exposure temperature (1400°C).

The room-temperature strength of the SiC—15.1 vol % TiB_2 specimens oxidized at 1000 and 1200°C did not change as compared with the unoxidized material (Table 1). Only the samples oxidized at 1400°C showed an appreciable loss of strength after oxidation (192 MPa vs 485 MPa).

Table 1. Strength of SiC and SiC—15.1 vol % TiB_2 flexure bars

Sample	Mean strength (MPa)	Standard deviation (% of mean)	Number of specimens
SiC—0 vol % TiB_2	379	10.2	9
SiC—15.1 vol % TiB_2	485	9.1	9
SiC—15.1 vol % TiB_2 oxidized at 1000°C	480	9.7	5
SiC—15.1 vol % TiB_2 oxidized at 1200°C	498	9.9	5
SiC—15.1 vol % TiB_2 oxidized at 1400°C	192	14.1	5

Discussion

Strength

The increase in strength of the SiC—15.1 vol % TiB_2 composite as compared with the base SiC ceramic probably is due to an increase in K_{Ic} of the composite in analogy to the SiC-TiC system.[1,2] K_{Ic} was not measured during this investigation; however, direct observations of cracks were made. Figure 4 shows a crack emanating from the corner of a Vickers identation in a SiC—15.1 vol % TiB_2 composite. The micrograph shows several examples where the trajectory of the crack was deflected out of the plane of travel by the presence of a TiB_2 particle. In most cases, the crack path followed the particle-matrix interface, as predicted by theory.[1] An example of crack branching, which constitutes an additional toughening mechanism, is also shown in the center of the micrograph.

ORNL-PHOTO 0242-85

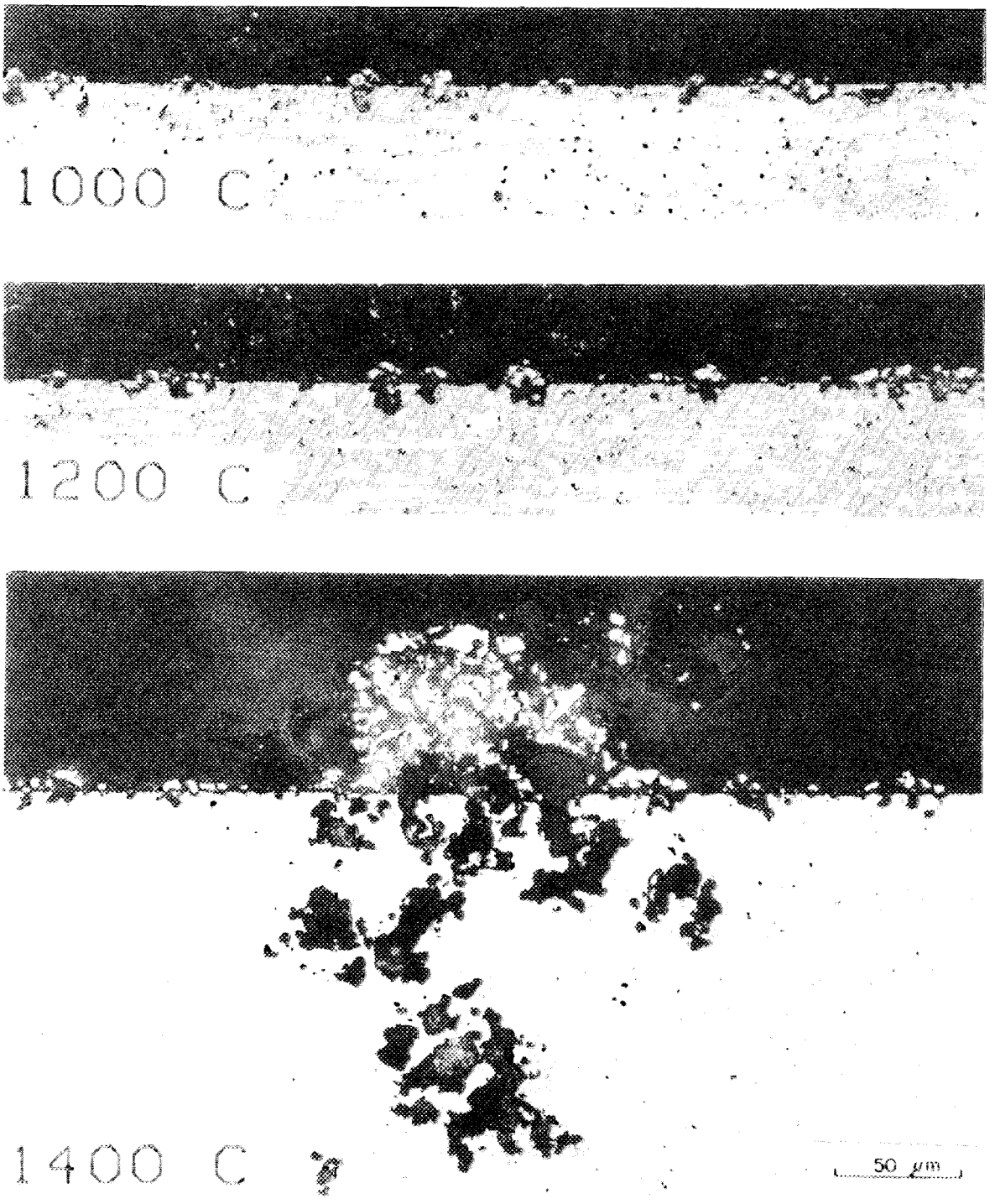

Fig. 3. Surface damage of SiC-TiB_2 increased as temperature was raised.

An estimate of the magnitude of K_{Ic} can be made from the increase in strength on addition of TiB_2 by invoking the Griffith relationship:[5]

$$\sigma_f = \frac{Z}{Y} \frac{K_{Ic}}{\sqrt{c}}, \qquad (2)$$

where

σ_f = fracture stress,
K_{Ic} = critical fracture toughness,
c = critical flaw size,
Z and Y = geometric parameters dependent on location and shape of flaw, stress state, etc.

If one assumes similar flaw geometries in the SiC and SiC—15 vol % TiB_2 samples (i.e., constant Z, Y, and distribution of flaw sizes, c), then $\overline{\sigma}_f$ and K_{Ic} should be proportional. Since $\overline{\sigma}_f$ increased by 28%, from 380 to 485 MPa, a similar increase should be expected in K_{Ic}. Wei and Becher[1] reported K_{Ic} for a similar SiC to be about 3.85 MPa $\sqrt{m}$; hence, K_{Ic} for the SiC—15.1 vol % TiB_2 composite is estimated to be about 4.9 MPa $\sqrt{m}$.

The postoxidation strength behavior of the SiC—15.1 vol % TiB_2 composites is reasonable in light of the estimated K_{Ic} for the composite.

L609

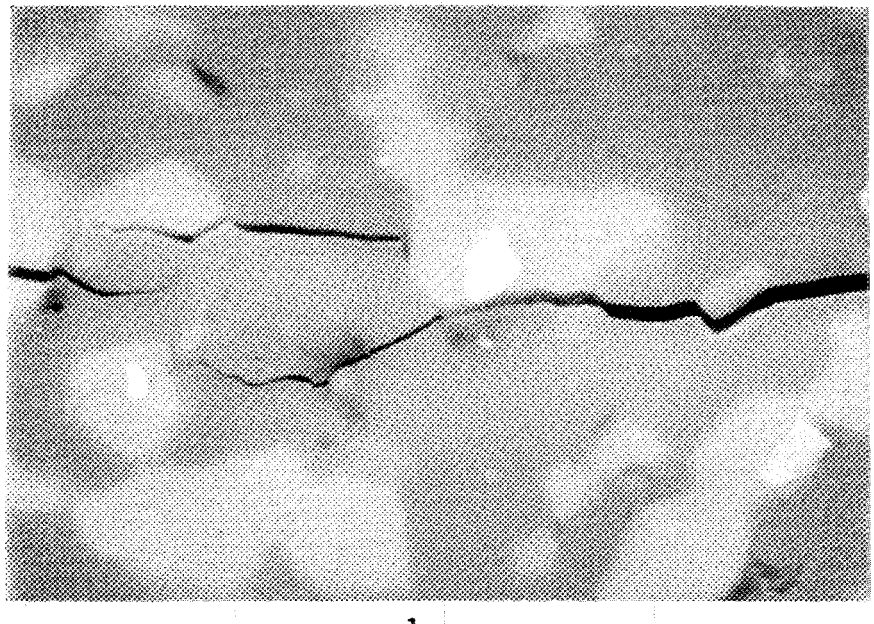

Fig. 4. Crack deflection in SiC-TiB_2.

Oxidative attack was limited to depths less than 20 μm at 1000 and 1200°C. This is much less than the critical flaw size for a K_{IC} of 4.9 MPa $\sqrt{m}$. Assuming the Griffith relationship is valid and using $Z = 1.5$, $Y = 2.0$, (ref. 5), and $\bar{\sigma}_f = 485$ MPa, one calculates $c = 57$ μm. Only the samples oxidized at 1400°C showed a major decrease in strength. This was due to oxidative attack to depths greater than 250 μm. If the oxidation pits acted as critical flaws, then a 250-μm pit would predict [based on Eq. (2)] a strength of about 230 MPa, which is in reasonable agreement with the observed mean strength of 192 MPa.

Oxidation mechanism

The oxidation of the SiC—15.1 vol % TiB_2 composites was catastrophic; both the dispersed TiB_2 phase and the SiC matrix phase were consumed. This was in marked contrast to the oxidation behavior of SiC-TiC composites[6] in which only the TiC dispersed phase was attacked. The difference in behavior is believed to be due to the presence of boron.

Figure 5 shows a back-scattered-electron scanning-electron-microscope photograph of the 1400°C-oxidized sample previously shown in Fig. 3. The bright areas are Ti-rich. Within the composite, the predominant Ti-rich phase is TiB_2 from the original composite. However, electron-probe microanalysis indicated that the Ti-rich phases which were surrounded by glass (e.g., "A" and "B" in Fig. 5) contained large amounts of oxygen.

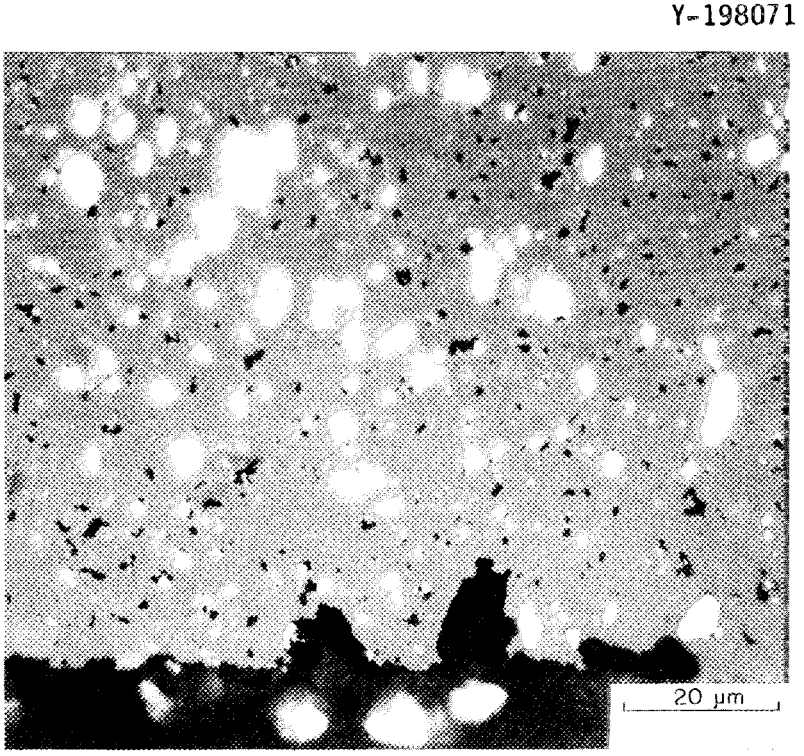

Fig. 5. Cross section at the surface of a SiC—15.1 vol % TiB_2 composite sample oxidized at 1400°C for 24 h in air.

This indicates that the TiB_2 had been oxidized, probably to TiO. An additional Ti-rich phase was present in the oxidation product on the surface. X-ray diffraction (XRD) of the surface of this sample showed the rutile phase of TiO_2 to be the only crystalline phase present. The XRD data combined with light microscopy (Fig. 3) indicate that the large bubbles observed on the surface of the samples were composed of glass and rutile. Also shown in Fig. 5 are large pores and gas bubbles which extend from the interior of the composite up to the surface. The bubble in the center of the micrograph (marked C) was pushing its way to the surface when the sample was removed from the furnace. The gas composition in the bubbles probably was a combination of CO and BO_x.

The oxidation of the SiC-TiB_2 composites is hypothesized to occur as outlined below. The main chemical reactions of concern are

$$TiB_2 + O_2 \rightarrow TiO + BO_x \quad (x = 1\text{-}1.5) \tag{3}$$

$$B_2O_3 + O_2 + SiC \rightarrow B_2O_3\text{-}SiO_2 \text{ (glass)} + CO \tag{4}$$

$$TiO + 1/2\ O_2 \rightarrow TiO_2\ . \tag{5}$$

The sequence of events leading to oxidation might be as follows. First, an isolated particle of TiB_2 on the surface of the composite oxidizes to form TiO or TiO_2 and B_2O_3 according to Eq. (1). At the temperatures examined in this investigation (i.e., between 1000 and 1400°C), B_2O_3 forms a very fluid, volatile glass, which has a high capacity for transporting oxygen. The boria glass then combines with SiC to form CO and a high-boron-content borosilicate glass, which is also very fluid. As the SiC matrix is attacked, additional TiB_2 particles are encountered; these provide more boron to flux the SiC matrix. The high oxygen transport capacity of the fluid borosilicate glass allows oxygen to penetrate deeper into the body of the composite, which leads to additional attack on the TiB_2 and the SiC.

Support for this hypothesis comes from the response to oxidation of a composite containing only 7 vol % TiB_2, Fig. 6. When this material was oxidized at 1400°C for 24 h, the maximum depth of attack was limited to only about 10 to 15 μm. The TiB_2 particles were spaced farther apart than in the 15.1 vol % TiB_2 composite; hence, more SiC matrix phase had to be dissolved before the next TiB_2 particle could be oxidized. Apparently, not enough boron was available to attack such a thick layer of SiC.

Movement of the titanium to the surface of the composite appears to have been by viscous transport in the glass phase. As the glass was blown to the surface by gas bubbles containing BO and CO, oxidized TiB_2 particles (now TiO or TiO_2) were carried along in the glass. Several examples of this type of transport are shown in Fig. 5, especially near the bubble marked "C". Microprobe data suggest that the Ti concentration in the glass decreased between the interior and the surface, indicating that Ti might precipitate out of solution as the oxygen potential in the glass increased.

YP-398

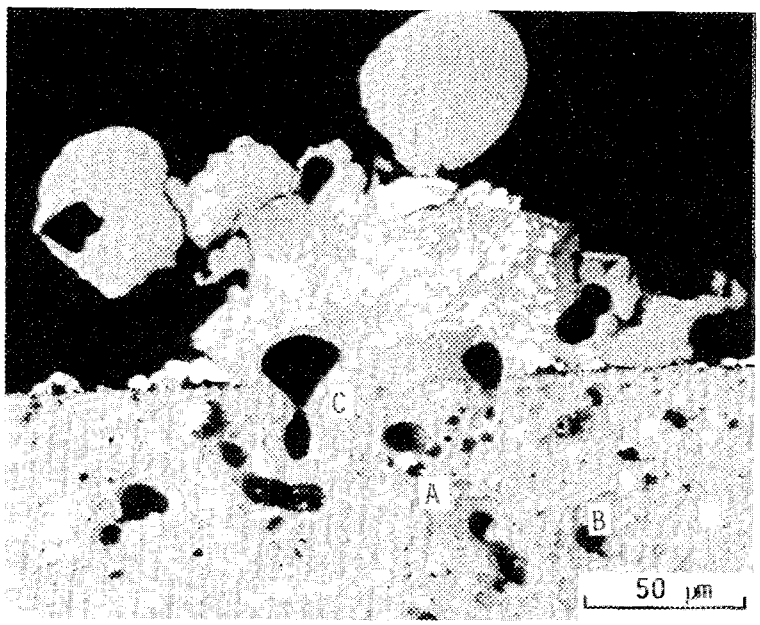

Fig. 6. Oxidation attack depth in the SiC—7.0 vol % TiB_2 was limited to about 10 μm. Sample oxidized at 1400°C for 24 h.

Summary and conclusions

SiC—15.1 vol % TiB_2—1 wt % B + 0.5 wt % C composites were hot pressed to about 96.5% theoretical density at 2000°C. Addition of the TiB_2 increased the strength of the composite by 28% as compared with the base SiC. These composites were attacked by oxidation at temperatures between 1000 and 1400°C, with the rate of attack increasing with increasing temperature. Ambient-temperature strength determined after oxidation showed no reduction in strength for samples oxidized at 1000 or 1200°C; however, strength fell 60% for samples oxidized at 1400°C. Oxidative attack involved both the TiB_2 particulate phase and the SiC matrix phase. Large bubbles containing glass and TiO_2 formed on the surface of the samples. Boron oxide is postulated as a fluxing agent that accelerates the attack of the SiC matrix by forming a nonprotective oxide glass layer on the surface of the composite.

References

1. G. C. Wei and P. F. Becher, "Improvements in Mechanical Properties in SiC by Addition of TiC Particles," *J. Am. Ceram. Soc.* **67**(8), 571—74 (1984).

2. M. A. Janney, "Microstructural Development and Mechanical Properties of SiC and of SiC-TiC Composites," submitted to *J. Am. Ceram. Soc.*

3. A. G. Evans and T. G. Langdon, "Structural Ceramics," *Prog. Materials Sci.* 21(3–4), 171–441 (1976).

4. Y. Murata and G. W. Weber, *Sintered SiC-TiB_2 Mixtures and Articles Thereof*, U.S. Patent 4,327,186 (April 27, 1982).

5. D. W. Richerson, *Modern Ceramic Engineering*, Marcel Dekker, Inc., New York, 1982.

6. M. A. Janney, "Particulate Toughened Silicon Carbide," pp. 497–504 in *Proceedings 22nd Automotive Tech. Dev. Contractors' Coordination Mtg.*, SAE P-155, Society of Automotive Engineers, Dearborn, Mich., 1985.

1.2.3 Oxide Matrix

SiC-Whisker-Reinforced Ceramic Composites

T. N. Tiegs, P. F. Becher, and R. K. Williams (Oak Ridge National Laboratory)

Objective/scope

This work involves development and characterization of SiC-whisker-reinforced oxide composites for improved mechanical performance. To date, most of the work has dealt with alumina as the matrix because it was deemed a promising material for an initial study. However, optimization of matrix materials is also being explored. The approach to fabrication is to first use hot pressing to identify compositions for toughening and then to develop pressureless sintering for fabrication of near-net-shape pieces. Initial work has been described in previous semiannual reports.

Technical highlights

Modification of SiC whiskers

We are investigating ways to modify the SiC whiskers in order to change the interface between them and the matrix to maximize the mechanical properties.

Because of the encouraging results where the fracture toughness of a 20 vol % SiC whisker–Al_2O_3 composite was increased to 9.4 MPa·$m^{1/2}$ after milling the whiskers for 8 h, a study was undertaken to quantitatively assess the effect of milling on the whisker size distribution.

Whisker batches were milled 1 h, 4 h, and 16 h and then hot pressed with an Al_2O_3 matrix at 20 vol % whisker concentration into samples. Metallography showed good distribution of the SiC whiskers with no major defects. Analysis of the milled whiskers by scanning electron microscopy (SEM) show that the average whisker length after milling 1 h is 18 to 20 μm; however, the distribution is large (1–100 μm). After milling 4 h, the average length is 10 to 12 μm, but the distribution is much narrower (>90 % less than 30 μm). Further milling up to 16 h only reduces the average length to 9 to 11 μm, but the distribution is further reduced (>90 % less than 20 μm).

The mechanical properties were determined on specimens machined from the hot-pressed billets and are presented in Table 1. As shown, the flexural strengths are the same or higher than normally observed for a similar composite using unmilled SiC whiskers (which is typically 650 MPa). However, the fracture toughness values indicate that some severe degradation of the SiC whiskers has occurred. We speculate that the whisker surfaces are damaged during milling in addition to the reduction in aspect ratio. We plan to examine some archive samples by transmission electron microscopy to determine the extent of any damage. The initial samples where we observed increases in fracture toughness with milling times were processed by milling the Al_2O_3 and SiC whiskers together. The presence of the Al_2O_3 particles may help to cushion the whiskers during the milling operation and reduce any whisker surface damage.

Table 1. Summary of mechanical properties of Al_2O_3—20 vol % SiC whisker composites

Sample number	Whisker mill time (h)	Flexural strength[a] (MPa)	Fracture toughness, K_{Ic} ($MPa \cdot m^{1/2}$)[b]
SCW-76	1	655	6.3
SCW-77	4	755	5.7
SCW-78	16	705	7.3

[a]Measured by four-point bend test.
[b]Measured by multiple-indent method.

The vast majority of testing to date has been with the SiC whiskers produced by ARCO Chemicals Co. However, we are looking at other sources of SiC whiskers: Tateho Chemical Industries Co., Versar Manufacturing Inc., and Los Alamos National Laboratory (LANL). Previously, we had examined and tested SiC whiskers from Tokai Carbon Co.[1] With the exception of the LANL whiskers, all are available in commercial quantities. At the present time, we have fabricated Al_2O_3—20 vol % SiC whisker composites from these alternate sources and plan to test the mechanical properties. These will be compared to the results previously obtained on composites made with whiskers from ARCO Chemicals and Tokai Carbon.

Rice-hull remnants

An Al_2O_3—20 vol % SiC whisker sample was fabricated by hot pressing and machined into bend bars to determine Weibull statistics on these composite materials. The mean strength of the samples in four-point bend tests was about 550 MPa or about 100 MPa less than previous composites with comparable whisker concentrations. Examination of the fracture surfaces revealed large flaws at the fracture origins. Further examination with SEM (Fig. 1) showed the flaws to be remnants of rice hulls used to produce the SiC whiskers. We have now determined that the rice-hull remnants can be removed from the whiskers by flotation in water and are now cleaning all whiskers prior to use in making test composites.

Pressureless sintering

Several batches of SiC whisker—Al_2O_3 composites were fabricated with whisker concentrations ranging from 5 to 20 vol %. They were sintered under similar conditions, and the results are summarized in Table 2. As shown, high densities were achieved for whisker concentrations up to 10 vol %. As the whisker concentrations approach 20 vol % the densities drop dramatically and illustrate the fact that some pressure assistance is probably needed to densify composites at high whisker concentrations. Other avenues for improving the pressureless sinterability of the SiC whisker—Al_2O_3 composites are being explored.

M-21100

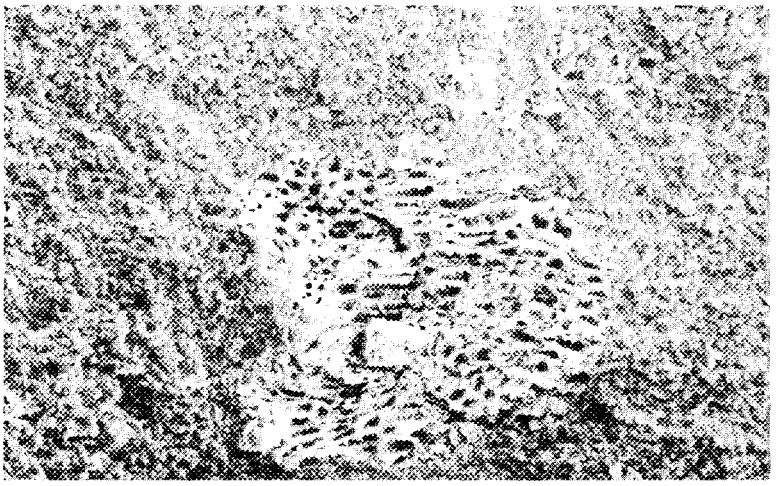

(*a*)

100 μm

M-21111

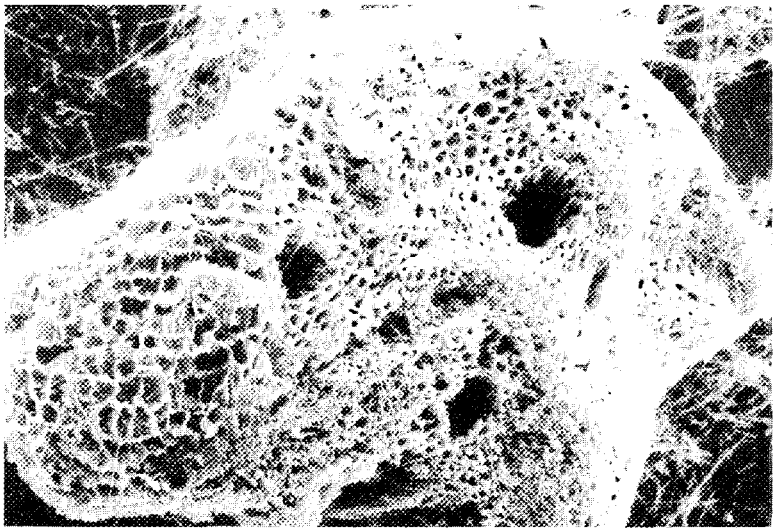

(*b*)

100 μm

Fig. 1. (*a*) Fracture surface of Al_2O_3—20 vol % SiC whisker composite showing rice-hull remnant at origin. (*b*) Rice-hull remnant removed from SiC whiskers by flotation in water.

Table 2. Summary of results on sintering of Al_2O_3—SiC whisker composites with various whisker concentrations

Whisker volume concentration (%)	Sintered density (Mg/m^3)	Fraction of theoretical density (%)
5	3.81	97.1
10	3.70	95.2
11.3	3.65	93.4
15	3.10	80.6
20	2.90	75.0

Low-thermal-conductivity matrices

For applications in certain areas of the uncooled diesel engine, the use of composites having a matrix material with low thermal conductivity is desirable.

The materials considered as candidate low-thermal-conductivity matrices in ceramic composites for structural applications were mullite, zirconia, alumina-zirconia, and alumina-chromia solid solutions. The reinforcements considered were SiC and Si_3N_4 whiskers and also Al_2O_3 and ZrO_2 fibers. A series of composites were fabricated by hot pressing (Table 3). As shown, not all of the sample fabrications were successful in this initial scoping of low-thermal-conductivity composites. On the other hand, some of these first fabrications were very successful.

The composites having mullite as the matrix material [with only one exception (SCW-80)] were easily fabricated; consequently they provided most of the mechanical test data. Examination of ceramographic polished sections showed little interaction between both the SiC and Si_2N_4 whiskers and the mullite matrix. When the ZrO_2 was added to the mullite matrix (SCW-80), there was interaction between the ZrO_2 particles and SiC whiskers and not the mullite. Similar interactions between the ZrO_2 particles and SiC whiskers were observed in the Al_2O_3—ZrO_2 matrix composites.

The composites in which ZrO_2 was the matrix showed the most interactions with the reinforcement materials. Some of the problem, we believe, is due to the 12 vol % Y_2O_3 stabilizer used, and the same interaction problems could be anticipated in partially stabilized zirconia when Y_2O_3 is used. Further development of processing controls may help alleviate some of these interaction problems.

The incorporation of Cr_2O_3 into Al_2O_3 to form a solid solution has been shown to significantly lower the thermal conductivity.[2] However, when SiC whiskers are added and samples fabricated at elevated temperatures, reduction of Cr_2O_3 to metallic Cr by the SiC occurs. The resulting microstructure shows that none of the whiskers remain unaffected after fabrication.

Table 3. Summary of fabrication of whisker-reinforced low-thermal-conductivity matrices

Sample	Matrix	Reinforcement	Density (% T.D.)	Comments
SCW-49	Mullite	20 vol % SiC whiskers	100.0	Good sample
SCW-49A[a]	Mullite	20 vol % SiC whiskers	100.0	Good sample
SCW-50	Mullite	10 vol % SiC whiskers	100.0	Good sample
SCW-81	Mullite	20 vol % Si_3N_4 whiskers	99.3	Good sample
SCW-81A[b]	Mullite	20 vol % Si_3N_4 whiskers	99.4	Good sample
SCW-80	Mullite—30 vol % ZrO_2	20 vol % SiC whiskers	N.D.[c]	Melting observed
SCW-84	Mullite—12 vol % ZrO_2	20 vol % SiC whiskers	99.7	Good sample
SCW-48[d]	ZrO_2 (12 wt % Y_2O_3)	10 vol % SiC whiskers	85.0	Whisker-matrix interaction
SCW-66	ZrO_2 (12 wt % Y_2O_3)	20 vol % Si_3N_4 whiskers	90.0	Whisker-matrix interaction
SCW-75	ZrO_2 (12 wt % Y_2O_3)	20 vol % Si_3N_4 whiskers	91.2	Whisker-matrix interaction
SCW-88	ZrO_2 (12 wt % Y_2O_3)	20 vol % Si_3N_4 whiskers	92.5	Good sample
SCW-87	ZrO_2 (12 wt % Y_2O_3)	20 vol % Al_2O_3 fibers	93.1	Melting observed
SCW-18	Al_2O_3—12 vol % ZrO_2	20 vol % SiC whiskers	95.9	Whisker-matrix interaction
SCW-85	Al_2O_3—12 vol % ZrO_2	20 vol % SiC whiskers	99.4	Whisker-matrix interaction
SCW-85A	Al_2O_3—12 vol % ZrO_2	20 vol % SiC whiskers	100.0	Good sample
SCW-86	Al_2O_3	20 vol % ZrO_2 fibers	98.7	Melting observed
SCW-21	Al_2O_3—10% Cr_2O_3	20 vol % SiC whiskers	95.5	Whisker-matrix interaction

[a]Smaller grain size than SCW-49.

[b]Smaller grain size than SCW-81.

[c]Not determined.

[d]Pressureless sintered instead of hot pressed.

The mechanical properties of selected composites were determined on specimens cut from the hot-pressed samples. Those results are summarized in Table 4. As shown, significant levels of flexural strength were observed with the mullite and Al_2O_3-ZrO_2 matrices. While the mechanical properties for the zirconia matrix composites are not extraordinary, they are typical of values reported for fully stabilized zirconia.

Many comparisons can be made between the different sets of mechanical property data. One of the first is the effect of any whisker-matrix interaction (i.e., SCW-75 vs SCW-88 and SCW-85 vs SCW-85A). In every case degradation of the mechanical properties results when any interaction occurs between the matrix and the reinforcement.

Table 4. Summary of mechanical properties of whisker-reinforced low-thermal-conductivity matrices

Sample	Matrix	Reinforcement	Flexural strength[a] (MPa)	Fracture toughness (MPa·$m^{1/2}$)
SCW-49	Mullite	20 vol % SiC whiskers	422	4.7[b]
SCW-49A[c]	Mullite	20 vol % SiC whiskers	490	3.8[d]
SCW-50	Mullite	10 vol % SiC whiskers	419	3.6[b]
SCW-81	Mullite	20 vol % Si_3N_4 whiskers	268	
SCW-81A[e]	Mullite	20 vol % Si_3N_4 whiskers	388	1.6[d]
SCW-75[f]	Zirconia[g]	20 vol % Si_3N_4 whiskers	108	
SCW-88	Zirconia[g]	20 vol % Si_3N_4 whiskers	125	
SCW-85[f]	Al_2O_3—12 vol % ZrO_2	20 vol % SiC whiskers	390	8.4[d]
SCW-85A	Al_2O_3—12 vol % ZrO_2	20 vol % SiC whiskers	675	7.8[d]

[a]Measured by four-point-bend test.

[b]Measured by applied moment double cantilever beam method.

[c]Smaller grain size than SCW-49.

[d]Measured by multiple indent method.

[e]Smaller grain size than SCW-81.

[f]Reaction occurred between matrix and whiskers.

[g]Stabilized with 12 wt % Y_2O_3.

The type of whiskers (SiC vs Si_3N_4) also affects the final mechanical properties. Comparing the mullite matrix composites indicates that the SiC whiskers are more effective as a reinforcement than the Si_3N_4 whiskers are. The reasons for this difference are unclear at the present time. Differences in whisker size distributions, chemical interactions, and processing procedures may all contribute to the disparity in the final properties.

By using a comparative method[3] the thermal conductivities of several ceramic composite samples have been determined near room temperature. The results are presented in Table 5, and tests with standard specimens[1] show that the experimental uncertainty is 3% or less. Data for a hot-pressed Al_2O_3 sample are also included, and these thermal conductivity values are about 10% smaller than the recommended values[3] for this compound.

Additions of 20 vol % SiC whiskers increase the thermal conductivities of both Al_2O_3 and mullite, but the percentage change is larger for the mullite. The values for mullite–20 vol % SiC are about 25% larger than literature data[4] for this compound. The results for hot-pressed Al_2O_3–20 vol % SiC also show that the thermal conductivity does not depend on sample (SiC whisker) orientation.

Table 5. Thermal conductivity values for SiC-toughened ceramics

Sample	Temperature	Thermal conductivity (W/m·K)
Al_2O_3 (hot pressed)	303.6	32.3
	331.6	29.0
	362.6	26.1
Al_2O_3–5 vol % SiC[a] (sintered)	303.2	29.5
	331.6	26.4
	362.9	23.8
Al_2O_3–20 vol % SiC (hot pressed, parallel to pressing direction)	303.3	35.2
	331.5	32.0
	362.8	29.4
Al_2O_3–20 vol % SiC (hot pressed, perpendicular to pressing direction)	303.1	35.1
	331.4	32.1
	362.8	29.5
Mullite–20 vol % SiC (hot pressed)	303.2	7.27
	331.7	7.16
	362.9	7.06

[a]Sample also contained sintering aids that formed a glassy phase at grain boundaries. Results cannot be compared with those for hot-pressed samples.

Status of milestones

The following milestone was scheduled for completion in this reporting period.

Milestone: Complete initial investigation of whisker-reinforced low-thermal-conductivity matrix composites. Submit progress report. March 1985.

The milestone was completed, and the results are summarized in the bimonthly progress report and in the program semiannual report. All other milestones are on schedule.

References

1. T. N. Tiegs et al., "SiC-Whisker-Reinforced Ceramic Composites," pp. 36–39 in *Ceramic Technology for Advanced Heat Engines Project Semiannual Progress Report for Period April 1984–September 1984*, ORNL/TM-9497, February 1985.

2. T. Y. Tien, University of Michigan, unpublished results.

3. R. K. Williams, R. K. Nanstad, R. S. Graves, and R. G. Berggren, *J. Nucl. Mater.* **115**, 211–15 (1983).

4. "Thermal Conductivity: Nonmetallic Solids," p. 254 in *Thermophysical Properties of Matter*, Vol. 2, Y. S. Touloukian, R. W. Powell, C. Y. Ho, and P. G. Klemens, IFI/Plenum, New York, 1970.

Sol-Gel Oxide Powder — W. D. Bond, P. Angelini, P. F. Becher, and T. N. Tiegs (Oak Ridge National Laboratory)

Objective/scope

Sol-gel processes have the potential for the synthesis of materials that can be processed at modest temperatures while obtaining highly uniform composition in dense fine-grain ceramics that incorporate dispersed second phases to increase fracture toughness. This research emphasizes the determination of the feasibility of sol-gel processes for synthesizing powders of phase-stabilized zirconia and alumina and for coating whiskers to control their interface properties to matrix phases. Sol-gel processes take advantage of the high degree of homogeneity that can be achieved by mixing on the colloidal scale and the surface properties of the colloidal particles. The excellent bonding and sintering properties of colloids are a result of their very high specific surface energy.

Work conducted on sol-gel oxide powder synthesis and processing within this program is part of an integrated activity which is also supported by the DOE Materials Sciences Program at Oak Ridge National Laboratory (ORNL). The Materials Sciences supported research on ceramic composites derived from the sol-gel powders resulting from this work. The research on the coating of whiskers by sol-gel methods is done in a collaborative effort with the research on SiC whisker-reinforced composites under way at ORNL in the Industrial Conservation Program. The Industrial Conservation Research includes the necessary research on the fabrication and properties of composites reinforced with the sol-gel-coated whiskers.

Technical progress

Sol-gel studies this report period were concerned with a study of the effect of temperature on the precipitation of hydrous alumina by urea hydrolysis, the effects of the pH and concentration of alumina sols in the coating of SiC whiskers by sol-gel methods, and the preparation of gel-derived powders of ZrO_2-HfO_2. The powders ZrO_2-HfO_2 will be evaluated in the Material Sciences Program with regard to the high-temperature (up to 1000°C) stability of the tetragonal ZrO_2 phase.

The rates of precipitation of hydrous alumina and the nature of the precipitates produced by thermal hydrolysis of urea were investigated. Precipitations were effected by heating 1 L of a 0.1 M $AlNO_3$—0.1 M NH_4NO_3 solution in a reflux vessel in three experimental runs at temperatures of 60, 70, and 80°C. The time required for precipitation was observed visually. The precipitates were separated by centrifugation, washed free of NH_4NO_3, dried in air at ambient temperatures, and examined visually in a microscope. The precipitation rates were very slow, requiring about 5 days at 60°C and about 3 days at 80°C. Gel precipitates were formed at the lower temperature conditions (60 and 70°C), whereas granular precipitates were formed at 80°C. The average size of the precipitated particles was about 1 μm, and the particles formed at 60°C appeared to be the most uniform in size.

Preparations of alumina-coated SiC whiskers by sorption of colloidal alumina from sols were investigated with regard to effects of the pH and Al_2O_3 concentration of the sols. To promote good contact during coating, ultrasonic agitation was used to disperse the SiC whiskers into an aqueous Al_2O_3 concentration of the sols. Experiments have been carried out with sols at two concentration levels of Al_2O_3 (11 and 34 g/L). In each experiment, 0.5 g of SiC whiskers were coated while holding the mass ratio of Al_2O_3 to SiC constant at 1.7. Examination of the coated whiskers by electron microscopy showed that the whiskers were completely coated at all conditions and that the coating thickness increased with increasing Al_2O_3 concentration and decreasing pH of the sol. The coatings applied at pH = 3.5 were very uniform, whereas the coatings at pH = 2.5 were not. The coatings formed at pH = 2.5 were not uniform in thickness along the lengths of the whiskers.

Gel powders were prepared by direct gelation and by gelation of precursor ZrO_2-HfO_2 hydrosols. Both methods were used to prepare several 20-g batches of glassy, semi-transparent, ZrO_2-HfO_2 gel particles containing 8 and 16 wt % HfO_2. In the direct gelation method, the ZrO_2-HfO_2 gels were precipitated by using a large excess of 8 M NH_4OH at 25°C. The gel precipitation was carried out by slowly adding a 0.3 M solution of the metal salts (1.5 mL/min) to 1 L of 8 M NH_4OH while rapidly stirring. At 25°C, gel precipitates were obtained by this procedure, whereas at 50°C granular precipitates resulted. The gel was separated from the mother liquor by filtration. Subsequently, the gel filter cake was washed and dried. Gels were prepared from ZrO_2-HfO_2 precursor sols by water evaporation. The ZrO_2-HfO_2 sols were synthesized from ZrO_2-HfO_2 gel precipitates that were precipitated by the direct gelation procedure.

Important findings and observations

Initial results of the influence of Al_2O_3 concentration and pH sols on the coating thickness of alumina-coated SiC whiskers suggest that the coating process is governed by typical adsorption isotherms for colloidal particles. According to these isotherms, the magnitude of the driving force for adsorption is increased by increasing the solution concentrations of the colloidal sorbate and by increasing electrostatic attraction between the colloidal sorbate particles (e.g., Al_2O_3) and sorbent surface (e.g., SiC). The pH of the system determines the electrostatic attraction because the H^+ or OH^- ion concentrations determine the sign of the charges on the colloidal sorbate particles and on the sorbent surface and the magnitude of those charges.

Advanced Transformation-Toughened Oxides
(University of Michigan)

No report received.

1.2.4 Silicate Matrix

Mullite SiC Whisker Composites

S. Musikent and S. Samento (General Electric Company)

OBJECTIVE/SCOPE

The objective of this program is to develop high toughness, high strength, refractory ceramic matrix composites which are amenable to low cost, near net shape forming for application to automotive engines.

In this program, the General Electric Company, Space Systems Division, is pursuing the development of SiC whisker reinforced mullite (3 Al_2O_3 2 SiO_2) matrix ceramic composite. In addition, the enhancement of the mullite matrix fracture toughness by the incorporation of transformation toughening by additions of $Zr_{0.5}Hf_{0.5}O_2$ is proposed. This mullite matrix composite can meet a very significant need in the ceramic heat engine technology. That specific need is for a low thermal conductivity, high strength, tough, hard and wear resistant ceramic with intrinsically good thermal shock resistance. The intrinsically good thermal shock resistance is due to mullite's moderately low modulus of elasticity, $\sim 30 \times 10^6$ psi (207 GPa), and relatively low coefficient of thermal expansion (CTE), 5 x 10^{-6}/°C, as well as good levels of strength. The thermal conductivity is low, being approximately equal to that of ZrO_2. Since the coefficient of thermal expansion (CTE) is about half that of ZrO_2, mullite experiences far lower thermal stresses than ZrO_2 when exposed to the same thermal gradient.

Similarly, in comparison to alumina, mullite is intrinsically superior with respect to thermal shock because of mullite's lower CTE and lower modulus of elasticity. Any matrix with a high CTE tends to have lower resistance to thermal shock.

The initial aim of the investigation is to prepare a composite with fracture toughness of $\geq$ 4.0 MPa$\sqrt{m}$.

In order to achieve this goal, we have initiated investigation of the mullite-SiC whiskers compositions with varying parameters. The major steps in this investigation are as follows:

1. Prepare mullite/SiC whisker compositions using fine particle size mullite powder. Whisker compositions may range between 15 and 30 wt %. Whiskers may be milled for size reduction before incorporating into a batch composition.

2. Investigate sintering aids which will assist in composite consolidation.

3. Investigate the addition of a transformation toughening agent, $Zr_{0.5}Hf_{0.5}O_2$, to mullite/SiC compositions to enhance the fracture toughness of the matrix material.

4. Consolidation methods include:

   (a) Cold isostatic pressing and sintering.
   (b) Hot isostatic pressing (HIP).
   (c) Cold isostatic pressing (CIP), sintering, and hot isostatic pressing (HIP).

5. Explore the application of coating materials to whiskers to control the bonding strength of whisker to matrix; incorporate diffusion barriers at the whisker/matrix interface to minimize chemical reactions between the matrix and whisker.

6. Characterize the composites for mechanical, physical, chemical and thermal properties at room temperature and at elevated temperatures.

TECHNICAL HIGHLIGHTS

Summary of Work to Date

In the previous reporting period, mullite/SiC whisker composites were prepared with 20 w/o and 30 w/o as received SiC whisker content. The highest density after sintering measured was 85% of theoretical density which is too low for practical usefulness and also, due to connected porosity, too low to subject to hot isostatic pressing operation without canning. The key issue identified in this early work is to achieve a sufficiently high density composite by sintering without resorting to hot pressing. If this can be accomplished, then a containerless HIP'ing operation can be expected to fully densify the composite.

During the current reporting period we have investigated three different approaches to achieving higher density including:

1) Milling of whiskers to reduce the l/d ratio and thus enhance ability to densify during sintering.

2) The use of a SiO_2-Al_2O_3 glass plus additions of Al_2O_3 to achieve a liquid phase during sintering followed by diffusion of the excess Al_2O_3 into the glassy phase to approach the mullite composition.

3) The use of Nb_2O_5 as a sintering aid as well as for its potential to form a carbide diffusion barrier on the SiC whisker.

A series of sintering experiments were conducted and the highest density achieved was 90.8% using mullite, milled SiC whiskers and Nb_2O_5 in a 70/30/10 weight ratio. These experiments as well as the earlier ones previously reported are summarized in Table I and in the following paragraphs.

Compositions 1 through 3 were composed of mullite powder and as received Arco SiC whiskers.

Compositions 4 through 7 were composed of mullite powder, as received ARCO Sic whiskers and two compositions of SiO_2-Al_2O_3 glasses. The SiO_2-Al_2O_3 phase diagram shows a eutectic glass at approximately 4.2 m/o Al_2O_3 (Ref. "Phase Diagrams for Ceramics", E. M. Levin, C. R. Robbins, and H. F. McMurdie, American Ceramic Society, 1964). In each of these batches, additional alumina was added in an attempt to achieve a stoichiometric mullite matrix in the final sintered body.

In compositions 8 through 12, the effect of milling the SiC whiskers was investigated. In general, the milling of the SiC increased the densities to the 87% of theoretical density range.

Compositions 13 and 14 incorporated Nb_2O_5 as a sintering aid. Sample 14 achieved the highest density, 90.8% of theoretical, in this series of experiments.

Composition 15 was similar to composition 1, except that the mullite whisker mixture was prepared as a slury with pH adjustments to attempt to achieve a more homogeneous dispersion of the whiskers in the mullite matrix. The slurry was concentrated by boiling off the water, dried and further processed as described in Table I.

DISCUSSION

During this reporting period, we have prepared mullite - SiC whiskers (70/30 wt %) compositions with and without an additive or a sintering aid. The baseline mullite (Baikowski mullite, planetary ball milled 1 ½ hours), Baikowski mullite ball milled for 48 hours, and a newly available, deagglomerated, finer particle size variety of mullite from Baikowski Corp. were investigated as the starting matrix material.

SiC whiskers from Arco Metals Co. were also milled for various periods of time to obtain shorter (lower l/d) fibers before incorporating into a mix composition. Also, we investigated the use of SiO_2-Al_2O_3 glasses (and their subsequent re-crystallization to mullite) and niobium oxide, Nb_2O_5, in order to promote sintering by the presence of a liquid phase at the sintering temperature (1650°-1670°C). A few compositions were also tried with ZrO_2-HfO_2 (1:1 molar) addition to achieve transformation toughening in the system. The compositions investigated along with their processing methods and densitites of sintered composites are summarized in Table I. In general, powder mullite-SiC whisker batches were cold isostatically pressed (CIP) at 40-55 KSI and sintered in air at 1650-1670°C for 2-3 hours. Sintered composite billets exhibited a thin oxidized, white layer on the surface. A small piece from inside (greenish) was saw cut from each billet for density determination.

As seen in Table I, density of the sintered composites ranged between approx. 80-91% theoretical. The highest density of about 91% theoretical was obtained with the composition #14 containing 10 weight % Nb_2O_5. Sintered specimens containing Nb_2O_5 have a blackish color (probably due to NbC formation), unlike other materials, which are similar to the original greenish color of SiC whiskers. Based on the data shown, several other observations are mentioned as follows:

(1) New, as-received, deagglomerated Baikowski mullite is supereior to the milled earlier Baikowski mullite.

(2) Use of SiO_2-Al_2O_3 glasses (composition nos. 4-7, Table I) in the composites batches did not develop sufficient liquid phase(s) to improve densification of the material at the sintering temperature. The use of such glasses and other sintering aids needs to be investigated further.

(3) Addition of a toughening agent, such as, ZrO_2-HfO_2, did not exhibit any transformation toughening in the system, probably because of the high porosity in the sintered composite.

(4) Use of slightly milled SiC whiskers improves the composite density (comps. #10-14). Milling the as-received (10-80μm) whiskers for about ½ hour, wet or dry, in a planetary ball mill breaks down the major fraction of the fibers to $\leq$ 10-12μm in length.

Figures 1 and 2 show SEM photomicrographs of SiC whiskers in batch composition #10 (whiskers wet milled in PBM for ½ hour) and after ½ hr PBM dry (whiskers used in compositions #13 and 14). Figures 3 and 4 show fiber structures in powder batches of the compositions #11 and 12 respectively. Figure 5 shows the presence of much longer whiskers in a batch of composition #15 prepared by wet dispersion and with unmilled whiskers.

A few small pieces of sintered mullite-SiC whisker composites were also sent to GE-CR&D, Schenectady, NY for canning/encapsulating in a Mo foil by electron beam welding for HIP'ing experiments. Initial weldings of the foils were not successful. Further work is under way.

WORK PLANNED

During the next reporting period, the following tasks are planned:

(1) Continue to investigate the use of a glass Nb_2O_5 or other sintering aid(s) to achieve further densification during sintering of mullite - SiC whiskers composites. The principal aim is to achieve high enough density (no open porosity) of a sintered composite, which could be densified further by hot isostatic pressing (HIP).

(2) Investigate HIP'ing of a sintered composite(s) after encapsulation in a refractory metal (Mo or Ta) or glass to produce a denser composite.

(3) Further investigate wet dispersion technique to produce more homogeneous batch compositions of mullite and milled SiC whiskers.

(4) Study of mechanical properties and microstructures of a few selected composites prepared.

STATUS OF MILESTONES

Table II, contract management summary report, lists the milestone plan and our current status. At this time, milestones 1.1, 1.2 are complete. Milestone 1.3, Characterize Initial Specimens, is partially complete. However, to date we have not achieved, by sintering, properties equivalent to those of the hot pressed samples made during our earlier IR&D program and reported in our Proposal C-03083 (January 24, 1984). Until we achieve densities in the range of 95% of theoretical, we will hold up on any extensive characterization.

Likewise, Milestone 3.1, Detailed Test Plan, has been held up pending achievement of higher density samples. However, this task will be completed during the next reporting period.

COMMUNICATIONS/VISITS/TRAVEL

During this period a progam review was conducted (March 12, 1985) at General Electric Co. with T. Tiegs and D. R. Johnson.

PUBLICATIONS

No publications have been prepared on the work to date. However, a paper based on our earlier IR&D study on the same subject was delivered at the American Ceramic Society Symposium on Composites and Advanced Ceramics, Cocoa Beach, FL, January 1985: "SiC Whiskers Reinforced Ceramic Matrix Composites", S. C. Samanta and S. Musikant.

PROBLEMS ENCOUNTERED

The primary objective in the present stage of this investigation is to achieve a high density composite without resorting to hot pressing. So far we have achieved a maximum of 90.8% of theoretical using a 70:30:10 weight ratio of mullite: milled SiC whiskers: Nb_2O_5. Nb_2O_5 has a melting point of 1479°C.

Future work will attempt to achieve a higher density by sintering prior to containerless HIP'ing.

Table I

Mullite-Sic Whisker Composites Prepared

NO.	COMPOSITION	PARTS BY WEIGHT	PROCESSING CONDITIONS	DENSITY (% THEORETICAL)
1	Mullite (1) SiC Whiskers	70 30	Blended in planetary mill for 15 minutes, cold isostatically pressed at 40,000 psi and sintered at 1650°C in air for 3 hours. Sintered billets ≈ 2.5" X 1.0" X 1.0"	84.6
2	Mullite (1)/1:1 molar ZrO_2-HfO_2 SiC Whiskers	70 30	"	84.5
3	Mullite (2) SiC Whiskers	70	"	85.5
4	Mullite (2) SiC Whiskers Glass I Alumina	70 30 10 24	Same as above, except the powder batch was CIP-ed at 55,000 psi	82.6
5	Mullite (2) SiC Whiskers Glass I Alumina	70 30 30 72	"	80.0
6	Mullite (2) SiC Whiskers Glass II Alumina	70 30 10 18.5	Same as above, except sintered at 1670°C/3 hrs	81.4
7	Mullite (2) SiC Whiskers Glass II Alumina	70 30 30 55.5	"	81.3

Table I (Continued)

NO.	COMPOSITION	PARTS BY WEIGHT	PROCESSING CONDITIONS	DENSITY (% THEORETICAL)
8	Mullite (3) SiC Whiskers (Milled)	70 30	Same as bove, except sintered at 1650°C/3 hrs 4 billets _ 1.0" X 0.6" X 0.6"	83.6
9	Mullite (3)/1:1 ZrO_2-HfO_2 SiC Whiskers (Milled)	70 30	"	85.4
10	Mullite (3) SiC Whiskers (Wet milled 1/2 hour)	70 30	Same as above, except sintered at 1670°C/3 hrs.	88.0
11	Mullite (3) SiC Whiskers (Wet Milled 1 hour)	70 30	"	87.7
12	Mullite (3) SiC Whiskers (Wet Milled 2 hours)	70 30	"	86.0
13	Mullite (3) SiC Whiskers (dry milled 1/2 hour) Nb_2O_5	70 30 5	Same as above, except sintered at 1670°C/2hrs.	86.6
14	Mullite (3) SiC Whiskers (dry milled 1/2 Hour) Nb_2O_5	70 30 10	"	90.8

Table I (Continued)

NO.	COMPOSITION	PARTS BY WEIGHT	PROCESSING CONDITIONS	DENSITY (% THEORETICAL)
15	Mullite (3) SiC Whiskers	70 30	Prepared by wet dispersion on mixing in a Waring blender at PH 11.0, re-adjusted the PH to 7.0, concentrated the slurry by boiling off water and then dried. Dry batch powder CIP-ed at 55,000 psi, and sintered at 1670°C/ 3 hrs.	84.6

NOTE: Raw Materials

Mullite (1) - Baikowski mullite, ball milled, wet, 48 hours, dried and planetary ball milled, dry, 15 minutes.
1:1 molar ZrO_2-HfO_2 - Prepared by sol-gel method, calcined 750°C/2 hours, wet planetary ball milled 8 hours, dried and then planetary ball milled for 15 minutes.
SiC Whiskers - SILAR SC-9 from ARCO Metals Co.
Mullite (2) - New, deagglormerated, as-received Baikowski Mullite
Glass I - SiO_2/Al_2O_3, 95/5 mole %, melted and ground, - 325 mesh
Glass II - SiO_2/Al_2O_3, 85/15 mole %, melted and ground, - 325 mesh
Alumina - Nortion Co, grade 38-900
SiC Whiskers (milled) - SILAR Sc-9 whiskers milled in a planetary ball mill for 10 minutes
Mullite (1)/1:1 ZrO_2-HfO_2 - 90/10 Vol %
Mullite (3)/1:1 ZrO_2-HfO_2 - 90/10 Vol %
Mullite (3) - Baikowski mullite, planetary ball milled, wet, 1 1/2 hours, dried and then planetary ball milled, dry, for 15 minutes
SiC Whiskers (compositions 10,11 & 12) - wet milled in planetary ball mill for 1/2 hr., 1 hr, & 2 hrs., respectively; dried & then PBM dry, 15 min.
SiC Whiskers (compositions 13 & 14) - PBM, dry, 1/2 hour
Nb_2O_5 - Kenametal Co.

Table II

Development of Ceramic Matrix Composites for Application in the Ceramic Technology for Advanced Heat Engine Program - Mullite Si C Whisker Composites Subcontract 86X-00218C

Milestone Schedule

Task		Date
1.	Feasibility demonstration	
1.1	Establish performance goals	12/14/84
1.2	Fabricate initial specimens	1/7/85
1.3	Characterize initial specimens	2/1/85
2.	Develop process flow sheets	
2.1	Develop low cost near net shape process	
	Fabricate initial liquid phase sintered specimens	4/1/85
	Fabricate initial HIP specimens	4/5/85
	Fabricate improved liquid phase sintered specimens	8/2/85
	Fabricate improved HIP specimens	8/2/85
	Select best process for optimization	1/3/86
2.2	Develop optimized process	
	Document optimized process flow sheet for intermediate level of optimization	5/2/86
	Document process flow sheet for final level of optimization	8/1/86
3.0	Property measurements	
3.1	Characterize microstructure of each stage of process development	
	initial	5/3/85
	improved	9/6/85

December 1, 1984

Task		Date
3.1	intermediate optimization	5/2/86
	final optimization	8/1/86
3.2	Submit detailed test plan to ORNL	2/1/85
3.3	Property measurements	
3.3.1	(a) Measure MOR, K_{IC} at RT and 1200C	5/3/85
	(b) Measure MOR, E, K_{IC} CTE, k at RT and 1200C.	9/6/85
	Thermal soak at 1000C/500 hrs. and repeat tests.	
	(c) Repeat (b)	7/4/86
3.3.2	Perform cyclic fatigue test and fatigue crack	5/16/86
	propagation test	
3.3.3	Model MOR of composite	8/16/85
3.3.4	Perform thermal shock analyis	8/15/86
4.0	Reports	
	Milestone schedule	12/1/84
	Bimonthly reports	1/15/85 3/15/85 5/15/85 7/15/85 9/15/85 11/15/85 1/15/86 3/15/86 5/15/86 7/15/86
	Semi annual reports	6/15/85 12/15/85 6/15/86
	Final report	10/31/86

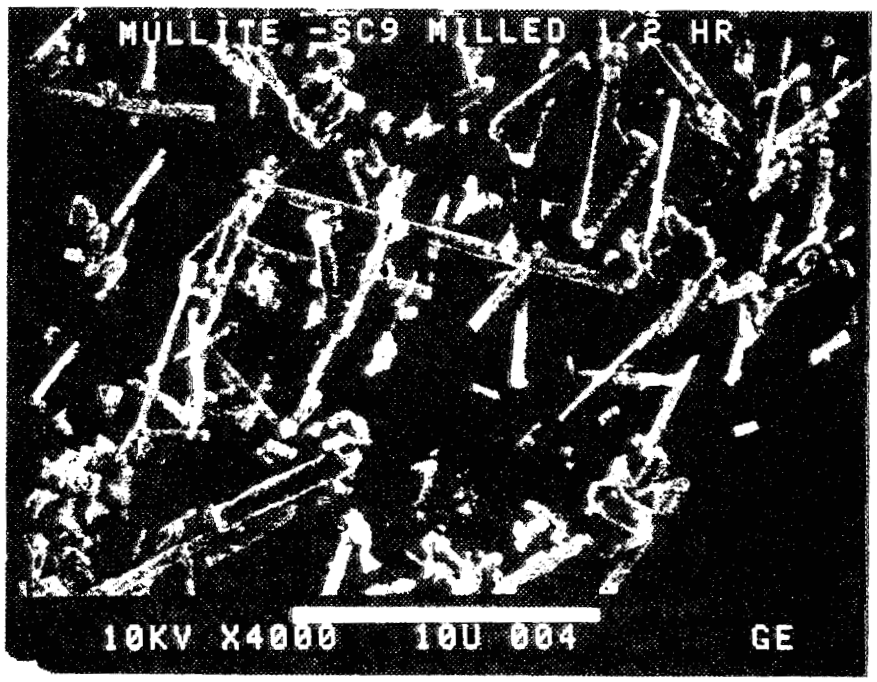

Figure 1: 1/2 hour PBM, wet, SiC whiskers in composition #10 batch

Figure 2: 1/2 hour PBM, dry, SiC whiskers

Figure 3: 1 hour PBM, wet, SiC whiskers in composition #11 batch

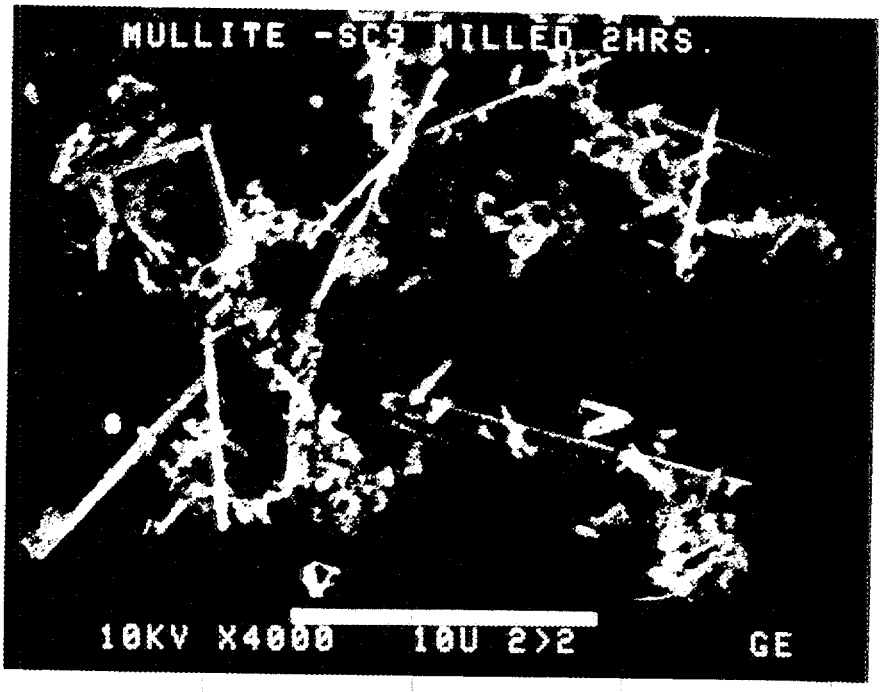

Figure 4: 2 hours PBM, wet, siC whiskers in composition #12 batch

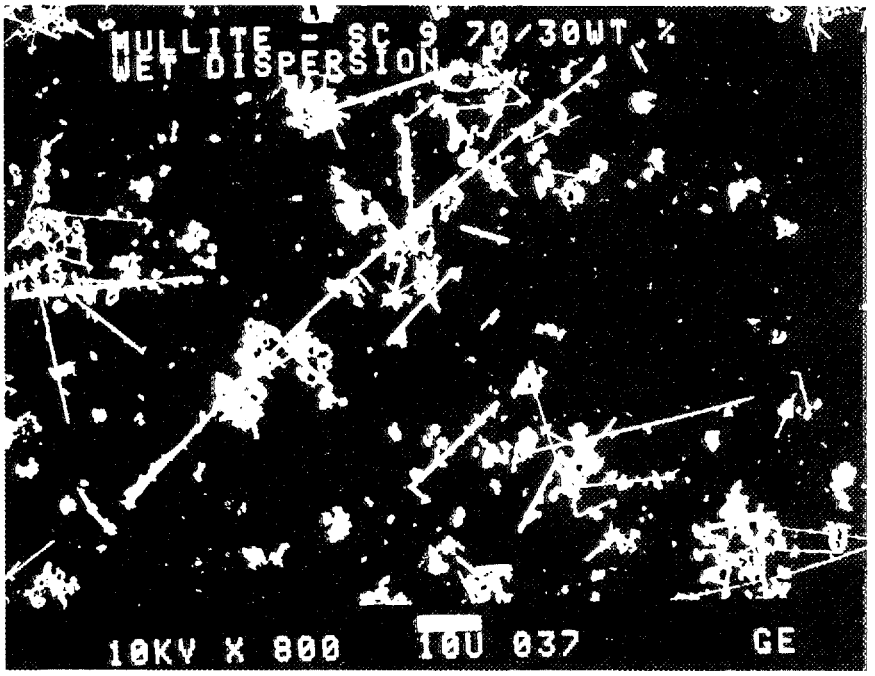

Figure 5: Unmilled SiC whiskers in batch composition #15

1.3 THERMAL AND WEAR COATINGS

1.3.2 ZrO_2–Cr_2O_3 Coating Evaluation

ZrO_2–Cr_2O_3 Coating Evaluation

T. M. Yonushonis (Cummins Engine Company, Inc.)

Objective/Scope

The objective of this program is to improve the understanding of the processing-microstructure-property relationships of chrome oxide based coatings and chrome oxide infiltrated plasma sprayed zirconia. The chrome oxide wear coatings have been applied to cylinder liners for wear protection, while plasma sprayed zirconia has been used for thermal protection of piston crowns in advanced adiabatic engines.

The tasks and subtasks for this program are as follows:

Task 1 - Microstructural and Property Characterization
- A - Microstructural and Chemical Analysis
- B - Thermal Stability and Thermal Fatigue
- C - Thermal Conductivity
- D - Mechanical Properties

Task 2 - Friction and Wear Characteristics

Task 3 - Post Engine Test Coating Characterization

It is anticipated that this 24 month program will provide detailed characterization procedures, design properties, and improved ceramic coatings for wear resistant surfaces and thermal barrier surfaces utilized in advanced adiabatic diesel engines.

Technical Progress

Task 1A - Microstructural and Chemical Analysis

Most characterization efforts on this task during this reporting period have been conducted at the University of Illinois under the direction of Irena Dumler. TEM, SEM, and electron microprobe analysis have been used to analyze the Kaman Sciences coatings and the Plasma Technics plasma sprayed zirconia. Data reduction is in-progress on these samples.

Results of the optical analysis were reported in the previous semiannual report.

Task 1B - Thermal Stability and Thermal Fatigue

Static oxidation tests of the chrome oxide and plasma spray coatings have been completed at 538°C (1000°F) for 1000 hours. Optical microscopy of cross sections of the samples revealed that the iron/coating interface was deteriorating due to oxidation of the iron. Improved substrate materials will be required if 538°C (1000°F) metal temperatures are required in advanced diesel engines.

Task 1C - Thermal Conductivity

No activity during this reporting period.

Task 1D - Mechanical Properties

Vickers hardness values were obtained for the Kaman SCA on cast iron at approximately 25°C, 250°C, 400°C, and 500°C at ORNL with the assistance of Wayne Clark. The coating hardnesses were measured at 500 gram and 1000 gram loads in vacuum. Vickers hardness was calculated using the formula:

$$DPH = \frac{2\ P\ SIN\ \Theta/2}{d^2}$$ where P = load in Kg
$\Theta = 136°$
d = diagonal length in mm

Vickers hardness values are reported in the following Table:

Vickers Hardness

Approximate Temperature	Average (Kg/mm^2)	Standard Deviation (Kg/mm^2)	Number of Tests
500 Gram Load			
25°C	468	39	3
250°C	517	120	9
425°C	432	62	8
1000 Gram Load			
260°C	417	16.8	5
400°C	371	65	9
500°C	332	71	6

Analysis of the 500 gram data by a T-statistic revealed that the coating hardness did not change over the temperature range tested. Calculation of the indentation depths based on diamond geometry confirmed indentation depths did not exceed the coating thickness. Indentation depth was approximately 1/5 to 1/3 the coating thickness.

Hardness values were lower than normal for this material based on comparison to other values which is probably related to a slightly different measurement technique. Therefore, hardness values reported in the previous table can only be used for relative comparisons within the table. The difficulty in finding the impressions forced us to use another microscope for measurements of the indentations.

Dr. Graham, Pennsylvania State University, has had some difficulties measuring the elastic modulus of the chrome oxide and plasma sprayed zirconia coatings on the iron substrates because of ultrasonic attenuation of the iron. Another set of coatings on steel substrates appears to minimize this problem and the effort is progressing.

An investigation was conducted to determine the adherence and fracture toughness of three coatings: SCA, zirconia, and SCA infiltrated zirconia. This effort also develops coating mechanical property data of coatings in diesel engines that is critical for successful application.

A Vickers diamond indentation technique was evaluated as a means of determining coating adherence and fracture toughness. A second method, double cantilever beam (DCB), was used to establish a lower bound for SCA fracture toughness. The information generated by these techniques can be used to predict coating performance and to develop improved coatings.

Pask Research and Engineering has evaluated the indentation method of determining coating adherence and coating fracture toughness.

A summary of the major findings of the indentation method were as follows:

- The Kaman SCA coating contained many cracks and porosity. These defects prevented Pask Research and Engineering from measuring the fracture toughness of the coating.
- Significant differences in crack lengths were observed at the edges of the indentation for cracks parallel and perpendicular to the plasma spray direction in the plasma sprayed zirconia. This result indicates residual stresses, anisotropy of material, or both. Toughness was greater normal to the surface than parallel to the surface by approximately 145%.

- Hardness of the zirconia was affected by the SCA treatment. However, the fracture toughness appeared unaffected by the SCA treatment as shown in the following table. This result indicates that the SCA treatment does not substantially improve the bond strength of plasma sprayed zirconia.

Hardness and Toughness of SCA Infiltrated Zirconia

		Toughness, $MPa^{1/2}$ (KSI in)		
Location	Hardness, Kg/mm^2	Parallel to Surface		Normal to Surface
Near SCA Layer	1200 ± 80	2.1 ± 0.5	(1.9 ± 0.5)	3.0 ± 0.6 (2.8 ± 0.6)
Center of ZrO_2	1050 ± 60	2.0 ± 0.5	(1.8 ± 0.5)	2.9 ± 0.6 (2.7 ± 0.6)
Near Bond Coating	960 ± 80	2.0 ± 0.5	(1.8 ± 0.5)	3.2 ± 0.6 (2.9 ± 0.6)

A DCB Technique [1] was used to determine the lower bounds of fracture toughness for the Kaman SCA coating at Cummins. The technique was considered to yield a lower bound fracture toughness due to the change in coating application method necessary to obtain samples. Although the processing was identical to SCA processing the method of bonding cast iron cantilevers was not previously attempted by Kaman Science. The following figure shows a schematic of the DCB specimen with a thin layer of SCA coating between the cantilever beams.

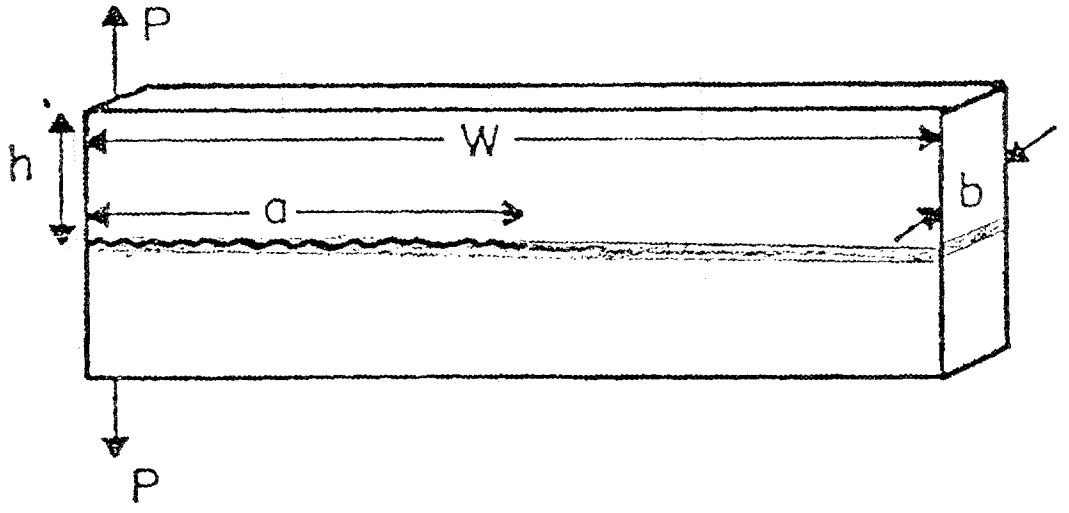
P
h
W
a
b
P

The DCB samples were precracked in tension using an Instron at 0.002 in/min crosshead speed. The crack length was determined by a binocular microscope and measured with a scale. The sample was then placed in the Instron for rapid fracture at a 0.2 in/min crosshead speed. Table 1 presents the data. Fracture toughness was calculated by the following formula [1].

$$K_{IC} = 3.45 \frac{pa}{b\, h^{3/2}} \left[1 + 0.7 \left(\frac{h}{a}\right)\right]$$

where h = 0.4 in.
b = 0.05 in.
w = 2.75 in

Fracture Toughness values are shown in the following table.

DCB Test Data and Fracture Toughness of Kaman SCA

Test #	Crack Length (in)	Pop In Load (lbf)	K_{IC} Load (lbf)	K_{IC} (MPa $m^{1/2}$)	K_{IC} KSI $\sqrt{in}$
1	1.79	45	2.4	1.47	1.35
2	0.66	27	4.4	1.23	1.13
3	0.93	27.5	4.0	1.44	1.32
4	0.64	29	5.1	1.40	1.28

Average K_{IC} = 1.39 MPam $^{1/2}$ (1.27 KSI $\sqrt{in}$)
S.D = 0.099 MPam $^{1/2}$

Average fracture toughness was 1.39 MPa $m^{1/2}$ (1.27 KSI $\sqrt{in}$) which is approximately double the fracture toughness of glass [2] and approximately equivalent to porcelain enamels [3].. This fracture toughness value is considerably lowered than cast iron, 44 $MPam^{1/2}$ (40 KSI $\sqrt{in}$.) Therefore, the Kaman SCA is much less tolerant to damage than cast iron.

References For Section 1.0

1. A.G.Evans, "Fracture Mechanics Determinations", in Fracture Mechanics of Ceramics, Vol 1, edited by R.C.Bradt, D.P.H. Hasselman, and F.F.Lange (1973).

2. S.M.Wiederhorn, A.G.Evans, and D.E.Roberts, "A Fracture Mechanics Study of Skylab Windows", Fracture Mechanics of Ceramics, Vol 2, edited by R.C.Bradt, D.P.H. Hasselman, and F.F.Lange (1974).
3. W.G.Clark,Jr. and W.A.Logsdon, "The Applicability of Fracture Mechanics Technology To Porcelain", Fracture Mechanics of Ceramics, Vol 2, edited by R.C.Bradt, D.P.H. Hasselman, and F.F.Lange (1974).

Task 2 - Friction and Wear Tests

A statistical experimental design approach was selected for this wear test investigation.

Test matrix was comprised using the following constants and variables.

Test Conditions

Constants	Variables
Speed - 500 rpm	Ring coating - CrC + Mo - Al_2O_3 + TiO_2
Oil Temperature - 175°C (350°F)	Block Coating - gray iron, (no coating)
Test Time - 15 Hours	Kaman SCA 10X C-1
Ring Diameter - 34.99 mm (1.3775 in.)	Oil Type - Life Oil (SDL-1 Type)
Block Width - 6.35 mm (0.25 in)	Exxon 7808 (Mil-L-23699)
	Initial Stress Level -
	High - Approximately 400 MPa (60 KSI)
	Low - Approximately 200 MPa (30 KSI)

The following fractional factorial design matrix was developed to determine the influence of coating type, lubricant, and stress level on the total test block wear.

Fractional Factorial Design Matrix

Ring Coating	Liner Coating: Kaman SCA 10X C-1				Liner Coating: Gray Iron From Liner Coating			
	1	2	1	2	1	2	1	2
CrC + Mo	1*	2	2	1	1	2	2	1
$Al_2O_3 + TiO_2$	2	1	1	2	2	1	1	2

* Number of tests
Oil 1 - Life
Oil 2 - Exxon 2380

1 = 400 MPa initial
2 = 200 MPa initial

The materials selected for this investigation are being evaluated for wear control in advanced engines. A low alloy gray iron liner was selected as a baseline, since it represents a standard cylinder liner material. A liner coating consisting of $SiO_2/Cr_2O_3/Al_2O_3$** was also selected. The ring coatings included plasma sprayed Cr_3C_2/NiCr/Mo* and Al_2O_3/TiO_2*.

A block-on-ring test machine***, ASTM Practices G77-83, was used to determine the wear volumes and frictional behavior of the materials.

A 2^4 factorial experimental design was used to minimize the number of tests and assist in interpretation of the results. In this testing, one-half of the matrix was replicated. The model statement selected was to evaluate the major effects of liner coating, ring coating, lubricant, load and two-way interactions between the major effects.

* Kopper's Co., Baltimore, MD
** Kaman Sciences Corp., Colorado Springs, CO
*** Falex Corp., Aurora, IL

The test sequence was randomized. The desired ring, block, lubricant and load combinations were selected, the lubricant reservoir was heated to 175°C, and the testing was initiated. Test duration was 15 hours. The samples were removed and catalogued. The wear was determined by averaging the width of the wear scar in three locations. Frictional forces were obtained from a load cell and these values were recorded during the test.

The coatings and wear scars were examined optically and by scanning electron microscopy.

Ring surface roughness measured by stylus techniques was approximately 0.8 μm AA for the as-ground surfaces. Surface porosity in the plasma sprayed coating was partially responsible for the high surface roughness compared to standard rings, approximately 0.15 μm AA. Block surfaces were 0.5 μm AA which was comparable to standard liner surfaces.

Material characterization revealed that the plasma sprayed ring coatings and the liner coatings had a complex microstructure. X-ray diffraction of the SCA revealed that this coating consisted of α-quartz, chromia, and alumina. Only the NiCr and Mo phases were detected by X-ray diffraction in the Cr_3C_2/NiCr/Mo coating. Al_2O_3 was observed by X-ray diffraction in the Al_2O_3/TiO_2 coating. Energy dispersive X-ray analysis of optical sections was able to detect discrete Cr_3C_2 particles and TiO_2 stringers in the respective coatings. Due to the low volume fraction of Cr_3C_2 the average coating hardness was approximately 480 HK_{500}.

The coefficients of friction and wear volumes obtained from the lubricated block-on-ring tests were analyzed by regression analysis procedures. Wear volume was modeled as log (wear volume) due to a higher correlation coefficient compared to the wear volume model. Mean values of the coefficient of friction and wear volume are shown in the following table.

Mean Value Of The Coefficient Of Friction and Wear Volume

	Number of Tests	μ_f	Wear Volume (mm^3)
Liner Material			
Gray Iron	10	0.16	8.4
SCA	12	0.22	0.4
Lubricant			
MIL-L-23699	10	0.14	0.7
SE/CD 15W-30	12	0.22	6.9
Load			
High	12	0.15	6.7
Low	10	0.23	1.0
Ring Coating			
Al_2O_3/TiO_2	11	0.18	1.2
Cr_3C_2/NiCr/Mo	11	0.20	7.0

Analysis of the interactions revealed that the oil and load have a significant interaction on the measured coefficient of friction. The SE/CD 15W-30 lubricant at low load had a significantly higher average coefficient of friction than any other combination of variables (99% confidence), following table.

Coefficient of Friction For Lubricant/Load Interactions

Lubricant * Load

	Load	
Lubricant	350 N/cm	70 N/cm
MIL-L-23699	0.16	0.12
SE/CD 15W30	0.3	0.14

From this data set, the effects of lubricant and load could not be separated due to the interaction. The other significant factor was that the SCA coating had a higher average friction coefficient than gray iron (96% confidence). Because of this interaction the lubricant and load coefficient of friction could not be separated.

Analysis of the wear volume demonstrated that the high load yielded a higher average wear volume (99% confidence), which was expected. The block and lubricant interaction may be easily seen. The gray iron block tested with SE/CD 15W-30 oil had a higher average wear volume than any other combination tested.

Log (Wear Volumes) For Block/Lubricant Interactions

	Block	
Lubricant	Gray Iron	SCA
MIL-L-23699	-0.44	-0.66
SE/CD 15W-30	+0.83	-0.97

It should be noted, however, that the contact stresses change rapidly with increasing wear scar width. Therefore, the rings tested with the SCA coatings have experienced a higher contact stress throughout the 15 hour test than when the rings were tested against gray iron. This factor complicates the analysis, but a possible trend was observed indicating that greater ring wear may occur when cylinder liners are coated with harder wear resistant coatings.

Surface roughness measurements of the block surfaces and the ring surfaces verified that the surfaces were degrading during the tests. Optical examination of the ring coatings indicated that they had exhibited considerable wear when evaluated with the more wear resistance SCA coating. The gray iron blocks had a negligible effect on the plasma spray ring coatings.

Additional Falex #1 wear testing was completed on two Kaman coatings, DES and C-7. The wear test conditions, 445 N normal load at 500 rpm, resulted in a wear through of the coatings in less than one hour. Tests of these coatings were stopped, since these coatings did not appear to have adequate wear life for liner applications.

Summary - Block-on-ring tests were used to obtain information on the wear behavior and coefficients of friction for boundary lubricated surfaces at conditions which simulate advanced engine operations. Although the test method has considerable short-comings, inadequate temperature capability and varying contact stress with wear, it did yield information on potential problem areas (increased ring wear with harder liner coatings) and detected interactions between lubricant/load combinations and lubricant/liner combinations.

Task 3 - Post Engine Test Coating Characterization

A SCA coated liner which was engine tested at Cummins has been analyzed by Auger microscopy. Because of surface contamination from diesel oil, fuel and other areas, it was not possible to determine if chemical species at the interface prevented bonding during the original processing.

The following table presents the status of the milestones for this investigation.

Major Milestones for "Characterization of Chromium Oxide Based Ceramic Coatings for Advanced Heat Engines

Milestone Identification	Milestones	Approximate Percent Completion
1.3.1.1	Sample Preparation for Task 1 Evaluation from SCA-1002 Family of Silica-Chromia-Alumina, Thin Chromia Coatings and Plasma Spray Zirconia Infiltrated with SCA-1002 or Thin Chromia	95%
1.3.1.2	Task 1 - Microstructural and Property Characterization A - Microstructural and Chemical Analysis B - Thermal Stability and Thermal Fatigue C - Thermal Conductivity D - Mechanical Properties	85%
1.3.1.3	Sample Preparation for Task 2 Friction and Wear Tests	95%
1.3.1.4	Task 2 - Friction and Wear Tests of SCA-1002 Coatings, Thin Chromia Coatings, and Plasma Spray Zirconia Infiltrated with SCA-1002 or Thin Chromia	90%
1.3.1.5	GO/NO GO Decision Point on Components for Engine Evaluation, Selection of Components, and Procurement	---
1.3.1.6	Task 3 - Post Engine Test Coating Characterization	20%
1.3.1.7	Final Report	

Publications

A paper on "Evaluation of Chrome Oxide Coatings and Wear Resistant Plasma Spray Coatings" by T. M. Yonushonis and G. W. Wolter was presented during the 9th Annual Conference on Composition and Advanced Ceramic Materials, Cocoa Beach, FL, January 20-24, 1985.

1.4 JOINING

1.4.1 Ceramic-Metal Joints

Active-Metal Brazing of PSZ to Iron

J. P. Hammond and S. A. David (Oak Ridge National Laboratory)

Objective/scope

The purpose of this work is to develop brazing processes for joining ceramic insulation components to nodular cast iron (NCI) for adiabatic diesel engine applications. Foremost of these applications is the attachment of the ceramic piston cap. Presently, the lead candidate material for the ceramic piston cap is partially stabilized zirconia (PSZ), Nilsen grade MS, with dispersion toughened alumina (DTA) as an alternate. Promising brazing methods and the mechanical properties of prototypical brazements are evaluated so that reliable joining processes may be transferred to industry.

Technical progress

During the previous reporting period, progress was made in the following areas. A new macro shear testing apparatus that more accurately measures the shear strength of ceramic-metal joints was developed, and work was initiated to establish room- and elevated-temperature data on the braze joint interfaces of interest. Also, progress was made toward characterizing the structure and composition of the ceramic-to-filler-metal bond zone responsible for the good fabrication results obtained in the PSZ/NCI joints. The results in these areas are reviewed below.

The former shear testing apparatus was adapted from a push-off, sessile drop tester. Although the old tester had certain shortcomings that were overcome with the new design, results with the former unit were shown to qualitatively agree with data gathered with the new apparatus. The principal improvements made in the shear tests dealt with minimizing torsional and normal (to shear plane) stressing that may superimpose on the shear stress, and increasing the area of shear to minimize any strengthening effect that may arise from the braze fillet.

Importance is being placed on the shear test as the primary test for evaluating the effects of joint fabrication and design variables for the following reasons. First, failures in ceramic-metal joints most often are by the shearing mode. Moreover, shear strength is the mechanical property considered to be most important in the piston cap application. Further, the particular shear test specimen we are using requires no damaging machining operations, and the specimen is by far the most economical to produce of the various types of mechanical properties specimens that may be considered. The Maco (uniaxial) tensile test proposed earlier will require specimens very difficult and costly to produce, and the results of such tests on ceramic-metal joints generally have had poor consistency.[1]

The shearing component of the new test apparatus is illustrated in Fig. 1. It operates in a 44.5-kN Instron tensile machine, equipped with a clam-shell furnace and quartz line (for protective atmosphere) for optional testing at elevated temperature. The test specimens are shown in the lower right portion of the photograph. Part B fits concentrically into assembly A, while part C (shown in inverted position) bolts to part B to constrain the shearing action of the claw (marked by arrow in A) against the bar of the test specimen. The claw engages the bar adjacent to the braze interface just above the braze fillet. The pad is held secure in the specimen recess by a set screw in the back of part B that holds the specimen pad flush against the surface of part C. The surfaces of the bar (except for the braze interface) are free except along the line where the bar is engaged by the claw.

Y-201887

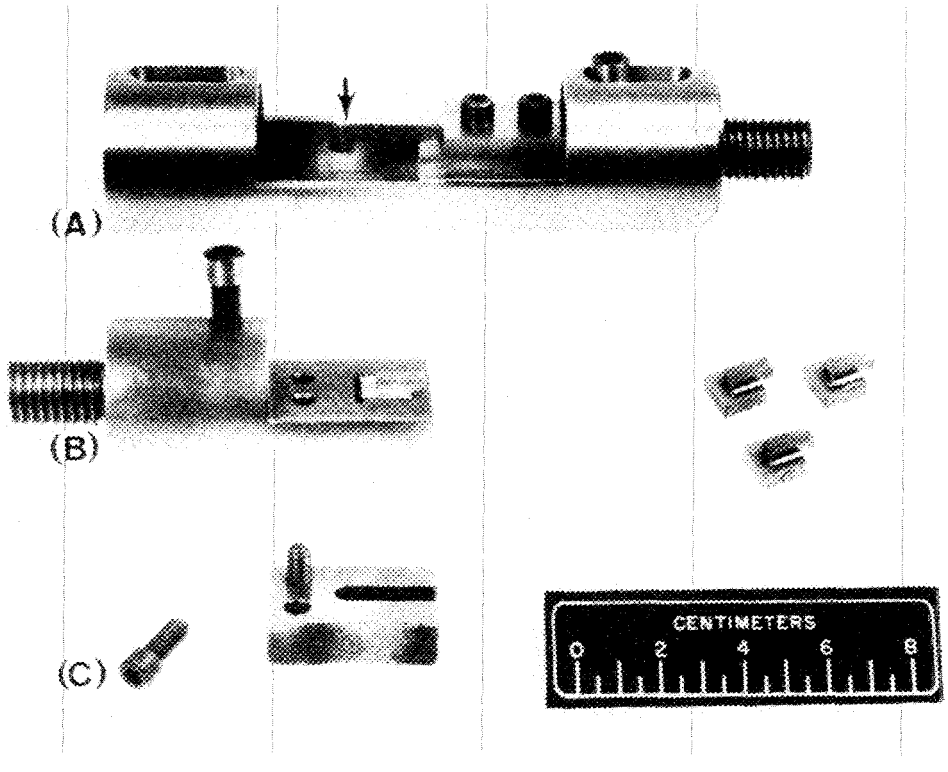

Fig. 1. Pad/bar shear tester (disassembled to show functional parts) uses specimens that are easy to fabricate and produces predominantly shear stress at braze interface.

The unit uses pad/bar specimens of 12.7 mm × 12.7 mm × 5.1 mm/12.7 mm × 5.1 mm × 3.4 mm size compared with 9.5 mm × 9.5 mm × 5 mm/9.5 mm × 3.4 mm × 3.4 mm for the former specimen. This results in a shear interface area of about 43 mm^2 compared with 21 mm^2 for the former specimen.

Room-temperature shear strength data developed for the PSZ/titanium/NCI and PSZ/NCI joints by using the new test apparatus are presented in Table 1. Joints of both types were fabricated by the active substrate (AS) and active filler metal (AFM) methods. The results for the former method of brazing will be presented first.

For the PSZ/titanium transition piece braze interface two ceramic materials, Nilsen grade MS (partially stabilized with Mg) and Coors TZP (partially stabilized with Y), were tested. The former was fabricated both at 735 and 800°C.

The latter ceramic has a predominantly tetragonal crystal lattice, whereas grade MS is predominantly cubic with largely the tetragonal phase constituting the remainder. Grade 8003 iron [552 MPa (80 ksi) yield strength] was used for the nodular cast iron. A titanium sput of 0.5 μm thickness was employed on the ceramic pieces, while 0.05 mm of copper was

Table 1. Shear strength data[a] on joint interfaces prepared by active substrate (AS) and active filler metal (AFM) brazing[b]

Specimen	Brazing temperature (°C)	Room temperature shear strength[c] (MPa)	(ksi)
PSZ/Ti/NCI joint by AS brazing			
PSZ(MS)/Ti	735	140.1 ± 18.1	20.34 ± 2.73
PSZ(MS)/Ti	800	41.7 ± 5.9	6.05 ± 0.86
TZP/Ti	735	161.8 ± 11.4	23.46 ± 1.66
NCI/Ti	735	253.0 ± 23.4	36.70 ± 3.39
PSZ/NCI joint by AS brazing			
PSZ(MS)/NCI	735	136.5 ± 7.6	19.80 ± 1.11
PSZ/Ti/NCI and PSZ/NCI joints by AFM brazing			
PSZ/(MS)/Ti	980	121.7 ± 8.3	17.65 ± 1.20
PSZ(MS)/NCI	980	78.0 ± 18.4	11.32 ± 2.67

[a]Tests performed with new shearing apparatus with a shear interface area of 43 mm^2.

[b]Brazed 10 min in vacuum of 6.6 mPa.

[c]Values are a mean of four tests, with the tolerance values being the standard deviation.

electroplated on the NCI. The usual 60 Cr-30 Ag-10 Sn (wt %) alloy as 0.07-mm foil was used for filler metal. The shear strength values are the mean of a total of four tests, whereas the tolerance values are the standard deviation.

Observe that the standard errors for these data range from 0.86 to 3.39, which attests to the excellent precision of the test method. It should be further noted that the test trends of the brazements prepared by the AS method parallel those of the earlier results with the smaller specimen.[2] Indeed, the individual values come remarkably close to the earlier ones considering that the earlier values were an average of only two tests.

Concerning the PSZ/titanium/NCI joints, the NCI/titanium braze interface is substantially stronger than the PSZ/titanium interface as experienced earlier.[2] The strength of the braze interface of the directly joined PSZ/NCI joint is about equivalent to that of the PSZ/titanium interface of the indirectly brazed joint (compare test values for specimens brazed at 735°C). Significantly, the TZP/titanium joint prepared from the Coors ceramic stabilized with yttrium and containing predominantly the tetragonal crystal phase is about 20 MPa stronger than this joint when prepared from the grade MS ceramic that is stabilized with magnesium and contains predominantly the cubic phase. As in earlier tests, the PSZ(MS)/titanium joint brazed at 800°C is much weaker than the same joint brazed at 735°C. Finally, it should be emphasized that the shear strength values achieved for all of the braze interfaces formed by AS brazing at 735°C are in excess of expected design requirements for the piston cap application.

Typical shear test specimens of the PSZ(MS)/titanium, NCI/titanium, and PSZ(MS)/NCI braze interfaces joined at 735°C are shown in Fig. 2. The favorable brazing characteristics of joints processed by the active substrate method will be apparent from the wetting and excellent filleting between bars and pads.

Close examination of the bars in Fig. 2 reveals a 6-mm radius on their front end where they engage the claw (Fig. 1). The purpose of this radius is to ensure that the principal shearing force is applied through the center of the shear area to avoid any possible secondary torsional forces which may arise from the claw engaging a misaligned bar of flat nose.

The fabrication results on braze interfaces associated with the PSZ/titanium/NCI indirect and PSZ/NCI direct joints fabricated by active filler metal brazing (Table 1) are rather sparse, but they nevertheless show encouraging strength for the more critical interface of the indirect joint. A shear strength value of 121.7 ± 8.3 MPa (17.65 ± 1.20 ksi) is recorded for the PSZ(MS)/titanium interface compared with a value of 140.1 ± 18.1 MPa (20.34 ± 2.73 ksi) for this brazement fabricated by the active substrate method. On the other hand, the direct PSZ(MS)/NCI joint fabricated by active filler metal brazing shows a shear strength of only 78.0 ± 18.4 MPa (11.32 ± 2.67 ksi).

The latter braze interfaces were fabricated by heating 10 min in vacuum [6.6 mPa (5×10^{-5} torr)] at 980°C using a 54 Ag-36 Cu-10 Ti (wt %) active alloy ribbon for the filler metal. The NCI was electroplated with 0.05 mm of copper.

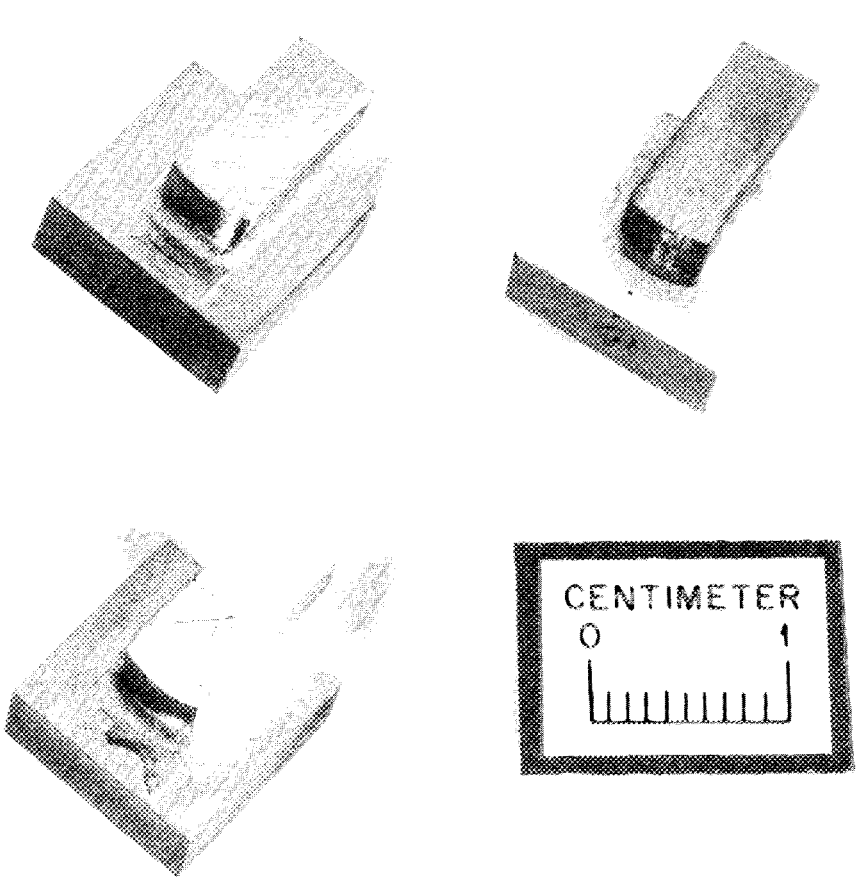

Fig. 2. Enlarged view of shear test specimens [PSZ(MS)/titanium and NCI/titanium at top; PSZ(MS)/NCI at bottom] shows the excellent brazing characteristics of joints fabricated by active substrate brazing. Brazed 10 min at 735°C in vacuum [6.6 mPa (5×10^{-5} torr) using 60 Ag-30 Cu-10 Sn (wt. %) filler metal, 1/2 μm Ti sput, and 0.05 mm copper electroplating (for NCI).

Photomacrographs of the active filler metal brazed pad/bar shear specimens, which illustrate the quality of the braze joints, are shown in Fig. 3. The PSZ/titanium joint exhibits wetting and excellent filleting, whereas in the PSZ/NCI joint the wetting and filleting are rather poor. This correlates quite well with the shear strength results. In the PSZ/titanium joint, the substrate discoloration is very intense (a dark black), which appears to have been caused by the titanium bar dissolving in the liquid filler metal as the brazing proceeds. In spite of the severe blackening of the substrate, the ceramic held together quite well during testing, with the fracturing occurring completely at the ceramic-metal interface. That the brazement performed so well probably is attributable in part to a good coefficient of expansion matchup at the interface. The merits of titanium for the transition piece (TP) were previously documented.[2] Active filler metal brazing with the titanium transition piece as a two-stage fabrication process will be investigated further in the future.

CYN-6019

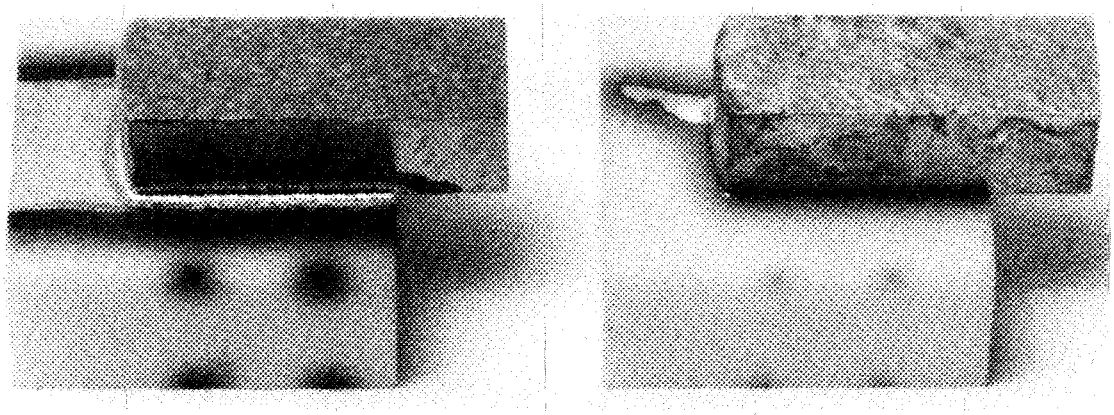

Fig. 3. Shear test specimen [PSZ(MS)/titanium at left, PSZ(MS)NCI at right] fabricated by active filler metal brazing. Brazed 10 min at 980°C in vacuum [6.6 mPa (5×10^{-5} torr)] using 54 Ag-36 Cu-10 Ti (wt. %) filler metal and 0.05 mm copper electroplating (for NCI).

The examination conducted on the bond zone formed between PSZ and filler metal with 750°C active substrate brazing using electron-probe microanalysis and X-ray diffraction as tools of investigation revealed a number of significant features. A photomicrograph of the filler metal deposit and the adjoining structural materials is shown in Fig. 4. The thickness of the bond zone (between ceramic and filler metal) in relation to that of the filler metal deposit, which consists of a eutectiferrous solid solution phase of predominantly copper in a continuous ductile matrix of solid solution silver, is apparent.

An insight into the composition of the bond zone and adjoining filler metal was gained by dot mapping the elemental constituents Zr, Ag, Ti, Cu, and Sn, as shown in Fig. 5. From this and from rate meter line profiles of these elements as viewed in backscatter electron (BSE) micrographs of the zone (Fig. 6), the following information was gained. The original sput coating (black layer in BSE images) and the eutectiferrous copper and silver solid solution phases are readily recognized in both Figs. 5 and 6.

The dot maps (Fig. 5) show that in addition to the copper and continuous silver phases having some mutual solubility for one another (the Ag-Cu constitution diagram indicates a solubility of about 12 at. % Cu and 2 at. % Ag, respectively, at the brazing temperature[3]), considerable Sn is dissolved in both phases, especially in the copper. Additionally, the Sn tends to segregate just off the titanium sput along with the copper constituent.

The line profiles taken across the bond zone confirm the presence of Ti, Cu, and Sn in the layer adjacent to the original sput.* Thus a ternary intermetallic compound containing these three constituents is indicated.

*The heights of the respective profile peaks in Fig. 5 have no significance because different rate settings were used for the individual profiles.

Y-198882

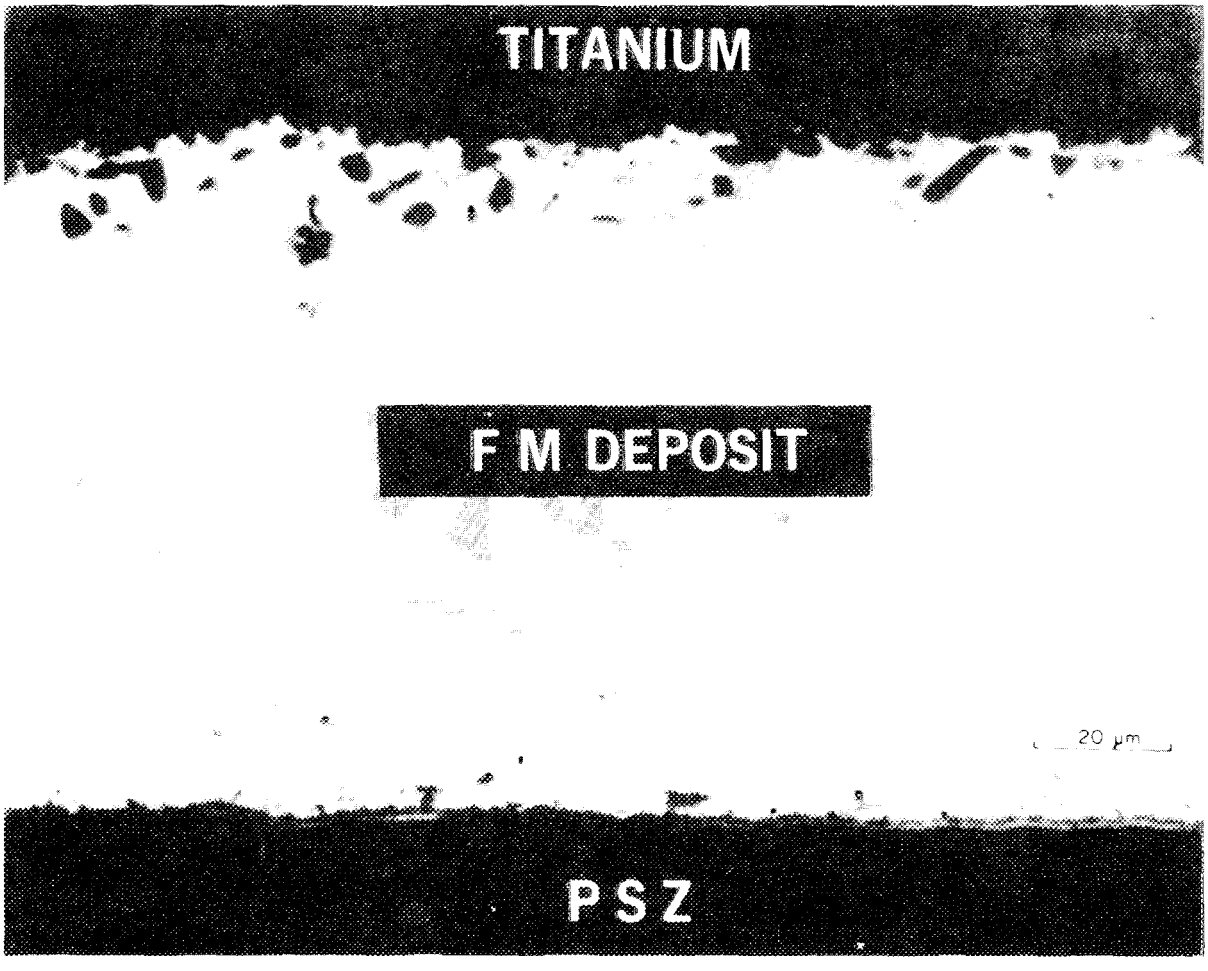

Fig. 4. Microstructure of the braze joint between titanium transition piece and PSZ(MS) ceramic, using the 60 Ag-30 Cu-10 Sn (wt. %) alloy as filler metal. Brazed in vacuum [6.6 mPa (5×10^{-5} torr)]. As polished.

The nature of the layer between this intermetallic compound and the PSZ substrate was explored by performing X-ray diffraction analyses on titanium sputter coated (0.5, 1.0, and 2.0 μm thicknesses) ceramic specimens that had been subjected to the simulated braze cycles (10 min and 3 h at 750°C) without the presence of the filler metal. These tests showed the presence of the cubic zirconia phase (the substrate), cubic TiO phase, and possibly hexagonal titanium metal phase (the latter depending on the sput coating thickness and brazing period). The ceramic substrate adjoining the sput coating was darkened in the usual manner. Because the braze cycle

ORNL-PHOTO 7884-84

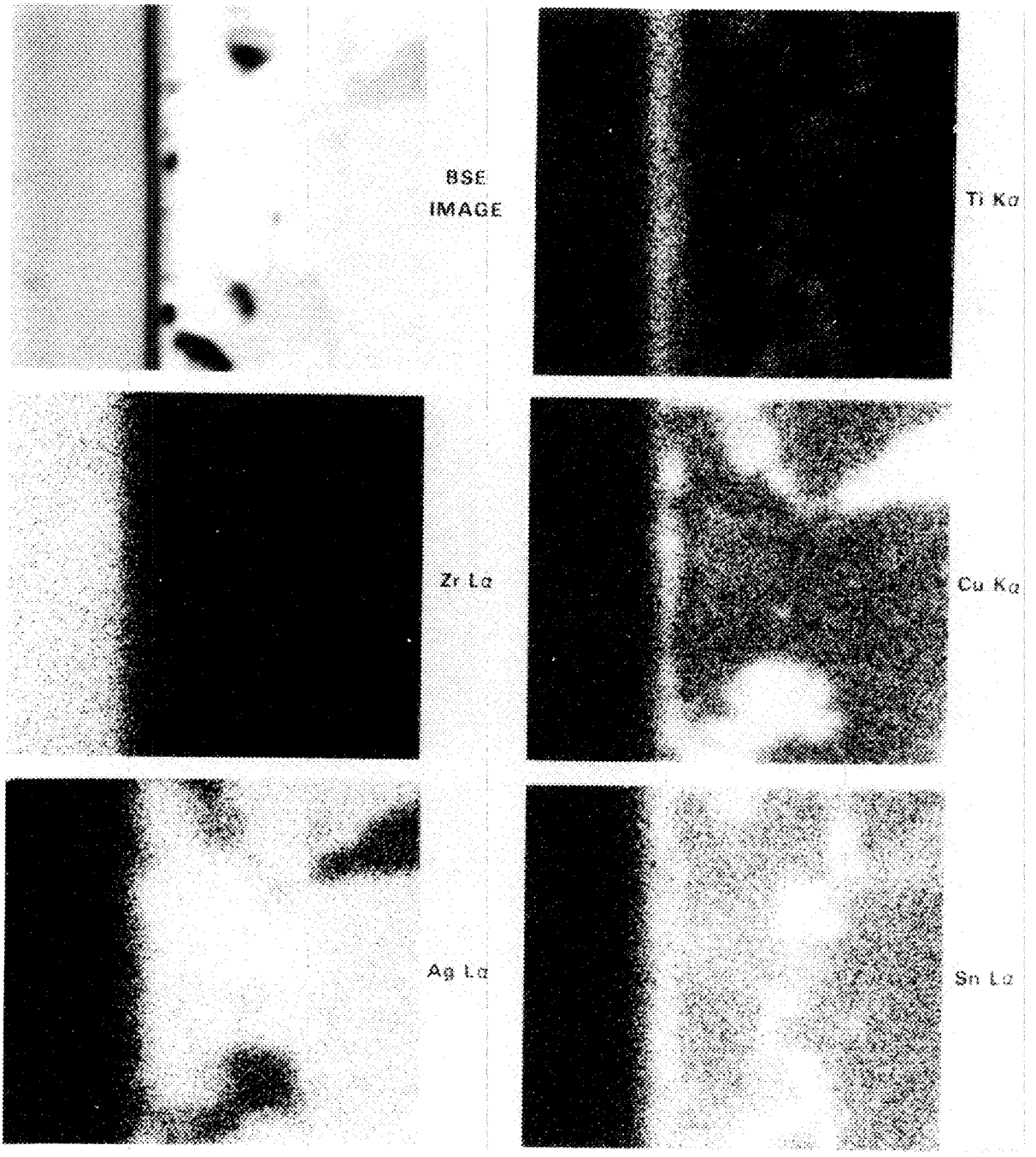

Fig. 5. Electron-probe dot maps of the elemental constituents in the PSZ(MS)/FM bond zone. Active substrate brazed 10 min at 750°C in 6.6 mPa (5×10^{-5} torr) vacuum using 1 μm titanium sput on the ceramic and 60 Ag-30 Cu-10 Sn alloy as filler metal.

ORNL-PHOTO 7856-84

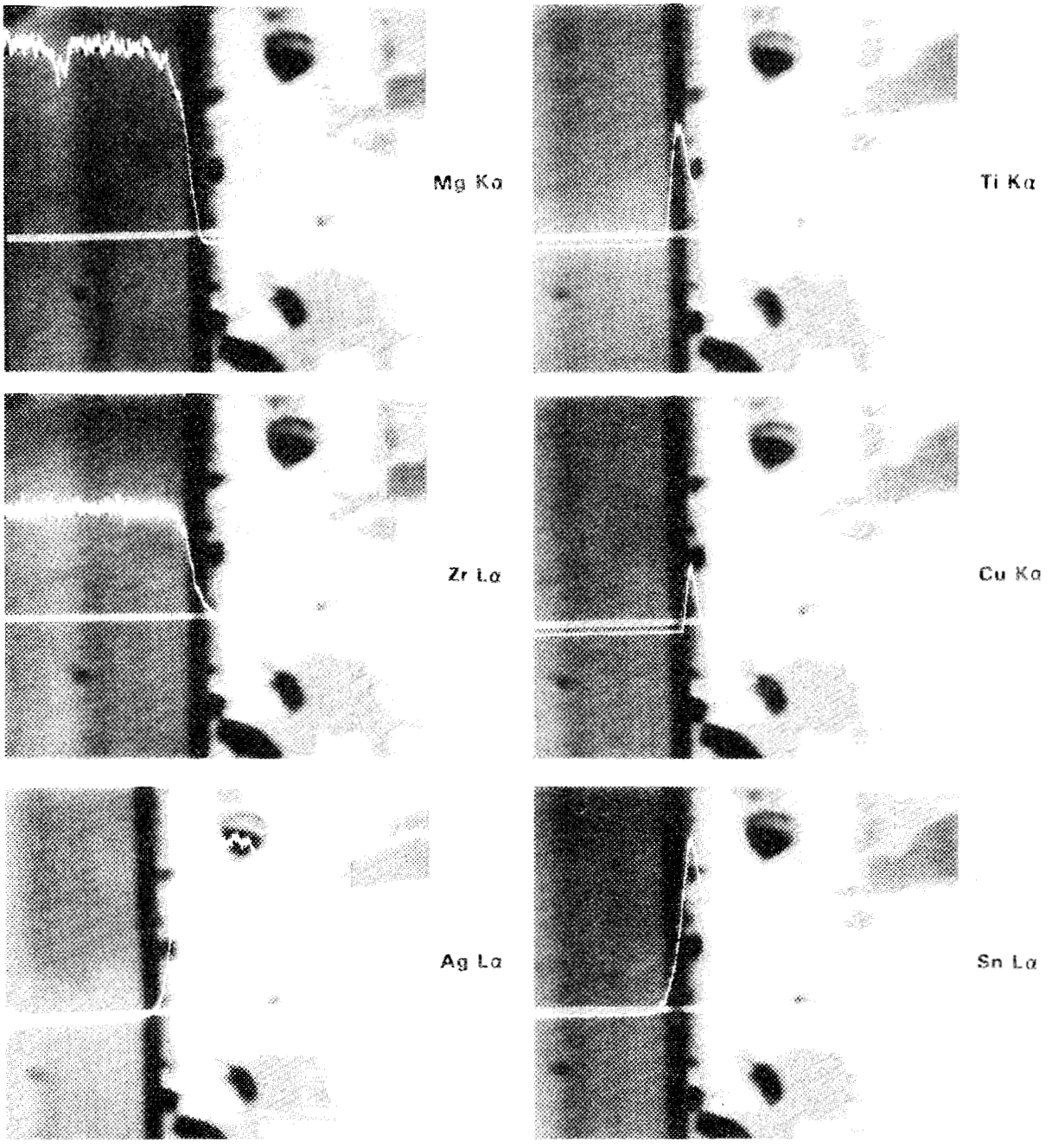

Fig. 6. Electron probe rate meter line profiles of the elemental constituents in the PSZ(MS)FM bond zone. Brazed 10 min at 750°C in 6.6 mPa (5×10^{-5} torr) vacuum.

was performed in vacuum, the TiO phase clearly is formed by a reaction of the sput with the substrate, ostensibly from oxygen diffusing outwardly and thus creating the observed oxygen-improverished, darkened region.

It was concluded from these experiments that the bond zone responsible for the good fabrication results in the PSZ(MS)/NCI joint employing the 60 Ag-30 Cu-10 Sn alloy as filler metal consists of sequential layers of PSZ, darkened zirconia, TiO, possibly titanium metal, the $Ti_xCu_ySn_z$ intermetallic compound, and filler metal deposit. A requirement for successful brazing appears to be the formation of the intermetallic phase. When the sput coating is too thin in relation to the intensity of the braze cycle (e.g., 0.1 μm relative to 10 min at 750°C), the sput transforms completely to TiO and $Ti_xCu_ySn_z$ does not form. As a result, wetting, which is essential to bonding, fails to occur.

Status of milestones

Milestone 2, scheduled for completion in September 1985, is progressing on schedule. A high-precision macro shear testing apparatus with a 43-mm^2 shear area was perfected, and room-temperature shear strength data were developed for PSZ/titanium/NCI and PSZ/NCI joints fabricated by both the active substrate (one-stage) and the active filler metal (two-stage) processes. Additional shear tests at room temperature are needed, while elevated-temperature shear tests and the assessment of environmental effects are yet to be initiated. Our present shear test, which will constitute the main mechanical properties test method during the first-phase work, has produced very consistent data. For PSZ/NCI joints fabricated by active substrate brazing, mean value shear strengths (sets of four tests) of joint interfaces have exceeded 138 MPa (20 ksi), which is amply in excess of expected design requirements for the piston cap application. Standard errors have ranged from 7.6 to 23.4 MPa (1.11 to 3.39 ksi), attesting to the excellent precision of the test method.

Also noteworthy is the achievement of a shear strength of 161.8 ± 11.4 MPa [23.46 ± 1.66 (SE) ksi] for the TZP/titanium interface joined by active substrate brazing. This is 20.7 MPa (3 ksi units) higher than for the same interface when grade MS PSZ is used for the ceramic. The TZP ceramic is Coors tetragonal zirconia partially stabilized with yttrium. Additionally, good shear strength results [121.7 ± 8.3 MPa (17.65 ± 1.20 ksi)] were obtained for the PSZ(MS)/titanium interface brazed with 54 Ag-36 Cu10 Ti (wt. %) ribbon by the active filler metal process (joined at 980°C and intended for two-stage fabrication).

References

1. H. Mizuhara, "Active Brazing Alloy," No. 4 JV-84, presented at the 86th Annual Meeting of the American Ceramic Society, Pittsburgh, Pa., May 2, 1984.

2. J. P. Hammond and S. A. David, "Ceramic to Metal Joining," pp. 60–70 in *Ceramic Technology for Advanced Heat Engines Project Semi-annual Progress Report for Period April 1984–September 1984*, ORNL/TM-9497, February 1985.

3. Max Hansen, *Constitution of Binary Alloys*, pp. 18–20, McGraw-Hill Book Company, New York, December 1985.

2.0 MATERIALS DESIGN METHODOLOGY

INTRODUCTION

This portion of the project is identified as project element 2 within the work breakdown structure (WBS). It contains three subelements: (1) Three-Dimensional Modeling, (2) Contact Interfaces, and (3) New Concepts. The subelements include macromodeling and micromodeling of ceramic microstructures, properties of static and dynamic interfaces between ceramics and between ceramics and alloys, and advanced statistical and design approaches for describing mechanical behavior and for employing ceramics in structural design.

The major objectives of research in Materials Design Methodology elements include determining analytical techniques for predicting structural ceramic mechanical behavior from mechanical properties and microstructure, tribological behavior at high temperatures, and improved methods for describing the fracture statistics of structural ceramics. Success in meeting these objectives will provide U.S. companies with methods for optimizing mechanical properties through microstructural control, for predicting and controlling interfacial bonding and minimizing interfacial friction, and for developing a properly descriptive statistical data base for their structural ceramics.

2.2 CONTACT INTERFACES

2.2.1 Static Interfaces

High Temperature Coating Study to Reduce Contact Stress Damage of Ceramics

J. L. Schienle (Garrett Turbine Engine Company)

Objectives/scope

The objective of this research program* is to develop coating compositions and procedures that will yield long term adherence and reduce or eliminate contact-stress damage to silicon nitride (Si_3N_4) and silicon carbide (SiC) ceramics. Prior studies[1-3] have determined that Si_3N_4 and SiC ceramics are susceptible to contact stress damage at ceramic-ceramic and ceramic-metal interfaces in heat engines. Subsequent studies have demonstrated a reduction or elimination of contact-stress damage to these ceramics using plasma-sprayed oxide coatings, but the coating adherence was not adequate for long term use.

This program utilizes an alternate coating method, electron beam physical vapor deposition (EB-PVD), as the coating process because of high control of composition, thickness, and morphology. Three substrate materials were selected for investigation: reaction-bonded silicon nitride (RBSN), sintered silicon nitride (SSN), and sintered silicon carbide (SSC)**. The RBSN and SSC were selected because substantial baseline strength and contact data were available. The SSN was selected to provide a nonporous Si_3N_4 to compare with the porous RBSN.

The present program scope consists of four technical tasks to be conducted over 31 months:

- Task 1 - Coating Adherence and Characteristics Investigation
- Task 2 - Advanced Pretreatment and Coating Studies***
- Task 3 - Contact Stress Testing and Friction Measurements
- Task 4 - Post-Contact Strength Measurement

Technical progress

During this reporting period, Task 1 was completed and Task 2 was initiated. The emphasis of Task 1 was to deposit a controlled zirconium oxide coating on Si_3N_4 and SiC substrates having various surface pretreatments, evaluate coating adherence characteristics, and determine the mechanisms of coating adherence. Task 1 efforts did not yield a coating/substrate system with adherence characteristics satisfactory for heat engine applications. However, directions for improved coating adherence investigation were identified. Based on the results of Task 1, the program

*Research sponsored by the U.S. Department of Energy under DOE/CE EE 0400 00 0, Ceramic Technology for Advanced Heat Engine Program WBS SC-I-2.2.1.

**RBSN and SSN from the AiResearch Casting Company, Torrance, California, and SSC from the Carborundum Company, Niagara Falls, New York.

***Task 2 was "Strength of Baseline and Coated Specimens" prior to the program revision approved by Supplemental Agreement 2.

was restructured to continue screening evaluations of substrate pretreatment and coating evaluations in Task 2. The statistical strength testing originally planned for Task 2 was postponed until Task 3 so that optimized coating/substrate systems could be developed. Advanced pretreatment and coating evaluations under Task 2 are progressing. Technical progress made under Tasks 1 and 2 during the reporting period are discussed in the following paragraphs.

Task 1 - Coating adherence and characteristics investigation

Task 1 efforts during this reporting period included preliminary line contact tests and microstructure/chemical analysis. The preliminary line contact tests were conducted in the GTEC contact rig to demonstrate the feasibility of line contact tests for adherence assessment and develop test procedures for future adherence assessment analyses. Microstructural/chemical analysis was conducted at University of California, Berkeley (UCB), to determine the mechanisms of coating adherence degradation observed after static air oxidation exposures.

Preliminary line contact tests. Preliminary line contact tests were conducted at GTEC to determine the feasibility of using the GTEC contact rig to assess coating adherence. Originally, the contact rig was only planned for use in Task 3 of the program in determining the coefficients of friction and the resistance to contact damage (strength retained after contact testing) for optimized coating/substrate systems. However, the indentation tests used earlier in Task 1 for adherence evaluations were too severe for oxidized specimens having reduced adherence. When the debonding, which is the measurable result of the indentation test, extends to the edges of the specimen (Figure 1), it does not provide comparative information. The contact rig is attractive for adherence assessment tests because line contact testing better simulates the type of stresses expected in a heat engine. Indentation testing exaggerates the contact stress conditions and might lead to elimination of a coating/substrate system, which may be acceptable.

Line contact testing was conducted with the GTEC test apparatus illustrated in Figure 2. With this apparatus, a normal force is applied to the specimen through a dead weight load system while a tangential force is applied through displacement of the crosshead. This mode of loading was identified in prior studies to be a critical condition to evaluate in terms of contact stress damage[1-3]. However, the purpose of the preliminary testing under the present program was only to demonstrate the feasibility of using this type of loading for coating adherence assessment tests.

Two types of line contact tests were conducted:

- o Static bi-axial load; i.e., a normal load (perpendicular to the surface) plus a tangential load sufficient to cause a bi-axial surface stress distribution, but insufficient to cause sliding.
- o Sliding bi-axial load; i.e., a normal load plus a sufficient tangential load to cause sliding.

Exploratory studies began using static bi-axial loading on specimens subjected to post-coating oxidation exposures to determine the threshold

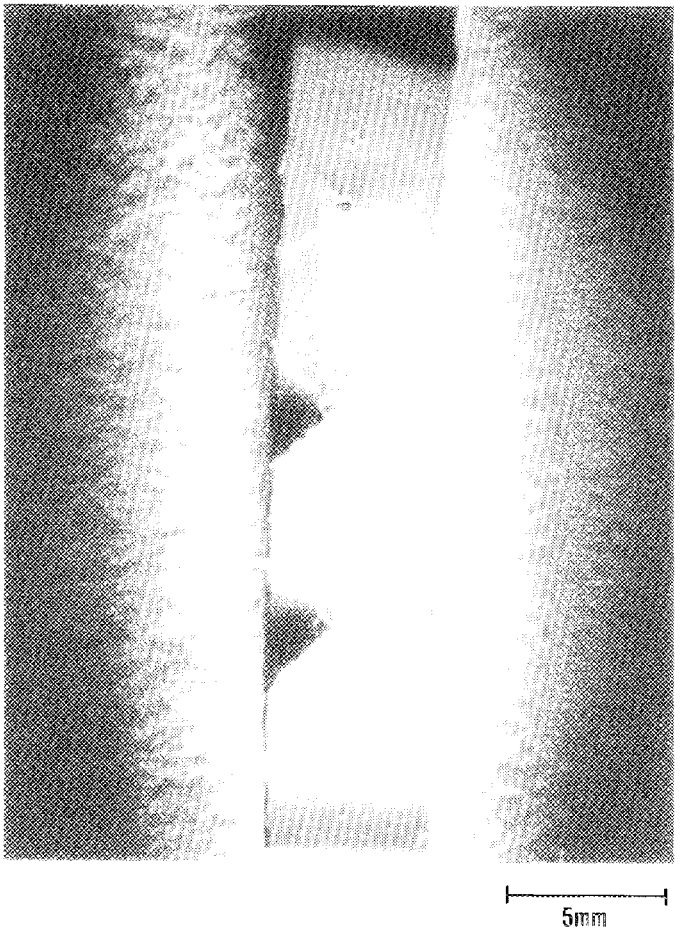

Figure 1. Debonding extended to the edges of the coating making the indentation test inclusive.

bi-axial stress conditions for visible damage to the coatings. The oxidized specimens have reduced coating adherence relative to as-coated specimens (determined by indentation testing) and therefore, were chosen to find the minimum loads necessary to initiate damage.

During initial testing, the average threshold appeared to be about 222.4 Newtons (50 pounds) normal load with 44.5 Newtons (10 pounds) tangential load. Based on the above observation, the test conditions for the remaining oxidized specimens were selected and are shown in Table 1.

In subsequent tests, the coatings neither chipped nor spalled regardless of material substrate or pretreatment. In some cases debonding was evident but only in the line of contact and not outside the contact region. Some specimens exhibited no debonding. The results suggest that static bi-axial load testing is advantageous to indentation in that specimens having poor coating adherence can be evaluated. However, the degree of damage to the system resulting from the test cannot be quantitatively measured as it can for the indentation technique. The results of the static mode tests also suggest that the adherence of oxidized specimens may be more acceptable than indentation tests indicated.

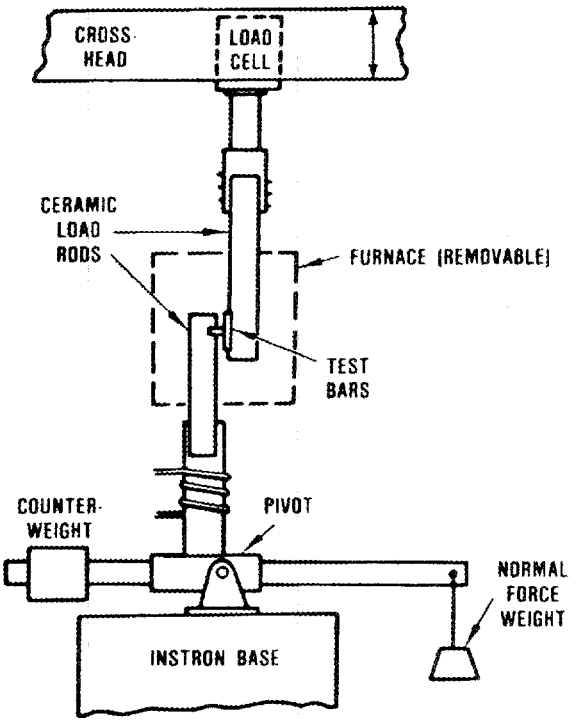

Figure 2. Contact stress test apparatus.

Table 1. Load conditions for static mode tests on oxidized specimens.

Normal Load, Newtons (pounds)	Tangential Load, Newtons (pounds)
133.4 (30)	26.7 (6)
177.9 (40)	35.6 (8)
222.4 (50)	44.5 (10)
266.9 (60)	53.4 (12)

In addition to static mode tests, sliding contact tests also were conducted. Reserve as-coated specimens were utilized to demonstrate the feasibility of using this type of loading for adherence assessment.

As a starting point, a normal load of 44.5 Newtons (10 pounds) was selected for the sliding contact tests; the total sliding motion was 1.52 mm. No damage was done to any of the specimens tested under these conditions. The normal load was increased at 22.2-Newton (5-pound) intervals to 111.2 Newtons (25 pounds). At this load, visible damage to the coatings occurred on approximately one-half of the specimens. Based on these results, 111.2 Newtons (25 pounds) was selected as the normal load for subsequent sliding contact tests on remaining specimens. At this normal load, the maximum tangential load just prior to sliding is approximately 48.9 Newtons (11 pounds) and the tangential load during sliding is 31.1 Newtons (7 pounds). Static mode test conditions were also selected for the as-coated specimens. The contact testing conditions are summarized in Table 2.

Table 2. Test conditions for as-coated specimens.

Static Mode:	266.9 Newtons (60 pounds) normal load 53.4 Newtons (12 pounds) tangential load
Sliding Mode:	111.2 Newtons (25 pounds) normal load 1.52 mm total sliding motion

Five as-coated specimens were tested under the conditions in Table 2. Test results are tabulated below:

Specimen	Static Mode	Sliding Mode
SSC (machined) light oxidation pretreatment (Figure 3)	Debond Line	Chipped
SSN (lapped) no pretreatment (Figure 4)	Debond Line	Debonded Area
RBSN (lapped) light oxidation pretreatment (Figure 5)	Debond Line	No Damage
RBSN (lapped) light oxidation pretreatment	Debond Line	No Damage
SSC (machined) no pretreatment	Debond Line	No Damage

No chipping or spalling occurred for the static tests of the as-coated specimens. However, all tests resulted in a debond line at the line of contact - note that only the most severe of the test conditions used for the oxidized specimens, 266.9 Newtons (60 pounds) normal load, 53.4 Newtons (12 pounds) tangential, was used in testing the as-coated specimens. For sliding tests, varying results were observed; some specimens exhibited chipping or debonding while others showed no visible damage.

Based on preliminary results, both the static and dynamic contact test appear useful as durability or proof tests for the coatings. The conclusion is that contact tests, along with indentation tests, should be more appropriate for assessing coating adherence than indentation testing alone.

Microstructural/chemical analysis. Microstructural/chemical analyses were conducted at UCB to determine the mechanism of coating adherence degradation during static air oxidation exposures. Earlier Task 1 adherence evaluations showed excellent coating adherence to SiC and Si_3N_4 substrate surfaces but less than adequate adherence after oxidation

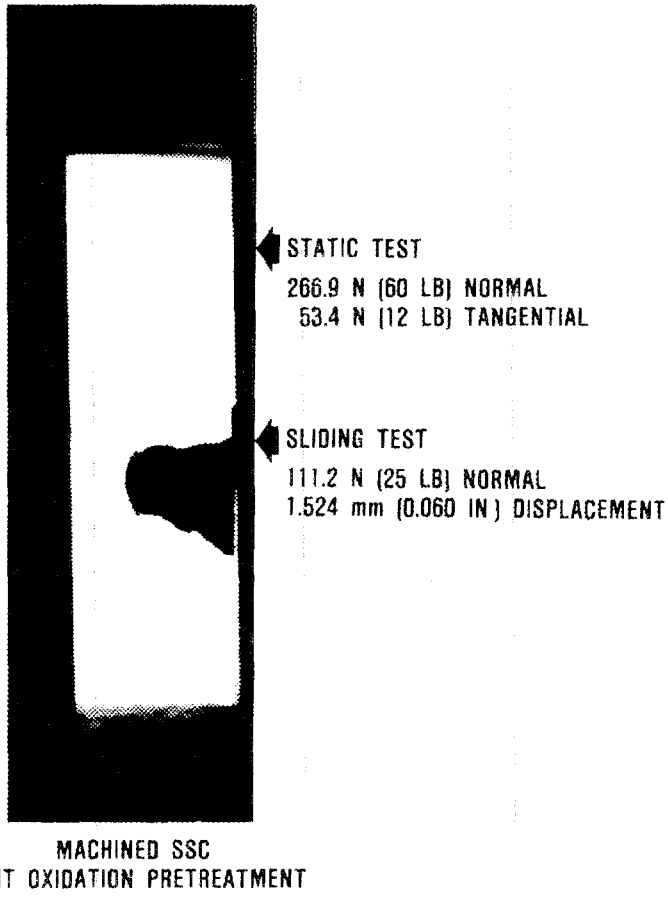

Figure 3. Debonding at line contact for static test; coating chipped during sliding contact test.

exposures. The ZrO_2 coatings used are permeable to oxygen so some type of interaction at the coating/substrate interface was expected. Polished sections of as-coated and oxidized specimens were prepared to allow coating/substrate interfaces to be examined using a scanning transmission electron microscope (STEM). The STEM was used as a high resolution SEM (STEM has higher resolution than conventional SEM due to smaller electron beam radius). Initial observations at UCB revealed the presence of a silicate layer at coating/substrate interfaces. For as-coated specimens, STEM did not reveal silicate layers topographically on micrographs, but silicate layers at coating/substrate interfaces were identified chemically. The silicate layers in as-coated specimens are probably a result of the presence of oxygen in the coating chamber during ZrO_2 deposition. The stoichiometry of the ZrO_2 is controlled through the partial pressure of oxygen during coating. Because the coating temperature is 980C, subsequent substrate oxidation may occur. For specimens with post-coating heat treatments, silicate layers were topographically and chemically recognizable. Figures 6 and 7 illustrate the coating/substrate interfaces for two systems as seen using STEM. Figure 6 shows the interface on both as-coated and oxidized (post-coating) RBSN. A silicate layer is not visible for the as-coated RBSN (although chemical analysis revealed its

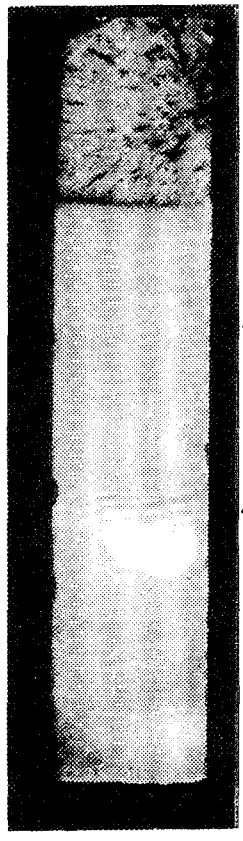

Figure 4. Debonding at line contact for static test; coating debonded in front of contact line during sliding test.

presence), while for the oxidized specimen the silicate layer appears to be one micron in thickness. The same features were observed for SSN (Figure 7), i.e., no visible silicate layer for the as-coated SSN, and a visible silicate layer approximately two microns thick for the oxidized specimen.

The hypothesis of these preliminary studies is that the growth of the silicate layer is directly responsible for reduced coating adherence after post-coating static oxidation. Although submicron silicate layers are present in as-coated specimens, the adherence is relatively good. Only after growth of the silicate layer during subsequent heat treating is adherence severely degraded. Also, there is some indication that impurities in the silicate layer from the substrate and/or coating may have an effect on the post-coating oxidation kinetics, thus affecting coating adherence. A more detailed analysis is being conducted under Task 2.

Task 2 - Advanced pretreatment and coating studies

As mentioned previously, the program was restructured to delay statistical strength testing until Task 3 in order to continue screening evaluations in Task 2. The rational for the changes included the following:

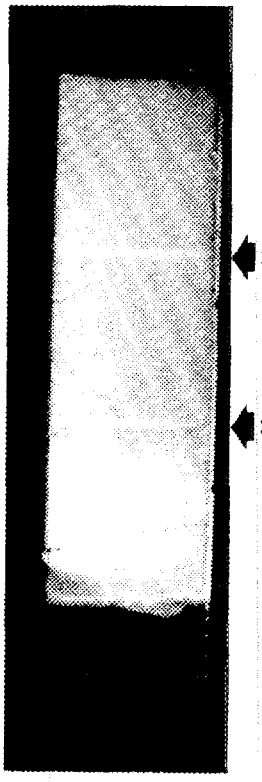

Figure 5. Debonding at line contact for static test; no critical damage resulting from sliding contact; only abrasion of coating evident.

- o Coating adherence after oxidation for the pretreatments and coatings studied in Task 1 was determined to be less than desired.
- o The Task 1 studies identified further directions for pretreatment and coating modifications that could yield increased understanding of the adherence mechanisms and lead to improved adherence after oxidation exposure.
- o Limited strength testing during Task 1 indicated that the surface pretreatments and coating procedures caused no significant strength reduction of SiC and Si_3N_4 substrate materials.

Several new coating/substrate system approaches are being evaluated during Task 2. These studies are separated into the following seven subtasks:

1. Oxidation
2. Oxygen Diffusion Barrier
3. High Purity Interlayer
4. Diffusion/Gradation Zone
5. Coating Variation
6. Surface Preparation
7. Mullite Coating

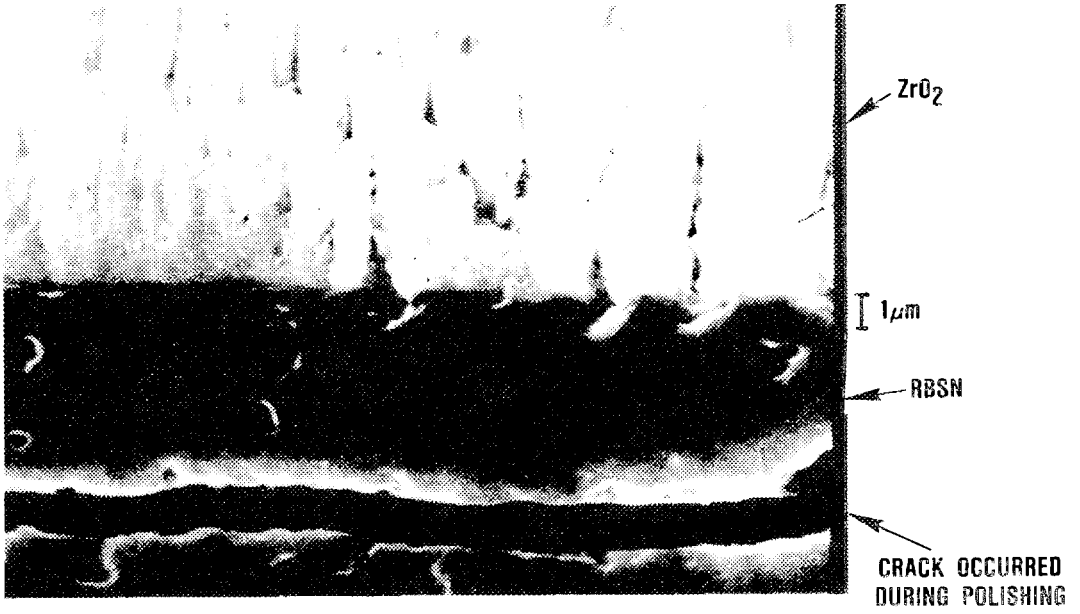

AS-COATED RBSN
SILICATE LAYER NOT VISIBLE

POST-COATING OXIDIZED RBSN
SILICATE LAYER VISIBLE

Figure 6. STEM micrographs of zirconia/RBSN interfaces.

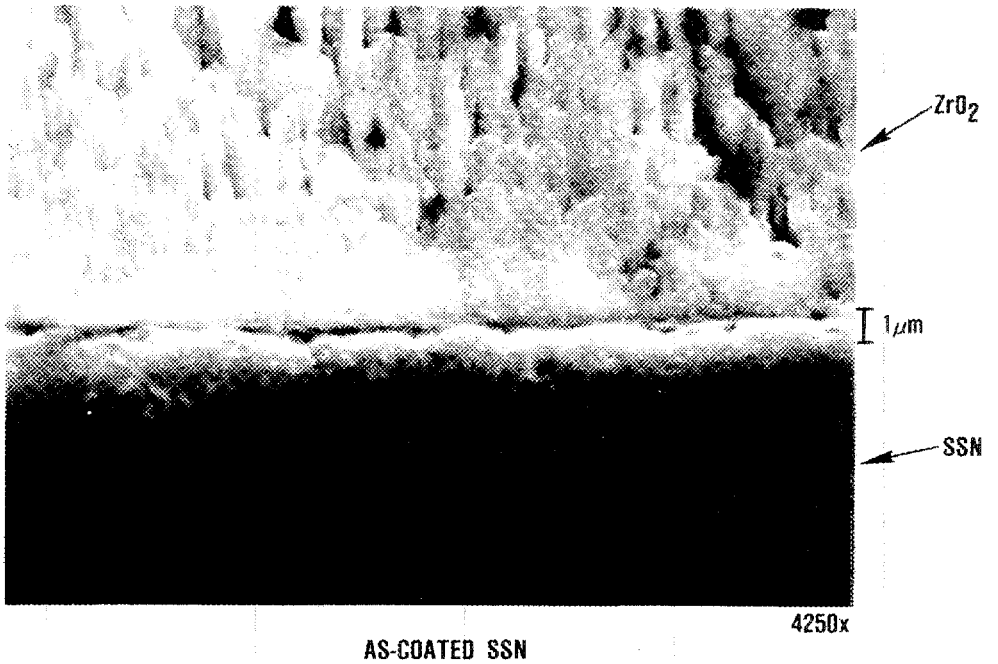

AS-COATED SSN
SILICATE LAYER NOT VISIBLE

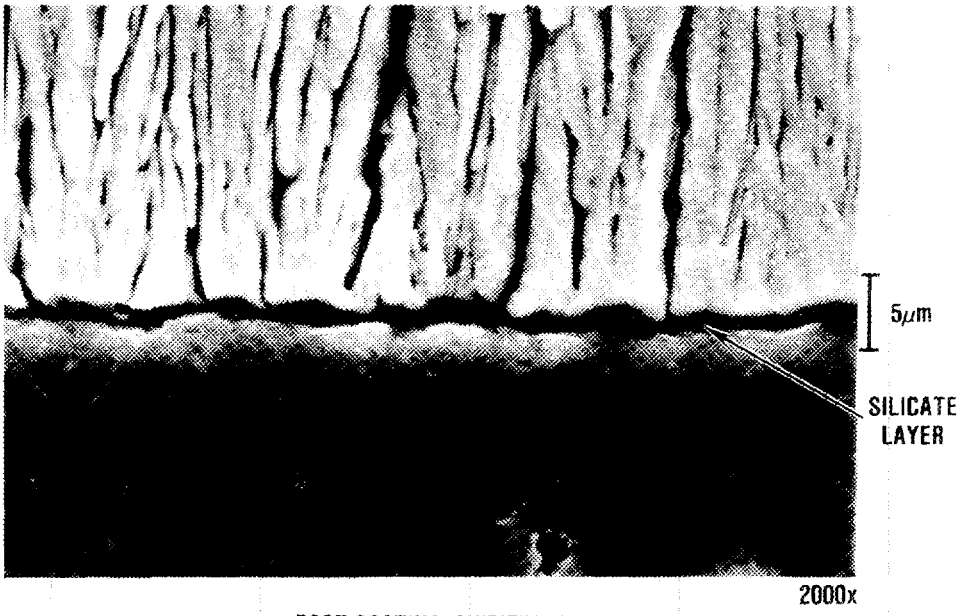

POST-COATING OXIDIZED SSN
SILICATE LAYER VISIBLE

Figure 7. STEM micrographs of zirconia/SSN interfaces.

Each of the subtasks and the progress made within are briefly described below:

Subtask 1: Oxidation. Task 1 results determined that adherence degradation after static oxidation was due to the growth of a silicate layer at the coating substrate interface. For this subtask, detailed microstructural/chemical analysis will be conducted on ZrO_2 coated RBSN, SSN, and SSC subjected to various static air heat treatments.

As-machined substrates were EB-PVD coated with ZrO_2-20%Y_2O_3 at Temescal. The specimens then were subjected to various oxidation heat treatments and flexure tested in four-point bending at GTEC. Based on visual examination of the coating/substrate systems after flexure testing, longer duration oxidation heat treatments (200 hours versus 100 hours at 1200C) did not result in a significant additional decrease in coating adherence, although adherence was degraded from the as-coated condition. However, higher temperatures (1400 versus 1200C for 200-hour durations) resulted in decreased adherence for the RBSN and SSN substrates but not for the SSC substrates. Selected specimens will be sent to Dr. A. Evans at UCB for detailed chemical analysis of the oxide layers at the coating/substrate interface. Also, the fracture surfaces of some specimens will be studied using SEM at GTEC.

Subtask 2: Oxygen Diffusion Barrier. Because coating adherence degradation after static oxidation is believed to be due to the growth of an oxide layer, an oxygen diffusion barrier at the coating/substrate interface may reduce or eliminate the observed adherence degradation. The candidates for evaluation are Al_2O_3, AlN, and mullite.

Alumina interlayers were applied to the three substrate materials by chemical vapor deposition (CVD) at Kennametal's Philip M. McKenna Laboratory through Dr. Dennis Quinto. The results were very encouraging. The Al_2O_3 coatings are 2 to 2.5 μm in thickness and appear adherent. The coatings were examined at Philip M. McKenna Laboratory using SEM and X-ray diffraction. SEM showed the coating microstructure to consist of nodular grains approximately 1 to 3 μm in size (Figure 8). X-ray diffraction revealed that the as-coated alumina is a mixture of α-Al_2O_3 and κ-Al_2O_3. Subsequently, the specimens were heat treated at 1200C for 20 hours in air to convert the κ-Al_2O_3 to the α-phase. X-ray diffraction after the heat treatment indicated complete conversion to α-Al_2O_3. Three coated specimens of each of the substrate materials were sent to Temescal for EB-PVD zirconia coating. One of each was kept at GTEC for further analysis of the Al_2O_3 coating.

Alumina interlayers also are being applied by a sol-gel technique at Signal UOP Research Center. These interlayers are expected to be ultrapure α-Al_2O_3, 1 to 2 μm in thickness, and contain a large fraction of micropores (approximately 50 percent).

Temescal is presently procuring feed materials for the application of alumina and mullite by EB-PVD. Eight substrates of RBSN, SSN, and SSC each were supplied to Temescal for development coating.

Twelve substrates of each material also were supplied to Battelle Northwest for exploratory coating experiments to apply aluminum nitride interlayers by reactive sputtering.

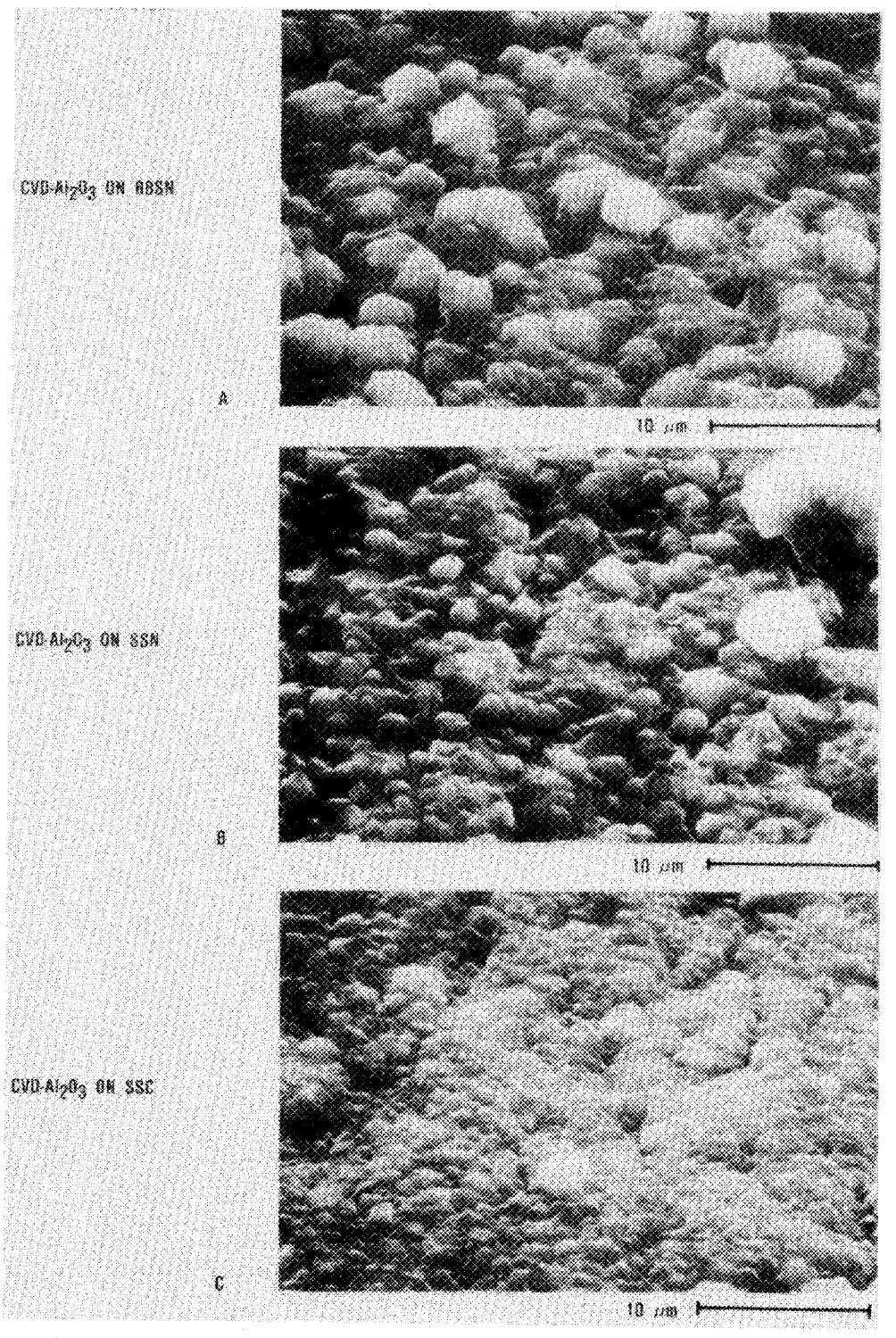

Figure 8. Microstructures of CVD-Al_2O_3 coatings on SiC and Si_3N_4 substrates.

Subtask 3: High Purity Interlayer. Preliminary chemical analysis conducted during Task 1 revealed the presence of impurities in the silicate layer at the coating/substrate interface in oxidized specimens which may have originated from the substrate material. This subtask will concentrate on using an ultrapure CVD-SiC interlayer to determine the effect of substrate purity on coating adherence. CVD-SiC on SSC specimens from a previous GTEC program will be utilized for initial studies. If the results are encouraging, all three substrates will be CVD coated then screened.

Silicon carbide specimens having CVD-SiC coatings were EB-PVD coated with ZrO_2-20%Y_2O_3 at Temescal. Three specimens have been subjected to various heat treatments in static air to determine the effect of a high purity SiC interlayer on coating adherence after oxidation. The analyses to be conducted include flexure testing and fractography, indentation testing, line contact testing, and chemical analysis.

Subtask 4: Diffusion/Gradation Zone. Because all specimens evaluated in Task 1 had an abrupt discontinuity between the coating and substrate, gradation or interdiffusion zones between the coatings and substrates will be evaluated. The candidate approaches are ion implantation, ion mixing, and alloy sputtering with chemical compositions, which may chemically "root" the zirconia to the substrate.

Efforts in the area of a diffusion/gradation zone have not been initiated. Some effort with ion implantation and ion mixing, to achieve a graded interlayer, will be pursued at Oak Ridge National Laboratories.

Subtask 5: Coating Variation. Studies with metal substrates determined that coating adherence can be increased by increasing coating temperature. Prior plasma spray studies suggest a similar condition for ceramic substrates.

As-machined specimens of the three substrate materials were zirconia EB-PVD coated at 1040C instead of at the standard 980C temperature. Visually, these coatings seemed as-clean and as-adherent as the 980C coatings. The specimens were subjected to various heat treatments in static air, then flexure tested at room temperature. The adherence degradation effects of the heat treatment on the 1040C coatings did not differ much from the effect on 980C coatings with respect to flexure testing. The specimens will be indentation tested at UCB to make an assessment of coating adherence.

Subtask 6: Surface Preparation. Adherence of Task 1 specimens was strongly influenced by the surface condition of the original substrate. This task will explore techniques of roughening the surface. Candidates include 150- to 200-grit machining (compared to 320 grit), HF etching (before and after oxidation exposure), abrasive grit blasting, and laser machining. Surface modification experiments will be conducted and specimens selected for coating and adherence evaluation.

An HF etch study was conducted to determine the effect of etch treatments on the surface topography of both as-machined and oxidized substrates. The surface topography was characterized using SEM and the results are shown in Figure 9.

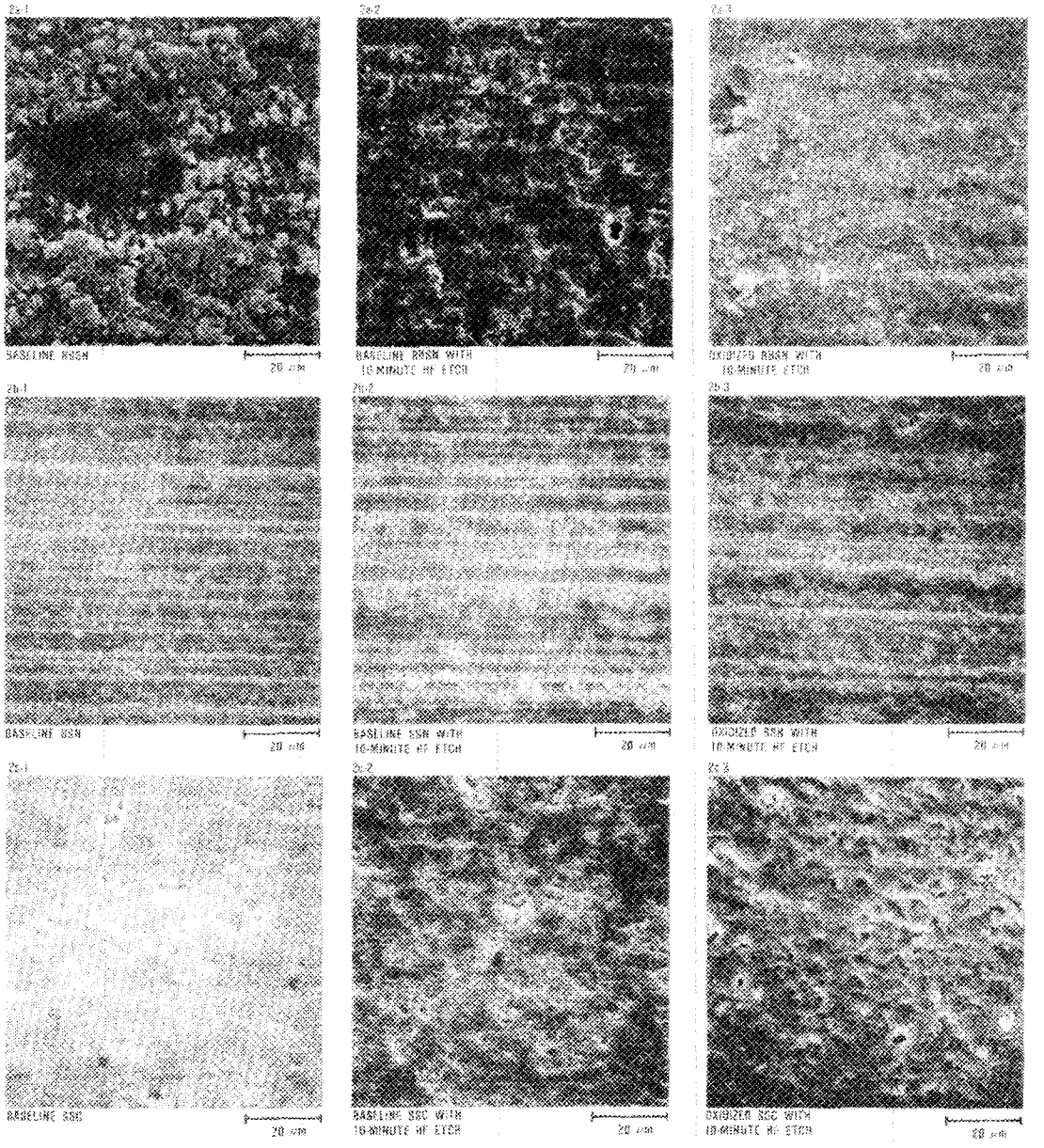

Figure 9. SEM micrographs showing the surface topography of baseline and oxidized substrates after HF etching.

The change in surface roughness observed suggests that HF etching should not significantly improve coating adherence through mechanical interlocking of the coating with substrate surface features. Also, the HF etching is expected to reduce substrate strength although that conclusion cannot be drawn from this study. Subsequently, efforts with HF etching have been discontinued.

A laser machining study is being conducted that uses a CO_2 laser to produce a matrix of pits on substrate surfaces with one diameter spacing. Preliminary studies revealed a strength reduction of about 20 percent for the substrate materials. However, the pits produced by the laser were

very acicular, and measured approximately 0.1 mm in diameter and 0.3 mm deep. The laser power was reduced for each type of substrate to decrease pit depth and increase strength. These specimens were sent to Temescal for ZrO_2 coating.

Subtask 7: Mullite Coating: Several coating runs will be conducted to determine if mullite columnar layers can be deposited on RBSN, SSN, and SSC. Mullite is a better oxygen barrier than zirconia and has a closer thermal expansion match to the SiC and Si_3N_4 substrate materials.

Temescal is procuring material for the application of mullite by EB-PVD as a coating to compare to the presently used ZrO_2-20%Y_2O_3. Temescal also is looking at EB-PVD mullite as an interlayer under Subtask 2.

Summary

During this reporting period Task 1, Coating Adherence and Characteristics Investigation, was completed. Task 1 efforts included preliminary line contact testing and microstructural/chemical analysis. The results are summarized below:

- Both static and sliding bi-axial load contact testing are advantageous to indentation testing in that specimens having poor coating adherence can be evaluated. However, the degree of damage to the system resulting from the test cannot be quantitatively measured as it can for the indentation technique.
- Contact testing, along with indentation testing should be more appropriate for coating adherence assessment than indentation testing alone.
- Based on preliminary contact test results, the coating adherence of oxidized specimens may be closer to acceptable than indentation testing implies.
- Microstructural/Chemical analyses using STEM revealed the presence of a silicate layer at the coating/substrate interfaces. In as-coated specimens, the silicate layer was only chemically detected. In oxidized specimens, the silicate layers were both chemically and visibly detectible and were approximately one to two microns in thickness.
- The growth of the silicate layer during post-coating oxidation is thought to be directly responsible for reduced coating adherence after oxidation.
- Some impurities were detected in the silicate layers and may have a significant effect on oxidation kinetics, thus affecting coating adherence.

During this reporting period Task 2, Advanced Pretreatment and Coating Studies, was initiated. The results of Task 2 efforts thus far are summarized below:

- Oxidation heat treatments at 1200C resulted in significant coating adherence degradation. Increasing the heat treatment duration from 100 to 200 hours does not appear to result in additional degradation. Increasing the oxidation temperature from 1200 to 1400C resulted in additional adherence degradation for RBSN and SSN but not SSC.

- o CVD-Al_2O_3 was applied to RBSN, SSN, and SSC as an oxygen diffusion barrier interlayer, and the interlayers appear well adhered.
- o Increasing the EB-PVD coating temperature from 980 to 1040C does not appear to significantly affect coating adherence.
- o Based on HF etch study results, the substrate surface topography resulting from HF etching of as-machined and oxidized substrates is not expected to significantly improve coating adherence; thus, this effort was discontinued.
- o Based on laser machining study results, the substrate surface topography resulting from laser machining is expected to improve coating adherence. However, there may be a trade-off between coating adherence and strength.

References

1. Ceramic Gas Turbine Engine Demonstration Program, Final Report, DARPA Contract N00024-76-C-5352, May 1982, Garrett Report 21-4410, D.W. Richerson and K.M. Johansen.
2. Contact Stress and Coefficient of Friction Effects on Ceramic Interfaces, Surfaces and Interfaces in Ceramic and Ceramic Metal System, Berkeley, CA, July 29-30, 1980, D.W. Richerson, W.D. Carruthers, L.J. Lindberg.
3. High Temperature Dynamic-Contact Behavior of Sintered Alpha Silicon Carbide, Ceramic Engineering and Science Proceedings, Vol. 4, No. 7-8, 1983, pp. 663-673, J.R. Smyth, D.W. Richerson.

Status of Milestones

The program was restructured and rescheduled during this reporting period. As a result, the program was extended from 27 to 31 months. All major milestones are on schedule.

Publications

A paper, "High Temperature Coating Study to Reduce Contract Stress Damage of Ceramics" was presented at the 22nd Automotive Technology Development Contractors Coordination Meeting in Dearborn, Michigan in November 1984. This paper is expected to be published in the proceedings of the meeting (SAE Order Number P-155).

2.2.2 Dynamic Interfaces

Studies of Dynamic Contact of Ceramics and Alloys for Advanced Heat Engines

K. F. Dufrane, W. A. Glaeser, and I. Sekercioglu (Battelle Columbus Laboratories)

Objective/Scope

The objective of the study is to develop mathematical models of the friction and wear processes of ceramic interfaces based on experimental data. The supporting experiments are to be conducted at temperatures to 1200 F under reciprocating sliding conditions reproducing the loads, speeds, and environment of the ring/cylinder interface of advanced engines. The test specimens are to be carefully characterized before and after testing to provide detailed input to the model. The results are intended to provide the bases for identifying solutions to the tribology problems limiting the development of these engines.

Technical Progress

Specimen Procurement

A selection was made of the materials to be studied in the initial portion of the study. Orders were placed for the following monolithic and coated specimens:

Monolithic Cylinder Specimens

	Quantity	
TS grade magnesia partially stabilized zirconia	11	Nilcra Ceramics, Inc.
Z-191 grade yttria partially stabilized zirconia	11	NGK-Locke, Inc.
Hexoloy™, sintered alpha silicon carbide	11	The Carborundum Co.
2Y20A grade HIP'ed transformation toughened alumina	5	Toya Soda Manufacturing Company, Ltd.

Coated Specimens from Ramsey Piston Ring Division of TRW

Coating Material	Quantity	Specimen Type
RC-6	20	Cylinder
RC-4.1	40	Ring

Tribaloy (Co-based)	40	Ring
Chrome	40	Ring

Delivery times of 6 to 12 weeks were quoted for the specimens, which were ordered in December, 1984, and early January, 1985. However, only the silicon carbide specimens were delivered as of April 15, 1985. The silicon carbide cylinder specimens appear to be in excellent condition and suitable for direct use in the test apparatus. Since all of the ring specimens are based on coatings, the initiation of actual experiments has been delayed awaiting the delivery of the ring specimens.

Experimental Apparatus

Modifications to the experimental apparatus have been completed. A photograph is presented in Figure 1. A heavy-duty, four-cylinder tractor engine provides the basic structure and reciprocating motion. A variable-speed 7-horsepower electric motor drives the engine at rotational speeds from 500 to 2200 rpm. The two reciprocating ring specimens are mounted on a specimen holder attached to the top of one of the pistons. The ring specimens are trapped between the two cylinder specimens, one of which is fixed and the other mounted on linear bearings to provide the load on the contact surfaces. The cylinder specimens are flat, for convenience of production and for ease of surface examinations. The ring specimens are flat along the longitudinal axis, but have the surface profile of actual rings in the vertical (sliding direction).

Temperature control is provided by an insulated stainless steel enclosure around the specimens and electric heaters within the enclosure. A 6-horsepower single cylinder diesel engine provides exhaust gases to the enclosure to reproduce the actual diesel-cylinder environment. Electric heaters in the exhaust stream from the engine raise the gas temperature to the desired operating temperature. The apparatus is designed for operation to 1200 F.

Literature Review

In support of the wear modeling efforts of the program, a literature search was conducted on the topic of wear of ceramics. Approximately 50 pertinent abstracts were identified in the machine search of government and open literature. Full copies of the reports and papers have been procured and reviewed for background information pertinent to the study. A critical review of this literature will be prepared to provide a starting point for the wear modeling associated with the experiment observations of the current study.

Status of Milestones

Delays in receiving the coated ring specimens have delayed the first milestone, the initiation of the actual experimental program. With a promised delivery of late April, 1985, the first experiments should begin in May, 1985. Progress on the wear modeling is on the expected schedule.

Publications

None.

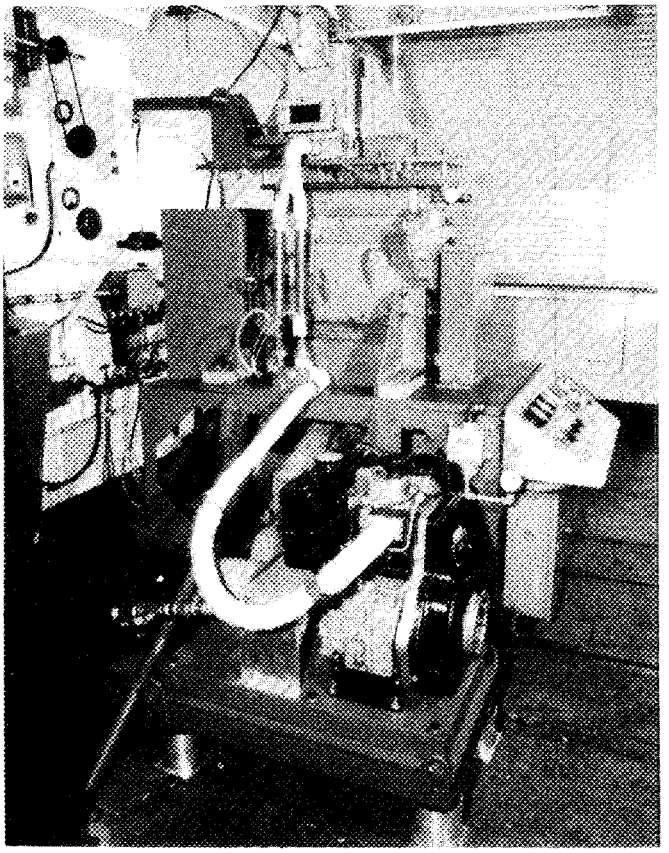

FIGURE 1. HIGH TEMPERATURE CERAMIC WEAR TEST FACILITY

2.3 NEW CONCEPTS

2.3.1 New Concepts

*Advanced Statistics**
W. P. Eatherly (Oak Ridge National Laboratory)

Objective/scope

The third and fourth moments of a statistical distribution (the skewness and kurtosis) can be extensively used in analyses for outlier tests, for goodness-of-fit tests, and for characterization in the Pearson scheme of generalized distributions. This effort is an attempt to calculate these moments for the Weibull distribution for m-values from one to infinity in preparation for Monte Carlo calculations on finite samplings from this distribution.

Technical progress

The calculation of an asymptotic series for the higher moments of the Weibull Distribution has been completed, and a second draft of a topical report is in preparation. Since it will yet be some time until this report is issued, the numerical results are tabulated here.

The behavior of the higher moments is of considerable theoretical interest but is also of direct practical interest in our treatment of the statistical failure criteria for ceramics. Since most of the statistical machinery available to us is built around normal distributions, we are forced to give up a great deal in going to a Weibull-type distribution to describe any aspect of strengths for brittle materials. In particular, we lose or weaken the theory of variance analysis, the ability to express confidence and tolerance limits, and to make goodness-of-fit tests appropriate to tails of a distribution.

Our interest in this problem was initiated by concern over goodness-of-fit tests in particular. The best test on a distribution as a whole is the Kalmogorov-Smirnov One-Sample Statistic, for which critical values are given in various books containing statistical tables.[1] This test compares the expected differences between an observed finite sample and an assumed continuous distribution independent of that distribution. The test, however, is not highly sensitive to the tails but is dominated by the central part of the assumed distribution.

The normal distribution contains two independent parameters, the mean μ and the standard deviation σ. The Weibull distributions at first glance appear to have only one free parameter, the mean μ, but in practice contain a second parameter that places the zero of the scale. Thus, in both distributions one is forced to the third and fourth moments for a goodness-of-fit test sensitive to the tails of the distribution. Hence our interest in these higher moments.

---

*These studies are being jointly supported by the Ceramic Technology for Advanced Heat Engines Program and the HTR Technology Program.

In Table 1, we give the scaled mean μ/θ and the coefficient of variance σ/μ as a function of the Weibull exponent m as calculated from 15-place tables (1, 2; 0.005) of the Γ-function,[2] using quartic interpolation. Also given are the third and fourth normalized central moments, defined as:

$$\beta_n = \frac{1}{\sigma^n} \int_0^\infty (x - \mu)^n \, pdf(x) \, dx \quad .$$

It will be noted, even to this degree of accuracy of the Γ-function, that values for the fourth moment become unusable above $m > 50$. Although m-values for ceramics have generally been observed only in the range $6 < m < 20$, higher values of m become of interest for other materials. These values are plotted in Fig. 1 superposed on uncertainty contours[3] for the normal distribution for which $\beta_3 = 0$ and $\beta_4 = 3$. This figure must be interpreted in the light that around any given m-value there

Table 1. Normalized moments of the Weibull Distribution for various values of the exponent m calculated by quartic interpolation on 15-place table of the Γ-function

m	μ/θ	σ/μ	β_3	β_4
1	1.	1.	2.	9.
2	0.886227	0.522723	0.631111	3.245089
3	0.892980	0.363447	0.168103	2.729464
4	0.906402	0.280544	-0.087237	2.747829
5	0.918169	0.229053	-0.254110	2.880290
6	0.927719	0.193774	-0.373261	3.035452
7	0.935438	0.168022	-0.463190	3.187182
8	0.941743	0.148369	-0.533727	3.327676
9	0.946965	0.132863	-0.590657	3.45521
10	0.951351	0.120310	-0.637637	3.57016
12	0.958286	0.101216	-0.71074	3.76697
14	0.963510	0.087371	-0.76509	3.92777
16	0.967580	0.076866	-0.80712	4.06076
18	0.970838	0.068621	-0.84063	4.1724
20	0.973504	0.061976	-0.86797	4.2670
25	0.978438	0.049902	-0.91846	4.4513
50	0.988844	0.025289	-1.0248	4.879
100	0.994326	0.012733	-1.081	5.1
200	0.997139	0.006390	-1.11	5.

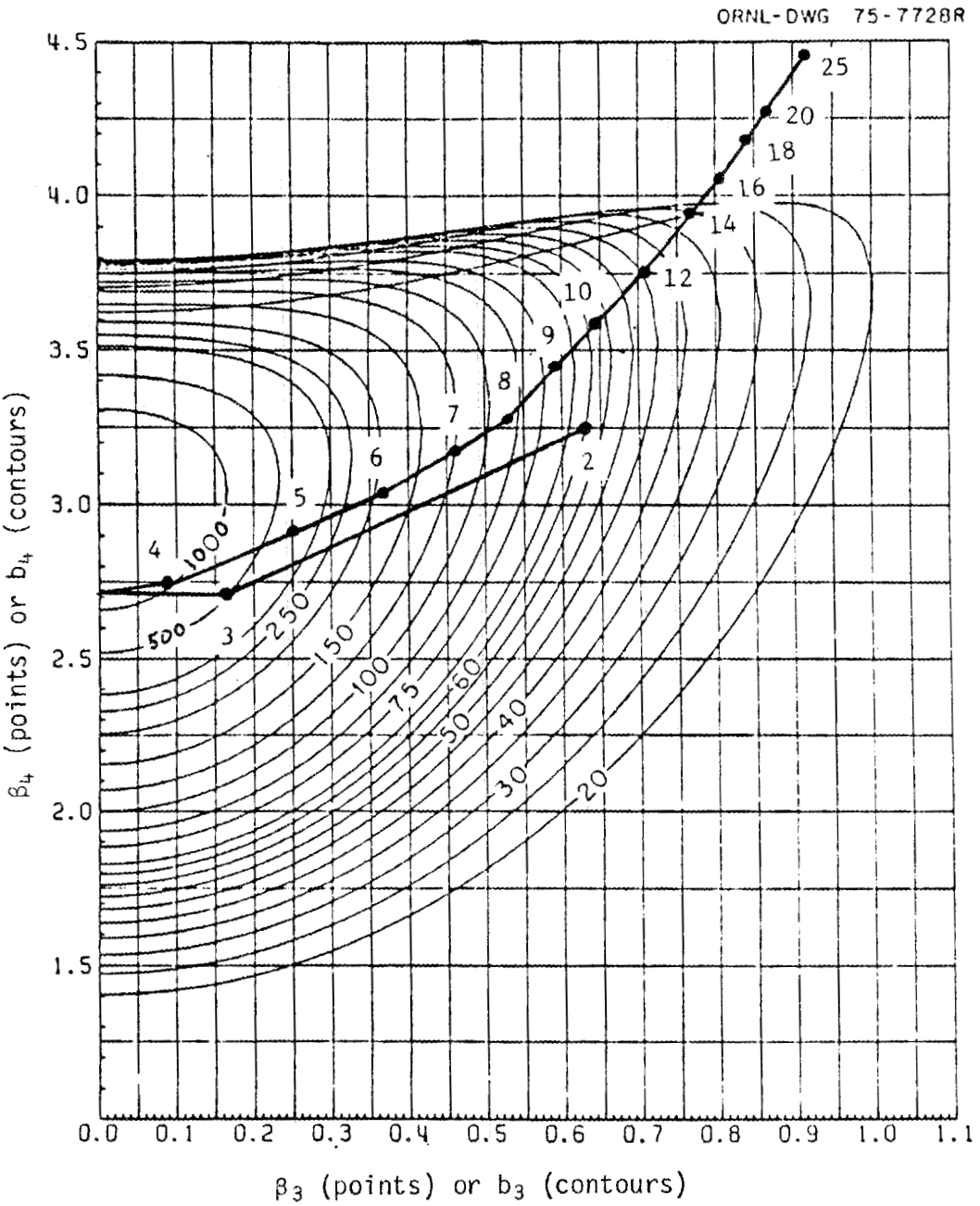

Fig. 1. Values of the moments β_3 and β_4 of the Weibull Distribution superposed on the 90% significance contours of the bivariate moments for the Normal Distribution. Figures on the contours are the sample size from the Normal Distribution. Figures on the points are the values of the Weibull exponent *m*. The upper branch of the curve has negative skewness.

will be a further set of contours relevant to the uncertainty in determining the b_3 and b_4 values from a finite sampling. Clearly, for m near 4, extremely large samplings ($n > 1000$) would be required to distinguish between the Weibull and Normal distributions. This is the problem yet to be solved: How large a sampling is required to distinguish between the two distributions?

In Table 2 we supply for selected m-values the third and fourth normalized central moments as calculated by the asymptotic series. The terms have been calculated and summed (S_8) to the eighth order and an extrapolation formula has been used to estimate the sum to infinite order (S_∞). We note in passing that while the central moments approach zero as m tends to infinity, the normalized central moments do not.

Finally, in Table 3 we present "best" values of the quantities of Tables 1 and 2 truncated to six decimal places where these are known. In regions of weakest overlap between the values calculated from the Γ-function table and the asymptotic series, only four and five decimal

Table 2. Normalized moments of the Weibull Distribution for various values of the exponent m calculated from the asymptotic series to eighth order (S_8) and with the correction term added (S_∞)

m	Order	β_3	β_4
10	S_8	-0.6	4.
	S_∞	-0.6378	3.6
20	S_8	-0.8678	4.3
	S_∞	-0.8679 65	4.267
50	S_8	-1.0248	4.8779
	S_∞	-1.0248 5300	4.8777 82
100	S_8	-1.0810 737	5.1234 5
	S_∞	-1.0810 7376 0	5.1234 456
200	S_8	-1.1100 166	5.2591 46
	S_∞	-1.1100 1656 9	5.2591 4541
500	S_8	-1.1276 6270 6	5.3427 698
	S_∞	-1.1276 6270 6	5.3427 6980 1
∞		-1.1395 4710 0	5.4000 0000 4

Table 3. "Best" values for the normalized moments and associated quantities of the Weibull Distribution for various values of the exponent m

m	μ/θ	σ/μ	β_3	β_4
1	1.	1.	2.	9.
3	0.8929 80	0.3634 47	0.1681 03	2.7294 64
4	0.9064 02	0.2805 44	-0.0872 37	2.7478 29
5	0.9181 69	0.2290 53	-0.2541 10	2.8802 90
6	0.9277 19	0.1937 74	-0.3732 61	3.0354 52
7	0.9354 38	0.1680 22	-0.4631 90	3.1871 82
8	0.9417 43	0.1483 69	-0.5337 27	3.3276 76
9	0.9469 65	0.1328 63	-0.5906 57	3.4552 1
10	0.9513 51	0.1203 10	-0.6376 37	3.5701 6
12	0.9582 86	0.1012 16	-0.7107 4	3.7669 7
14	0.9635 10	0.0873 71	-0.7650 9	3.9277 7
16	0.9675 80	0.0768 66	-0.8071 2	4.0607 6
18	0.9708 38	0.0686 21	-0.8406 3	4.1724
20	0.9735 04	0.0619 76	-0.8679 65	4.2670
25	0.9784 38	0.0499 02	-0.9184 55	4.4528
50	0.9888 44	0.0252 89	-1.0248 53	4.8777 82
100	0.9943 26	0.0127 33	-1.0810 74	5.1254 46
200	0.9971 39	0.0063 90	-1.1100 17	5.2591 45
500	0.9988 50	0.0025 61	-1.1276 63	5.3427 70
∞	1.	0.	-1.1395 47	5.4000 00

places are determinable. More extensive tables will be available in the topical report under preparation. The extrapolation formula carrying the partial sum S_8 toward S_∞ has not yet been bounded, so significant figures made available from this extrapolation have been estimated by comparison with the direct calculation from the Γ-functions.

A program to calculate values of b_3 and b_4 for finite samplings by Monte Carlo means is now being studied under a subcontract for the Ceramic Technology for Advanced Heat Engines Program.

Important findings and observations

Our major conclusions as a result of these calculations, not all demonstrated here, are:

1. The unnormalized central moments μ_n tend to zero as $(1/m)^n$.
2. The normalized central moments $\beta_n = \mu_n/\sigma^{n/2}$ are all finite and are also nonvanishing for all $n > 2$.

3. Discrimination between the Normal and Weibull distributions by a co-variant moment test will almost certainly be difficult unless sample sizes are very large (100s to 1000s of data points). This conclusion, of course, ignores discrimination by fracture location or, equivalently, volume effects.
4. Representation of the Weibull distribution within the Pearson scheme appears unprofitable because of the relative size of the moments as their order n increases.

A topical report presenting these results is in preparation.

References

1. For example, Donald B. Owen, *Handbook of Statistical Tables*, Addison-Wesley, Reading, Mass., 1962.

2. Milton Abramowitz and Irene A. Stegun, eds., *Handbook of Mathematical Functions With Formulas, Graphs, and Mathematical Tables*, Applied Mathematics Series 55, National Bureau of Standards, U.S. Government Printing Office, Washington, D.C., Third Printing, March 1965.

3. Komiko O. Bowman and Leroy R. Shenton, *Moment* $(\sqrt{b}_1, \sqrt{b}_2)$ *Techniques*, ORNL/CSD-83, August 1981.

3.0 DATA BASE AND LIFE PREDICTION

INTRODUCTION

This portion of the project is identified as project element 3 within the work breakdown structure (WBS). It contains five subelements, including (1) Structural Qualification, (2) Time-Dependent Behavior, (3) Environmental Effects, (4) Fracture Mechanics, and (5) Nondestructive Evaluation (NDE) Development. Research conducted during this period includes activities in subelements (1), (2), and (3). Work in the Structural Qualification subelement includes proof testing, correlations with NDE results and microstructure, and application to components. Work in the Time-Dependent Behavior subelement includes studies of fatigue and creep in structural ceramics at high temperatures. Research in the Environmental Effects subelement includes study of the long-term effects of oxidation, corrosion, and erosion on the mechanical properties and microstructures of structural ceramics.

The research content of the Data Base and Life Prediction project element includes (1) experimental life testing and microstructural analysis of Si_3N_4 and SiC ceramics, (2) time-temperature strength dependence of Si_3N_4 ceramics, and (3) static fatigue behavior of PSZ ceramics.

Major objectives of research in the Data Base and Life Prediction project element are understanding and application of predictive models for structural ceramic mechanical reliability, measurement techniques for long-term mechanical property behavior in structural ceramics, and physical understanding of time-dependent mechanical failure. Success in meeting these objectives will provide U.S. companies with the tools needed for accurately predicting the mechanical reliability of ceramic heat engine components, including the effects of applied stress, time, temperature, and atmosphere on the critical ceramic properties.

3.2 TIME-DEPENDENT BEHAVIOR

3.2.1 Time-Dependent Behavior

Characterization of Transformation-Toughened Ceramics
L. J. Schioler (Army Materials and Mechanics Research Center)

Objective/scope

Because of their unusual combination of properties, transformation toughened zirconias (TTZ) are leading candidates for cylinder liners, piston caps, head plates, valve seats and other components for the adiabatic engine. These materials age-hardened ceramic alloy systems and as such, they are likely to be susceptible at overageing and loss of strength at long times at high temperatures (i.e., close to the age hardening temperatures). The possibility of overaging with its likely negative impact on materials performance was identified as a critical area of ignorance in the preliminary technology assessment on ceramics for diesel engines previously prepared by AMMRC. Accordingly, a task was initiated to a) define the extent and magnitude of the overageing (if any) and b) develop toughened ceramic alloy systems which would not be susceptible to overageing at temperatures which may be encountered in advanced diesel engines (1000C - 1200C). Figure 1 gives an overview of the objective and approach of these two tasks. Note that in-house as well as contractural efforts are involved.

Technical Progress

(Army Materials and Mechanics Research Center)

Analysis of the second generation of TTZ and University of Michigan zirconia toughened alumina (ZTA) materials is nearing completion. Fractography of the >300 breaks is proceeding well. Preliminary results indicate that the fracture origins are processing defects or machining damage.

SR and STSR of the U. Mich. ZTAs is complete; analysis is proceeding. Tests of the second generation materials has been initiated. These tests will not be completed until well into 1985 as only three furnaces are available.

Status of milestones

(Army Materials and Mechanics Research Center)

A search for appropriate Japanese materials to examine in 1985 is under way. Submission of the purchase requests for the materials and for the machining has been delayed as 1985 funds have not yet arrived.

The annual report is delayed in order to include the results on the second generation TTZs and ZTAs.

FIGURE 1

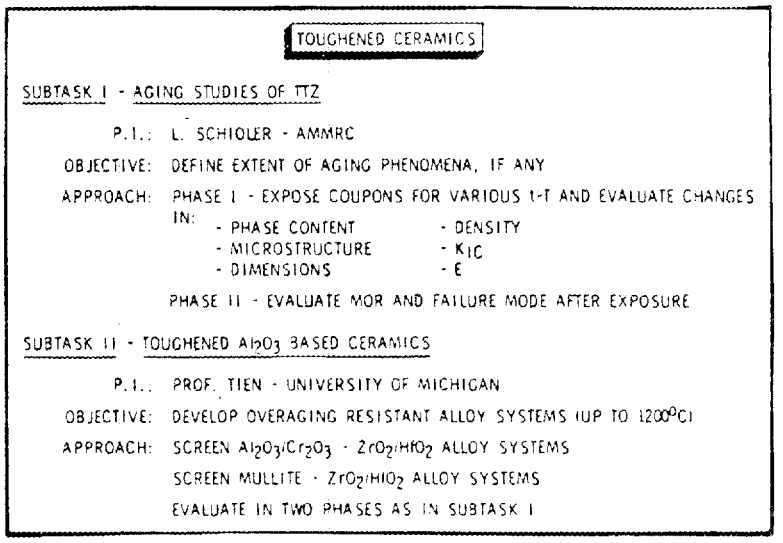
TOUGHENED CERAMICS
SUBTASK I - AGING STUDIES OF TTZ
P.I.: L. SCHIOLER - AMMRC
OBJECTIVE: DEFINE EXTENT OF AGING PHENOMENA, IF ANY
APPROACH: PHASE I - EXPOSE COUPONS FOR VARIOUS t-T AND EVALUATE CHANGES IN:
- PHASE CONTENT
- MICROSTRUCTURE
- DIMENSIONS
- DENSITY
- KIC
- E
PHASE II - EVALUATE MOR AND FAILURE MODE AFTER EXPOSURE
SUBTASK II - TOUGHENED Al2O3 BASED CERAMICS
P.I.: PROF. TIEN - UNIVERSITY OF MICHIGAN
OBJECTIVE: DEVELOP OVERAGING RESISTANT ALLOY SYSTEMS (UP TO 1200°C)
APPROACH: SCREEN Al2O3/Cr2O3 - ZrO2/HfO2 ALLOY SYSTEMS
SCREEN MULLITE - ZrO2/HfO2 ALLOY SYSTEMS
EVALUATE IN TWO PHASES AS IN SUBTASK I

Publications

1. L.J. Schioler, Editorial Introduction, Am. Ceram. Soc. Bull., 64 [2] 268 (1985)

2. L.J. Schioler, "Workshop Studies Ceramic Engines - Current Status and Future", Am. Ceram. Soc. Bull., 64 [2] 269-70 (1985)

3. L.J. Schioler, R.N. Katz, A.C. Gonzalez, and B.R. Lawn, "The Effect of Overaging on the Room Temperature Strength of Partially Stabilized Zirconia", Am. Ceram. Soc. Bull., 64 [2] 326-27 (1985)

4. L.J. Schioler, R.N. Katz, T. Brog, and T.Y. Tien, "Mechanical Properties of Zirconia-Toughened Alumina", submitted to the Proceedings of the American Ceramic Society

5. L.J. Schioler and J.W. Adams, "Phase Analysis of Zirconia Systems Using X-Ray Diffraction", in preparation

6. L.J. Schioler, "The Effect of Time-at-Temperature on Toughened Oxide Ceramics", Annual report, DOE Contract #DE-AI01-77CS51017, in preparation

Presentations

1. L.J. Schioler, R.N. Katz, T. Brog, and T.Y. Tien, "Mechanical Properties of Zirconia-Toughened Alumina", presented at the 9th Annual Conference on Composites and Advanced Ceramics, Ceramic-Metal Systems Division, the American Ceramic Society, Cocoa Beach, FL, January 1985

2. T.Y. Tien, "A Potential Heat Engine Materials - $Al_{(2-x)}Cr_xO_3$-$Zr_{(1-y)}Hf_yO_2$ Composites", presented at the 9th Annual Conference on Composites and Advanced Ceramics, Ceramic-Metal Systems Division, the American Ceramic Society, Cocoa Beach, FL, January 1985

Time-Temperature Dependence of Advanced Ceramics

G. D. Quinn (Army Materials and Mechanics Research Center)

Objective/Scope:

Stepped temperature stress rupture (STSR) testing and limited supplemental standard stress rupture (SR) tests are performed to obtain a preliminary evaluation of strength retention with time under load at various temperatures for new high performance ceramics.

Technical Progress:

Testing has continued without interruption and all equipment is functioning smoothly. New high temperature flexural fixtures that have rolling load bearings are in use. Some effort was expended in increasing the operational capabilities of the Mechanical Behavior and Testing Branch from three to six furnaces. In the meantime, eight furnaces in the Ceramics Research Division have been allocated to this task.

Two materials were tested during this six month period: University of Michigan siliconized silicon carbide and Ford sintered silicon nitride, grade RM-20. Technical highlights are described below. A report has been written and delivered to the Technical Reports Branch for the former material, but a decision whether to document the RM-20 results has not been made.

The University of Michigan siliconized silicon carbide material was developed by Professor E. Hucke. A polymer precursor is carbonized to form a very fine carbon skeleton which is then infiltrated by silicon. The basic premise of this approach is that since strength often scales in direct proportion to microstructure size, then a very fine microstructure will lead to high strength. This objective has been demonstrated since the AMMRC measured fast fracture strength is 680 MPa, higher than any other form of siliconized SiC. High temperature testing indicates this material had excellent oxidation, static fatigue and creep resistances. This material has been able to sustain high stresses at 1200^{o}C and above. One trial is still underway (4500 hours) at 1200^{o}C and 450 MPa. Unfortunately, strength scatter is high, due in part to multiple flaw populations and microstructural non-uniformity. Surface layer irregularities also are of concern as is the low inherent fracture toughness (2.5 MN/m$^{1.5}$) of this material. Attempts to fabricate stronger material will not likely succeed since machining damage (incurred despite very careful preparation) will be limiting. Increased microstructural uniformity should be a goal.

The Ford RM-20 sintered silicon nitride is being developed as a possible AGT material and is additionally slated for detailed studies in the Life Prediction Methodology Task VI. A very small lot of specimens was received and a truncated test sequence was performed. STSR testing revealed a significant strength loss from room to 1000°C although no catastrophic instability occurred. Additional strength losses and mediocre creep and static fatigue resistance at 1200° and 1300°C indicate further material development is necessary.

GTE Wesgo SNW-1000 grade of sintered silicon nitride was received and flexural specimens prepared. Testing was terminated after it was determined that room temperature strength was too low because of a processing problem. A new lot is being prepared by GTE to replace the unrepresentative lot. A three month delay is our testing is therefore projected. This material is also a candidate for further studies in Task VI, Life Prediction Methodology, and has been chosen for IEA round robin testing activities.

Lucas Syalon, heat engine grade, has been received and flexure specimens are being prepared. Kyocera sintered silicon nitride SN-220 is on order.

Milestones:

University of Michigan siliconized SiC tested, evaluated and a report written.

Ford RM-20 evaluated.

Lucas Syalon procured.

GTE Wesgo SNW-1000 procured and tested. Testing suspended due to unrepresentative lot.

GTE A4-6 results published.

Publications:

1. "Static Fatigue of a Sintered Silicon Nitride", AMMRC Technical report. TR84-40, dated October, 1984 was released in April 1985.

2. "Mechanical Property Evaluation at Elevated Temperature for Sintered Beta Silicon Carbide." This report has been prepared as an AMMRC Technical Report, but will also be submitted to Elsevier Publications for their High Technology Ceramics Journal.

3. "Static Fatigue for a Siliconized Silicon Carbide" has been sent to AMMRC's Technical Report Department.

Fracture Behavior of Toughened Ceramics

P. F. Becher and J. C. Ogle (Oak Ridge National Laboratory)

Objective/scope

Because of their excellent toughness, oxide ceramics such as partially stabilized zirconia (PSZ), dispersion-toughened alumina (DTA), and whisker-reinforced ceramics are prime candidates for many diesel engine components. The enhanced toughness of the PSZ and DTA materials is thought to be due to a stress-induced transformation (of the dispersed phase), which requires additional energy in order for catastrophic fracture to occur. However, these materials are still susceptible to slow crack growth and thus strength degradation. Also, there is limited evidence that, at temperatures above 700°C, time-dependent aging effects can reduce the concentration of the phase involved in the transformation process, leading to significant losses in toughness and strength. Again, it is essential that mechanisms responsible for both the slow crack growth and aging behavior be well understood. Similarly the toughening behavior in whisker-reinforced ceramics and their high-temperature performance must be evaluated in order to develop materials for particular applications.

In response to this need, studies have been initiated to examine toughening and fatigue properties of PSZ, DTA, and whisker-reinforced materials. Particular emphasis has been placed on understanding the effect of microstructure upon processes responsible for time-dependent variations in toughness and high-temperature strength. In addition, fundamental insight into the slow crack growth behavior associated with these materials is being obtained.

Toughening by whisker reinforcement

Studies of the toughening behavior of alumina ceramics reinforced by single-crystal SiC whiskers revealed that the primary toughening mode can be altered. Initial results showed that crack deflection by the whiskers was the primary toughening mechanism (Fig. 1).[1] In this case the increased toughness saturates at SiC whisker volume fractions (V_f) of 0.2 to 0.3. The fracture toughness (K_{IC}) level at which saturation occurs increases with increasing whisker length (l) to radius (r) ratio.[2] However, whisker pullout can be promoted by lowering the fiber-matrix interfacial shear strength (τ_i), by decreasing the whisker length, or by increasing the fracture strength of the whisker (σ_f^w). The magnitude of τ_i will be determined during pullout by the radial stress on the fiber-matrix interface (σ_r) and the static coefficient of friction (μ_s) of the interface. The radial stress results from the difference between the thermal expansion coefficient of the whisker (α_w) and matrix (α_m) and is introduced during post-fabrication cooling. When $\alpha_w > \alpha_m$, σ_r is tensile; τ_i will be very small and fiber pullout is promoted. This is the case in the SiC-fiber-reinforced LAS and glass matrices, Fig. 1, where τ_i is ≈2 MPa (i.e., $\tau_i \to 0$) (ref. 3).

In the case of the alumina matrix, $\alpha_m > \alpha_w$ and σ_r is compressive so that the whisker is effectively clamped by the greater contraction of the matrix and τ_i is increased. On the basis of this analysis one can see

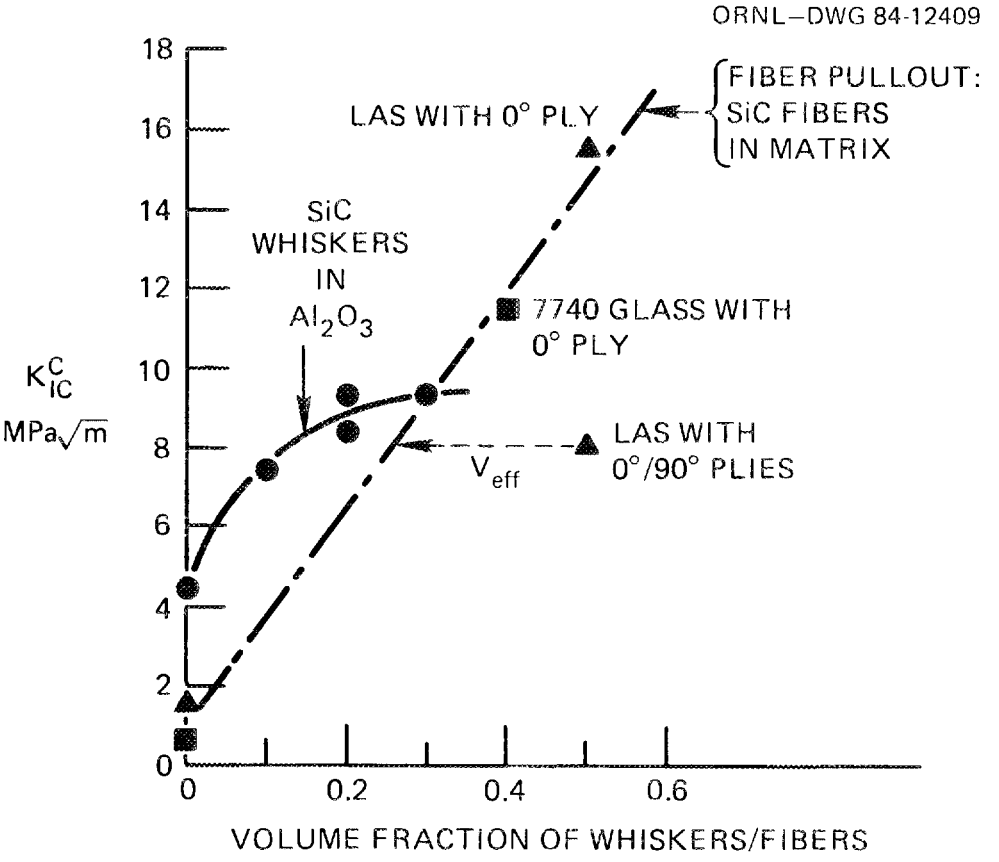

Fig. 1. Toughening behavior in ceramics reinforced with SiC whiskers and fibers. Data for and observations with continuous-SiC-fiber-reinforced ceramics indicate that fiber pullout is the primary mode of toughening. However, in SiC-whisker-reinforced alumina, initial results indicated that crack deflection by the whiskers was the primary toughening process. Changes in whisker properties and characteristics (especially whisker length) and interfacial shear strength can be utilized to enhance toughening by whisker pullout.

that changing the matrix to influence the value of $(\alpha_w - \alpha_m)$ can significantly alter the contribution of whisker pullout. This analysis of τ_i assumes that no chemical bonding occurs at the fiber-matrix interface so that τ_i is dominated by η and σ_r. In fact for composites where improvements in toughness by whisker pullout are sought, one wants to avoid significant chemical bonding at the fiber-matrix interface because τ_i will increase.

In composites where $\alpha_m > \alpha_w$, one can decrease the whisker length (l) and promote toughening by pullout. This occurs because stressing a whisker crossing the crack plane results in an increase in tensile stress in the whisker as a function of distance from the crack plane. When $l > l_c$, the

tensile stress acting on the whisker exceeds the whisker fracture strength (σ_f). Fracture of the whisker rather than pullout occurs then for $l > l_c$. By reducing l to values below l_c, pullout is promoted and greater toughness is achieved.

Studies of the influence of stressing rate particularly at elevated test temperatures on the mechanical properties of alumina reinforced with 20 vol % SiC whiskers with and without densification additives were initiated. The initial results obtained at room temperature are given in Table 1. Briefly these results reveal that the hardness is decreased with the use of the MgO and Y_2O_3 additives. The lower flexural fracture strength in sample SCW-60-1, Table 1, may not be solely a result of the additives, although the Y_2O_3 results in formation of at least $Y_3Al_5O_{12}$ second-phase regions that could act as flaws or defects. In addition, though, large pyrolyzed remanents of the rice hulls from the SiC whisker growth are found in the composites and often act as failure initiation sites. One can see that the composites containing the MgO and Y_2O_3 additives apparently exhibit some anomalous dependence of K_{IC} on stressing rates at room temperature. Test results at 1000°C are being evaluated.

Transformation-Toughened PSZ

Studies of the change in the mechanical properties of a PSZ ceramic as a result of exposure to an applied flexure stress for up to 1000 h at temperatures of up to 1000°C were recently completed. Previously it was shown that when subjected to an applied stress equivalent to 60% of the fast fracture strength at a given temperature (i.e., $t = 0$ h) the Nilsen TS grade PSZ ceramic (lot 83-065) exhibits a decrease in retained flexure strength (at temperature) with increasing exposure time at 1000°C but not at 500°C.[4] The current results, Fig. 2, include the changes in retained strengths at temperature observed for exposure times of up to 1000 h at 800°C.

In comparing these data, first notice that the incubation time for the initial increase in retained strength ($t > 24$ h) increases as the temperature is decreased. Second, it appears that strength changes are not occurring at 500°C.

After the initial strengthening effects, there is an associated decrease in the retained strength with increase in exposure time. Finally, after a 1000-h exposure, the ratio of the retained strength to that after the 24-h exposures increases from 0.82:1 to 1:1 as the temperature decreases.

These results can be used for two purposes here. First they indicate that this particular lot of PSZ material exhibits mechanical strengths that are quite stable for long periods of exposure to temperatures up to at least 500°C and to applied stresses up to 60% of the fast fracture strength. For many applications this characteristic stability of the mechanical properties is critical.

Second, screening of materials by similar testing but at only one temperature — either with or without an applied stress — does not give a sufficient assessment of the material's performance. For example at 1000°C this PSZ would not look very promising, but at room temperature it

Table 1. Mechanical properties of alumina composites containing 20 vol % SiC whiskers at 22°C, 40% relative humidity

Sample	Flexural fracture strength, MPa with 180 grit diamond surface ground tensile surface ⊥ HPA	Mechanical properties with polished surfaces ⊥ HPA		Mechanical properties with multiple controlled DPH indent (1.39 N load) flaws polished tensile surface ⊥ HPA			
		Indent K_c(MPa $\sqrt{m}$) 1.39 N load	DPH (GPa)	Stressing rate (MPa/s)	Final flaw radius (μm)	Resultant flexure strength (MPa)	Fracture toughness (MPa $\sqrt{m}$)
SCW-60-1 0.5 wt% MgO 2.0 wt% Y_2O_3 98.6% T.D.	472 ± 56	8.6 ± 0.6	17.20 ± 0.98	9.3×10^2	361 ± 63	261 ± 9	9.3 ± 1.1
				$\sim 1 \times 10^2$			7.9 ± 0.3
				9.3×10^{-2}	292 ± 21	222 ± 9	7.0 ± 0.5
SWC-61-1 99.9% T.D.	607 ± 77	8.8 ± 0.8	22.18 ± 2.94	6.1×10^2	262 ± 27	248 ± 8	7.4 ± 0.3
				$\sim 1 \times 10^2$			7.8 ± 0.7
				6.1×10^{-2}	342 ± 128	240 ± 26	8.1 ± 1.5

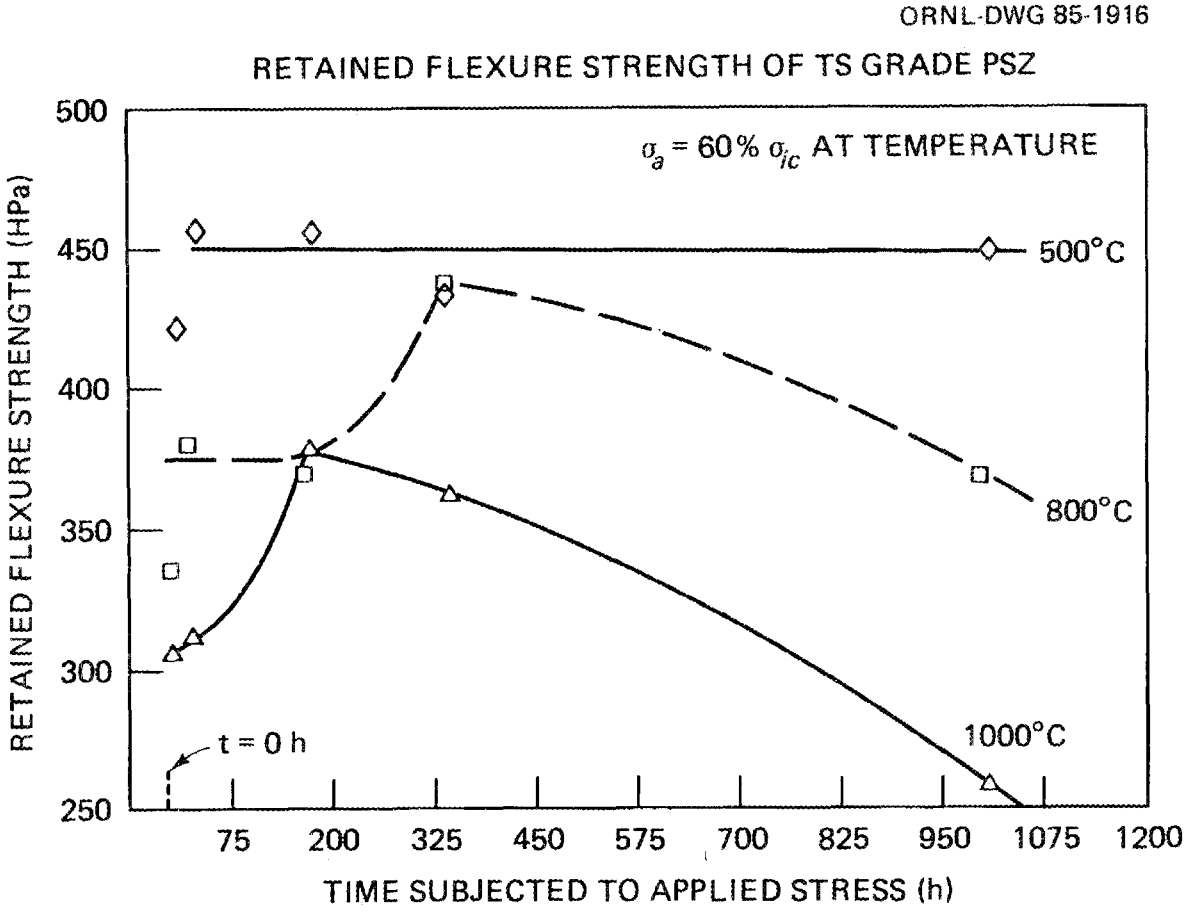

Fig. 2. Strength changes occur when PSZ samples are subjected to a flexure stress for various exposure periods at temperatures greater than 500°C. Note that the applied stress used for each test temperature is 60% of the fast fracture strength (t = 0 h). Retained strengths are determined at the same temperature as that used in exposing the samples to an applied stress.

has high fracture strength and toughness.[4] Thus one needs to characterize the response of the materials over a range of temperatures to accurately describe their performance capabilities.

References

1. P. F. Becher and G. C. Wei, "Toughening Behavior in SiC Whisker Reinforced Alumina," *Communications American Ceramics Society*, in press (1984).

2. K. T. Faber and A. G. Evans, "Crack Deflection Processes — I. Theory," *Acta Met.* **31**(4), 577–84 (1983).

3. D. Marshall, Rockwell Science Center, personal communication, 1984.

4. P. F. Becher and M. K. Ferber, "Static Fatigue Behavior of Toughened Ceramics," pp. 109–15 in *Ceramic Technology for Advanced Heat Engines Project Semiannual Progress Report for Period April 1984 to September 1984*, ORNL/TM-9497, February 1985.

Cyclic Fatigue of Toughened Ceramics

K. C. Liu and C. R. Brinkman (Oak Ridge National Laboratory)

Objective/scope

The objective of this work is to develop a system of bend-free tensile load train column capable of performing tension-tension dynamic fatigue in uniaxial mode for high-temperature structural ceramics and other brittle materials. Attention is focused on two areas of research involving (1) design, fabrication, and demonstration of a self-aligning grip housing and a load train column assembly that can transmit the uniaxial load passing through the center of the specimen cross-section without introducing bending stresses; and (2) design and analysis of tensile specimen geometry for cyclic fatigue testing.

Technical highlights

Development of self-aligning grip system

Gas bearings are used in some tensile machines intended for self alignment, and they eliminate the bending of uniaxially loaded tensile specimens. Theoretically speaking, they should work and serve the purpose if they operate under ideal conditions. Two basic requirements are that the gap between the two spherical bearing surfaces must be uniform and the lifting pressure be applied uniformly over the bearing area. Drawbacks are that neither the gap nor the pressure distribution can be measured directly to ensure proper operation. Furthermore, it remains questionable whether the gas bearings will operate properly under dynamic cyclic loading, which is the major mode of operation of interest here. Lack of reliable methods to monitor the performance was an important reason why the gas bearings were not selected in the current system design. Moreover, the gas bearings are expensive, and the cost of operation is also high.

The newly developed ORNL grip system consists of eight individual supporting mechanisms that carry equal shares of the load applied to the pull rod. Because each of the reactive loads can be measured directly with load transducers, the eccentricity of the loading point of the resultant force can be analyzed quantitatively. Good design versatility also permits an unlimited choice of tensile specimens, which can be either rods or plates.

Performance was evaluated for the self-aligning grip housing with a special load applicator instrumented with strain gages. Four sets of full bridge circuits were used as load transducers to monitor the distribution of the reacting loads supported by the eight mechanisms built in the grip housing. The outputs of the total applied load and strain gages were recorded continuously by a data acquisition system while cyclic loading was being applied to the grip housing. To avoid unconscious bias in the measuring method and to balance out inherent errors in the measuring system, the load applicator was rotated one-eighth turn successively at each test run so that the loads imposed on the supporting mechanisms were measured by different bridge circuits. The maximum offset from the

linearity between the applied load and strain gage outputs was less than 0.5% for a full-scale loading of 5000 lb. A typical distribution of the divided loads was measured to be 624.26, 624.49, 627.88, 623.17, 624.64, 624.61, 624.9, and 626.05 lb, respectively, on each of the eight supporting subsystems. The maximum deviation from the average value of 625 lb was 0.46%. On the basis of these test data, the eccentricity of the resultant load was calculated to be less than 0.001 in. for a first calibration test and less than 0.0006 in. in the second calibration test. A matching set of the grip housing for the lower grip and a complete set of the pull rod assembly are now being fabricated for a final evaluation test.

Analysis of tensile fatigue specimen

Stress analyses were performed for a dog-bone-shaped tensile specimen (Fig. 1) by using a finite-element analysis technique. Shown also in Fig. 1 is a finite-element grid for the fourth quadrant of the specimen. To avoid abrupt changes in stress, the transition between the uniform gage section and the specimen shank is blended smoothly with a double-flexure elliptical fillet having a major-to-minor diameter ratio of 4. The analyses were made for specimens in the shape of a solid rod as well as that of a flat plate assumed to have the same profile and to use the same finite-element grid.

Results of the stress analyses are summarized in Figs. 2 and 3. Figure 2 shows the distribution of dimensionless tensile stress under elastic loading. Four curves numbered from 1 to 4 delineate the change of the tensile stress along four rows of the grid elements labeled accordingly from the row next to the center line toward the outside. Failure to bring all four curves into a single line indicates that the tensile stresses are not ideally uniform in the transition section. However, they fall reasonably close to each other in the area immediately outside the gage section and somewhat apart in the section between the flexure point and the specimen shank. The situation is more pronounced, but only slightly so, in the plate specimen compared with that in the rod specimen. The nonuniformity of the stress distribution in the lower stress range is not important here. The stress riser in the outer elements adjacent to the end of the gage section is about 1% for the rod specimen and about 2% for the plate specimen. In both cases, the stress concentration normally occurring at the junction between the gage section and short circular transition fillet is virtually eliminated.

Elastic-plastic analyses were performed for the same specimen geometry, and the results are summarized in Fig. 3. Only the elements falling between the flexure points were loaded plastically. No significant changes are observed in the stress pattern due to the redistribution of inelastic stresses developed in the plastically deformed elements. Hence, no significant new information was gained.

In summary, the above finite-element analyses indicate that no significant stress riser will occur in the dog-bone-shaped tensile fatigue specimen provided the transition between the uniform gage and shank is blended smoothly by using a double-flexure elliptical fillet with a major-to-minor diameter ratio of 4 or higher.

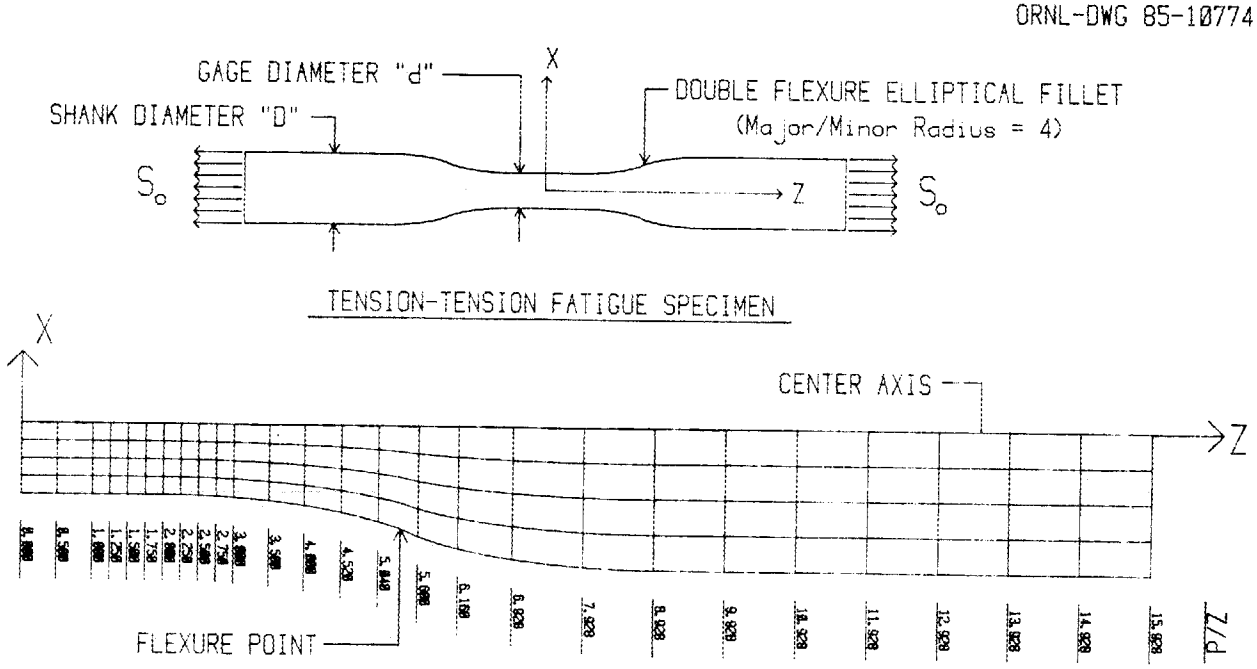

Fig. 1. Tensile fatigue specimen with double-flexure elliptical fillet (top) and fourth-quadrant finite-element grid (bottom).

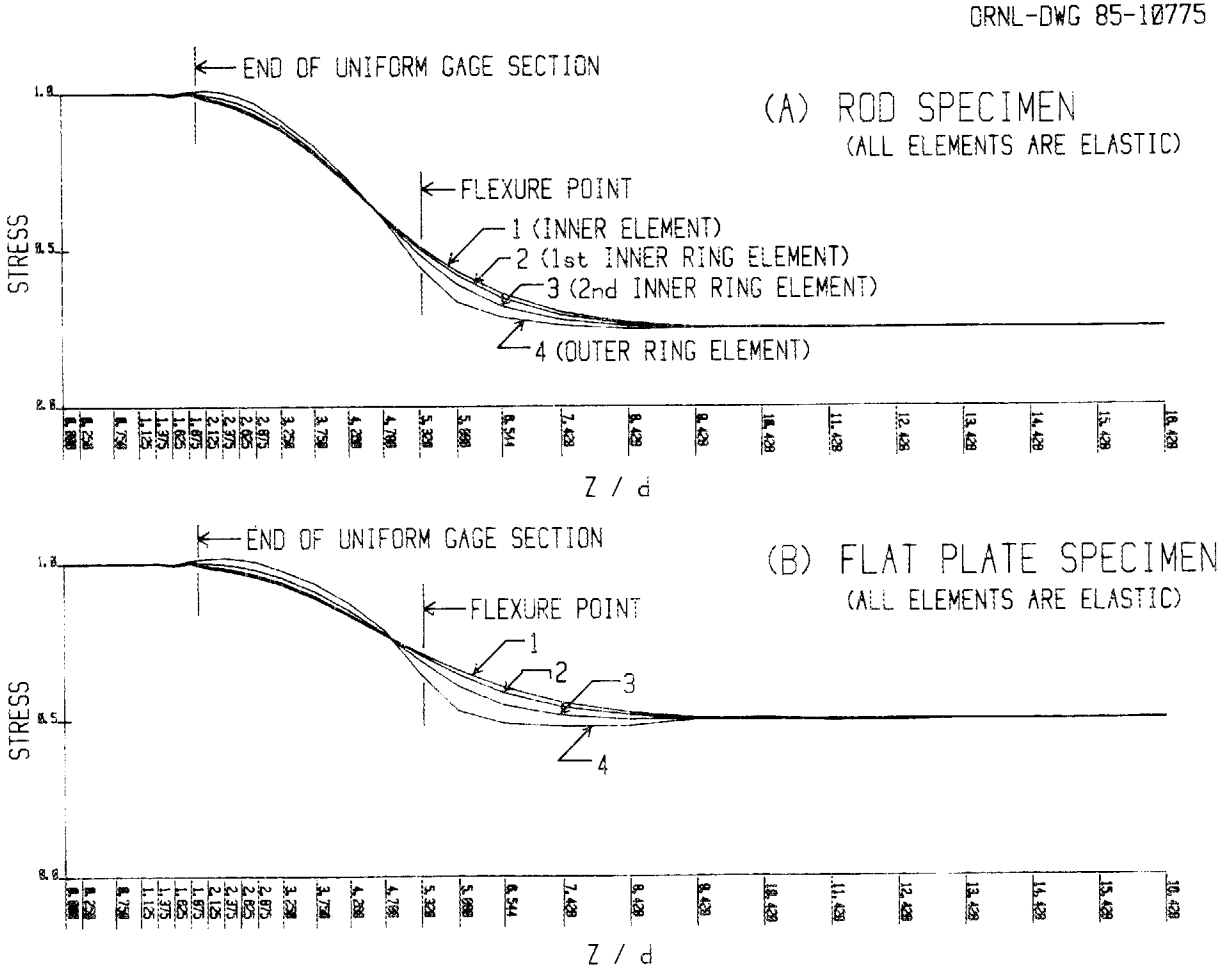

Fig. 2. Tensile stress distribution for rod (A) and flat plate specimen (B) subjected to elastic loading.

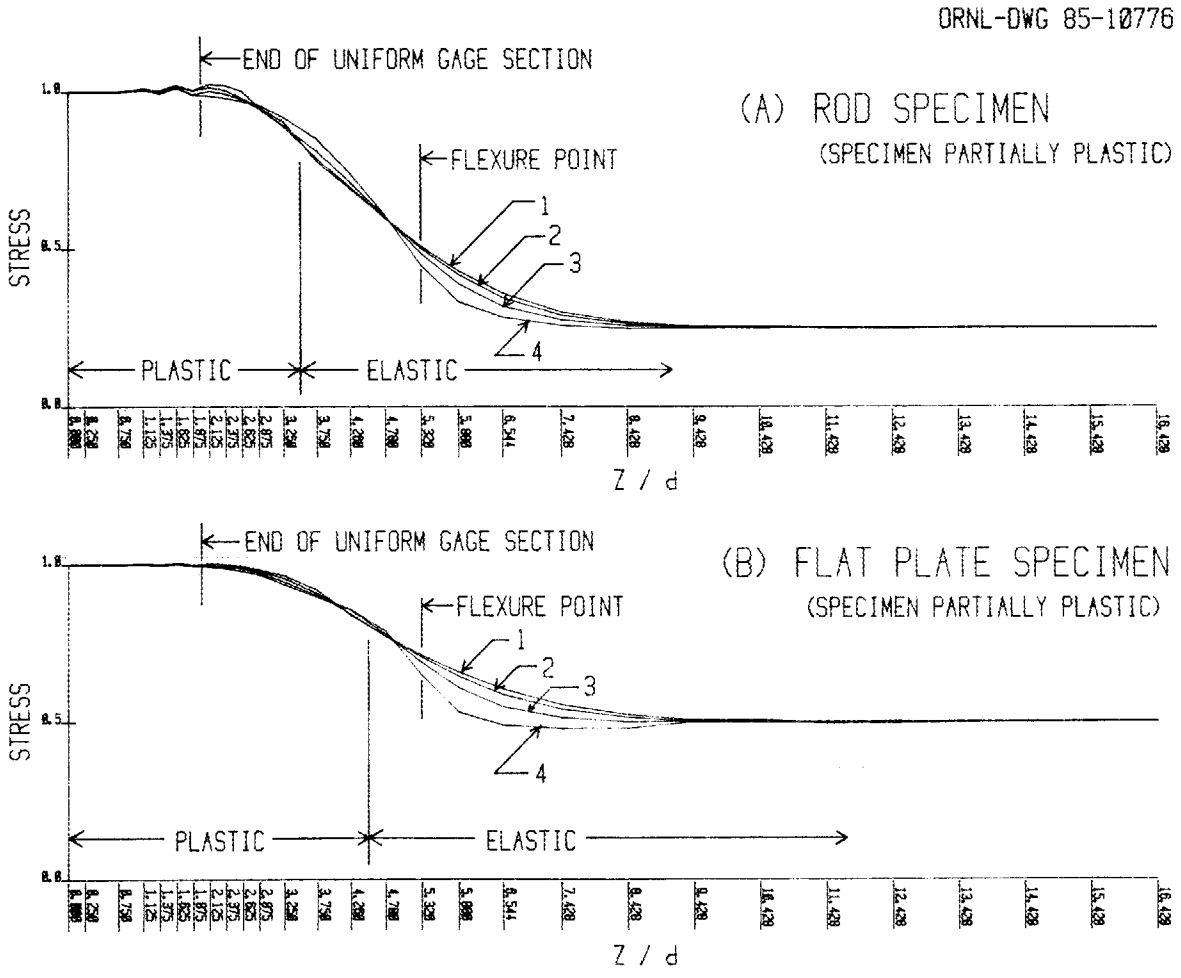

Fig. 3. Tensile stress distribution for rod (A) and flat plate specimen (B) subjected to plastic loading in the gage section.

Status of milestones

321401 Complete design fabrication, installation, and initial phase of evaluation of tension-tension fatigue grips for testing advanced ceramic materials. (Sept. 30, 1985)

Initial evaluation has been completed for the tension-tension fatigue grips, and the progress is on schedule.

Communications/visitors/travel

K. C. Liu visited the National Bureau of Standards and Naval Research Laboratory in Washington, D.C., on November 20–21, 1985, for discussions and an exchange of information concerning specimen preparation, surface finishes, and experimental techniques of conducting tension-tension dynamic fatigue testing of high-temperature ceramics. The general concensus was that the ceramics community clearly needs a reliable but relatively simple and cost-effective technique to generate useful information, which can be obtained preferably by using uniaxial testing methods. All agreed that the exchange of information was mutually beneficial.

Problems encountered

None.

Publications

None.

3.4 FRACTURE MECHANICS

3.4.1 Fracture Mechanics

Improved Methods for Measuring the Fracture Resistance of Structural Ceramics

R. C. Bradt and A. S. Kobayashi (University of Washington)

Objective/Scope

The long-term goals of this study are to develop and demonstrate a technique comprising one measurement, or a technique comprising a set of correlative measurements for structural ceramics including monolithic and composite materials which will allow the reliable and accurate determination of their resistance to fracture (crack propagation)over a broad temperature range from 25°C to 1400°C.

Technical Progress

This is the first semi-annual progress report of this program. During this period, efforts have been made to obtain the structural ceramic materials $MgAl_2O_4$, SiC, and Si_3N_4 from commercial sources and to set-up and make preliminary runs to adapt the laser interfermetric strain gage technique (LISG) to ceramic materials, first at room temperature and then at elevated temperatures. The $MgAl_2O_4$ has recently been received and specimens are now being prepared. Receipt of the SiC and Si_3N_4 materials is expected in the near future.

Initial difficulties with the LISG displacement measurement technique have been overcome by modifying the indentation fiducial markings using platinum foil. This has substantially enhanced the interference fringe pattern intensity and permitted preliminary testing of a dense alumina. Satisfactory elastic modulus and fracture toughness values were obtained for a notched three point bend specimen.

Status of Milestones

Difficulty in obtaining commercial materials has delayed the initiation of the extensive testing of those materials. However, the necessary (LISG) modifications probably would have caused similar delays. With the exception of this brief delay, other aspects are on schedule.

Communications/Visits/Travel

During the early portion of this report period, Mr. Michael Jenkins a graduate research assistant visited the laboratory of Dr. W. N. Sharpe at John Hopkins to become familiar with the LISG technique.

Problems Encountered

These have been discussed in the technical highlights section.

Publications

None during this report period.

Testing and Evaluation of Advanced Ceramics at High Temperature in Uniaxial Tension

J. Sankar and V. S. Avva (North Carolina A&T State University)

Objectives/Scope

The purpose of this effort will be to test and evaluate advanced ceramic materials at temperatures up to 1500°C in uniaxial tension. Testing may include fast fracture strength, stepped static fatigue strength, and cyclic fatigue strength, along with analysis of fracture surfaces by scanning electron microscopy. This effort will comprise the following tasks:

Task 1. Specifications for Testing Machine and Controls + (Procurement)
Task 2. Identification of Test Material (s) + (Procurement of Specimens)
Task 3. Identification of Test Specimen Configuration
Task 4. Specifications for Testing Grips and Extensometer + (Procurement)
Task 5. Specifications for Testing Furnance and Controls + (Procurement)
Task 6. Development of Test Plan
Task 7. High Temperature Tensile Testing
Task 8. Reporting (Periodic)
Task 9. Final Report

It is anticipated that this two (2) year program will help in understanding the behavior of ceramic materials at very high temperatures in uniaxial tension.

Technical Progress

During the past six (6) months attentions were given simultaneously to all Tasks 1-5 with special attentions to Tasks 1 and 2. Various testing machines were reviewed during the reporting period and a mechanical testing equipment that will be ideal for tensile testing of ceramic has been selected. The selected machine seems to have the expected alignment, stiffness and stability required for the uniaxial tension tests of ceramics. The force transducer used in this system seems to be very accurate and the control system seems to be a superior one. A detailed description of this equipment has been sent to ONRL project manager for his approval.

As far as Task 2 is concerned, silicon nitride (Si_3N_4) is selected as the candidate material for this program.

Although the choice is wide open between both silicon carbide (SiC) and silicon nitride (Si_3N_4), the silicon nitride is selected basically to go along with the decision taken by the International Energy Agency (IEA) for their research programs. By selecting the same candidate (GTE -

Si_3N_4) as that of the IEA, the results of the various programs can be compared for better understanding of the material and a comprehensive picture can be obtained. A request for the approval of this material is already with ORNL project manager.

Various specimen configuration (Task 3) and testing grips (Task 4) used by the previous investigators are also under review. The aim is to find a specimen configuration and gripping mechanism allowing minimal cost, minimum machining, simplicity and ease of alignment.

Status of Milestone

Both Tasks 1 and 2 are complete as scheduled and are waiting for the project manager's approval.

The procurement of the testing machine and control will start after hearing from the project manager. The procurement of the Si_3N_4 specimens will not start until after identification of the specimen configuration. Since specimen geometry will influence the gripping mechanism and vice versa, attention is given to both of them simultaneously. Both high temperature extensometry and furnace specifications are also under review. Although all these tasks are moving as planned, it is projected that there may be slight delay in coming up with the proper combination of all these items, suitable for tensile testing of ceramics.

3.5 NONDESTRUCTIVE EVALUATION DEVELOPMENT

3.5.1 Nondestructive Evaluation Development

Nondestructive Characterization
R. W. McClung (Oak Ridge National Laboratory)

Objective/scope

The purpose of this program is to conduct nondestructive evaluation (NDE) development directed at identifying approaches for quantitative determination of conditions (including both properties and flaws) in ceramics that affect the structural performance. Those materials that have been seriously considered for application in advanced heat engines are all brittle materials whose fracture is affected by structural features whose dimensions are on the order of the dimensions of their microstructure. This work seeks to characterize those features using high-frequency ultrasonics and radiography to detect, size, and locate critical flaws and to measure nondestructively the elastic properties of the host material.

Technical progress

In order to determine nondestructively the presence of critical and subcritical flaws in structural ceramics and assess their impact on such parameters as fracture toughness and strength, it is necessary to probe the interior of the sample with ultrasonic waves of considerably higher frequency than are normally used in structural metals. This is because of the higher wave velocity and much smaller critical flaw size in ceramics. For example, in silicon nitride (compressional wave velocity ~10.4 $km \cdot s^{-1}$) the flaws of interest probably lie in the range 25 to 100 μm. If an average diameter of 50 μm is assumed, then the scattering transition from Rayleigh to stochastic scattering, which is roughly the point of maximum scattering from such flaws, can be calculated from theory to occur at about 66 MHz. Below this frequency, the scattering decreases with the fourth power of the frequency and is insensitive to flaw shape. For these reasons, hardware capable of operating above 50 MHz is a necessity in studying the effect of flaw size and concentration on the mechanical properties of ceramics.

We have assembled an ultrasonic system able to generate and detect elastic waves in the frequency range 1 to 100 MHz. Figure 1 shows the response of the equipment using a special-order 100-MHz transducer. Defining the bandwidth by the −6 dB points, this unit is seen to be usable in the region from 45 to 100 MHz (lower frequencies may be obtained simply by changing transducers). This spectrum may be thought of as the input signal to the specimen, which then modifies the response through scattering losses, intrinsic absorption, etc. The spectra of Fig. 1 and those to be shown below have not been corrected for nonspecimen losses (chiefly diffraction). They are also normalized to the amplitude at the peak frequency and do not reflect absolute losses, although this information is contained in the raw data.

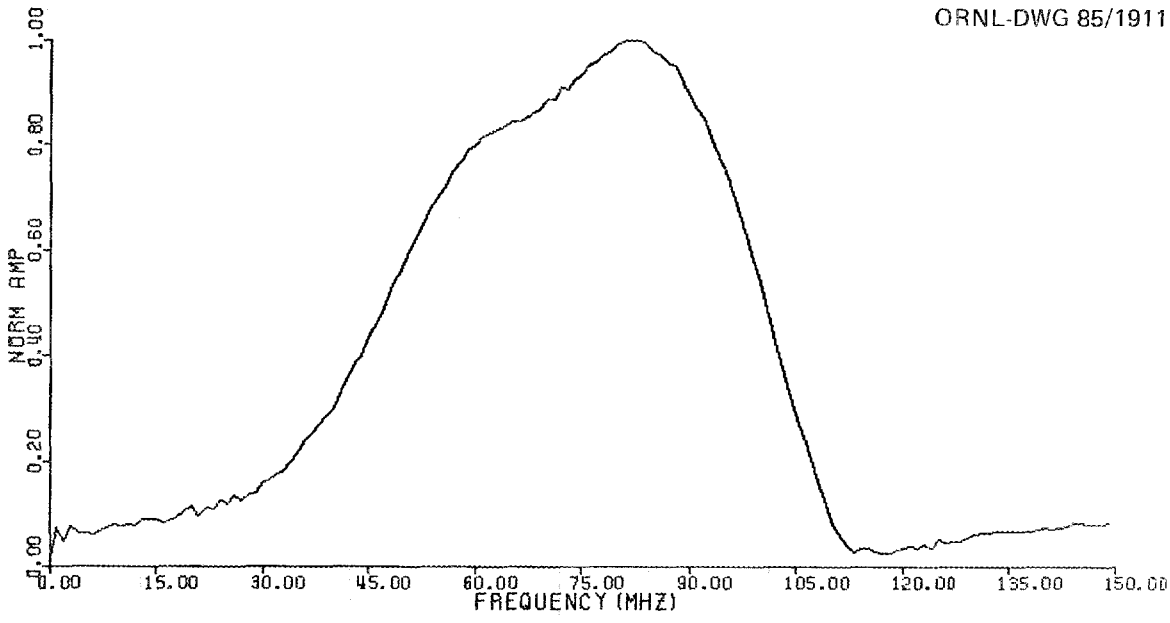

Fig. 1. Spectral response of a 100-MHz broad-band ultrasonic transducer.

Figure 2 shows the spectrum of an ultrasonic wave which has propagated through a silicon nitride modulus of rupture (MOR) bar. Note that there is relatively less high-frequency content and relatively more low-frequency content than for Fig. 1. This is consistent with frequency-dependent scattering losses, which preferentially remove the higher frequencies. The differences between these spectra contain information about the average scattering center size and concentration.

Figure 3 shows the result obtained after propagation through a zirconia MOR bar. Note that virtually none of the energy above about 70 MHz has survived. In addition, the total energy transmitted is much less than for silicon nitride.

These results can be quantified by removal (via deconvolution) of the transducer characteristic response and by correcting for diffraction effects, calculations which we routinely apply to low-frequency attenuation measurements. In the present case, however, a suitable high-frequency buffer material will have to be obtained to ensure operation in the radiation far field of the transducer for the highest frequencies present.

In order to detect the presence of critical flaws in structural ceramic materials, some form of volumetric inspection will be necessary. We currently have an automated system capable of performing such an inspection with a scan resolution of 25 μm, although the maximum frequency obtainable is limited to about 25 MHz with the present equipment. Nevertheless, five zirconia MOR bars (excess specimens from an external source

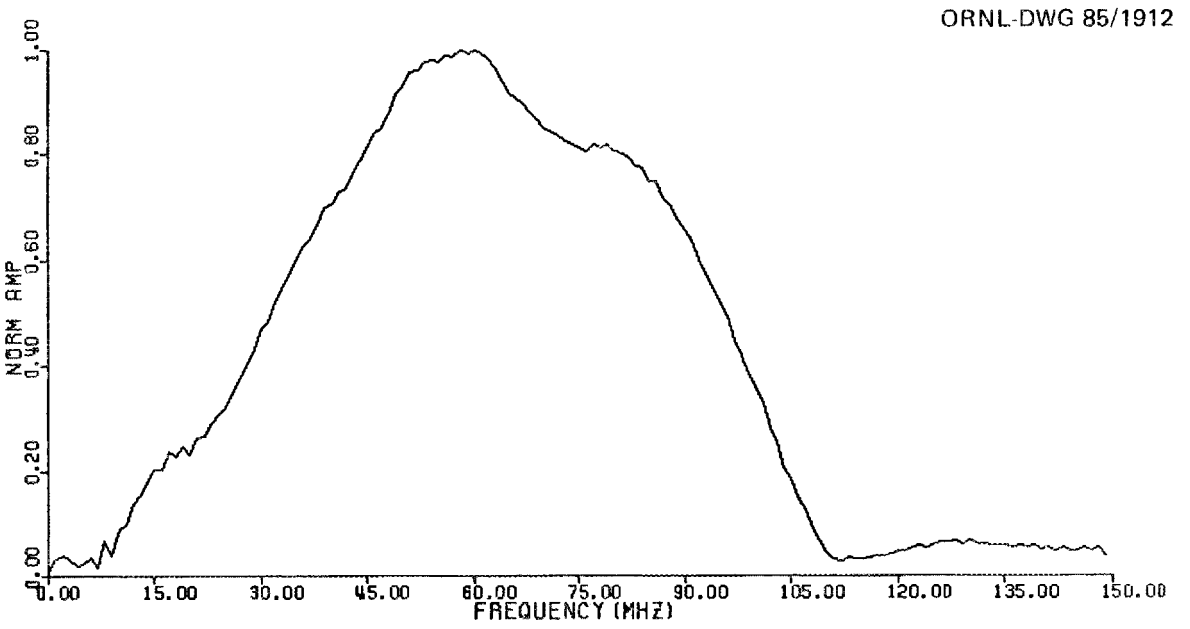

Fig. 2. Response of a silicon nitride MOR specimen to 100-MHz broad-band ultrasonic excitation.

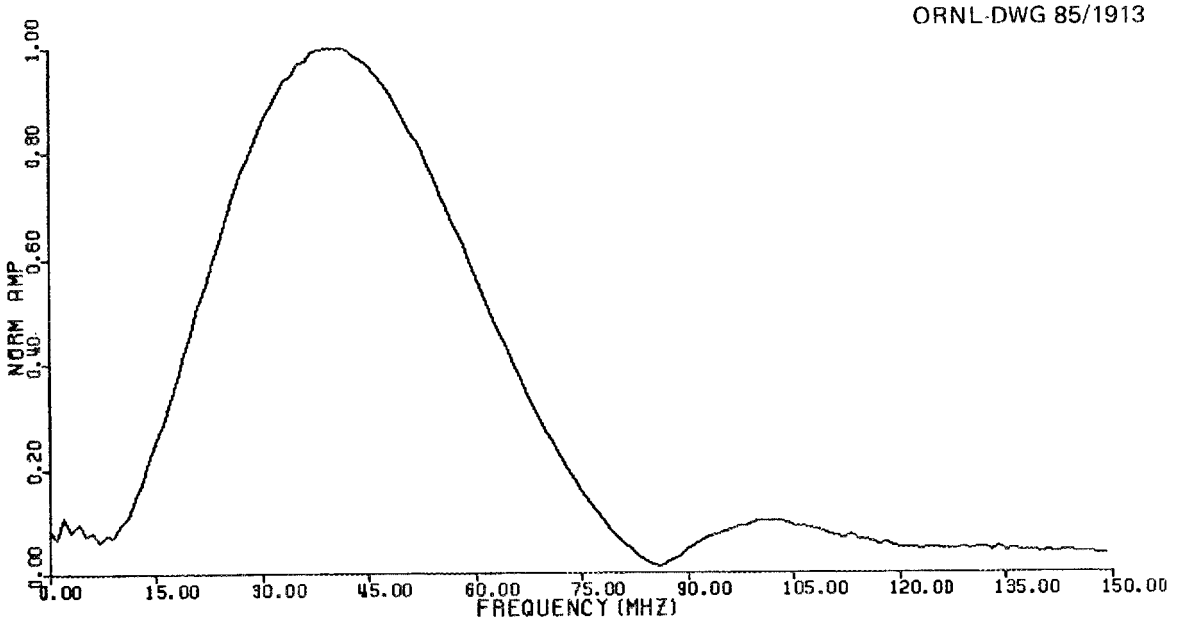

Fig. 3. Response of a zirconia MOR specimen to 100-MHz broad-band ultrasonic excitation.

being used for NDT development) were scanned by using a 20-MHz focused transducer. Several indications, some of which correspond in amplitude to the signal from a 250-μm standard flaw in zirconia, were recorded. Figure 4 shows the results, where the bars were staggered to aid delineation of the samples. These indications were quite repeatable, and numerous smaller indications were detected which were too small to record reliably. It is unlikely that the presence of such large discontinuities in these samples can be considered innocuous.

ORNL-DWG 85/1914

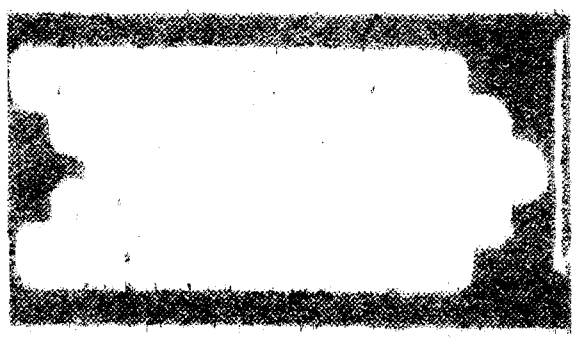

Fig. 4. Scan of zirconia MOR bars showing ultrasonic indications.

Because the data of Fig. 4 were produced by recording only those signals which exceeded a certain threshold, the dynamic range of the display is rather restricted, and the amplitude resolution is probably of the order of 1 to 2 dB. To alleviate these difficulties, a digital interface to the scanner and a gray scale software package were added to the system. With these modifications, a dynamic range of 48 dB is available, and any subset of the pixel values may be spread over the entire dynamic range to yield an amplitude resolution of about 0.1 dB. Because of hardware limitations, however, for reasonable scan rates this system is limited to about 20 MHz. Accordingly, a 100-MHz gated peak detector has been ordered that should allow us to record signals far smaller than is now possible. We are able to detect very small discontinuities (at this stage we cannot assign a size) with our current equipment, but the recording system cannot respond to signals above about 20 MHz at reasonable scanning rates. The new equipment should allow recording of signals from voids of diameters 20 to 50 μm.

Of critical interest in the ultrasonic testing of ceramics is the behavior of the material attenuation as a function of frequency. For such materials the primary loss is that due to scattering from voids, inclusions, and grain boundaries and is strongly frequency-dependent. For example, Fig. 5 shows the calculated scattering cross section for spherical voids in a silicon nitride host medium. Here k is the wave

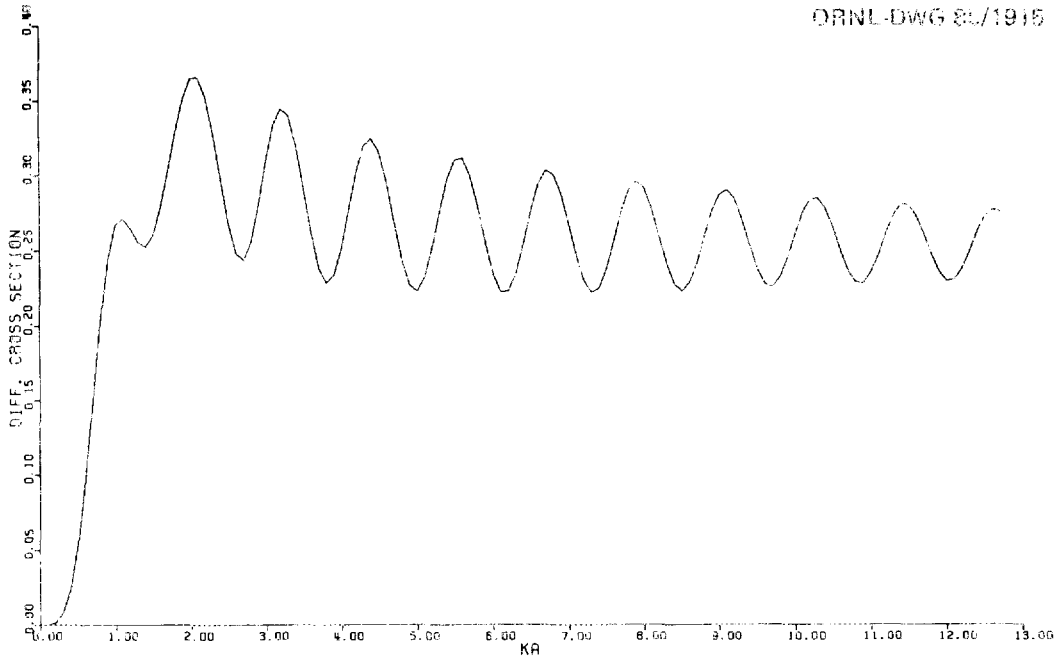

Fig. 5. Differential scattering cross section as a function of frequency for voids in silicon nitride. K is the wave number and A is the radius of the scattering center.

vector ($= 2\pi/\lambda$) of the ultrasonic radiation and a is the radius of the scatterer. The scattering is characterized by a low-frequency region (Rayleigh regime) below $ka \sim 1$ where the scattering increases with the fourth power of the frequency and a high-frequency region where the differential scattering cross section is oscillatory. These oscillations are caused by interference between the direct wave scattered by the void and a "creeping wave," which propagates around the surface of the void. Since the velocity in the host medium is known, the periodicity of these oscillations can be used to determine the diameter of the scattering centers, assuming uniformity of size. In many practical cases, however, the creeping wave is either greatly attenuated or missing. In this case the oscillations of Fig. 5 are replaced by an average value, and the transition frequency at $ka \sim 1$ may be used to estimate the size of the scattering center.

When the scattering centers are not uniform in size, the situation becomes more complicated. In the Rayleigh regime, the scattering varies as the sixth power of the scatterer diameter, while in the high-frequency regime it varies inversely with diameter. Thus, in principle, one can at least garner information about the extremes of the size distribution from the scattering behavior.

We have also calculated the scattering from spherical inclusions instead of voids, but the results were found to be highly sensitive to the elastic properties of both the host and the inclusion. The high-frequency results were exceedingly complex because of the generation of additional waves within the body of the inclusion, but the curves still exhibited the characteristic monotonic decay below $ka \sim 1$. The Rayleigh transition knee thus appears to be the most definitive and reliable characteristic of the scattering.

The results presented above will be obscured by the characteristic response of the transducer and by physical factors, e.g., radiation beam spread, that are unrelated to the sample. These effects can be removed, assuming that the transducer characteristics are known, by computer processing. In making the corrections, however, we find that the data still exhibit fluctuations that appear similar to the near-field (Fresnel zone) fluctuations of the transducer radiation field. To address this problem, we are writing a computer program to evaluate the transducer radiation field numerically rather than relying on the closed-form solution presently used. This should indicate whether the problem resides in our diffraction correction computer codes or is related to the specimen in some way.

4.0 TECHNOLOGY TRANSFER

4.1 TECHNOLOGY TRANSFER

D. R. Johnson
Oak Ridge National Laboratory

A trade-show-quality portable display for the project has been completed. It was used at the Automotive Technology Development Contractor's Coordination Meeting, October 29—November 2, 1984, Dearborn, Michigan, and at the ASME Gas Turbine Conference and Exhibit, March 17—21, 1985, Houston, Texas. A photograph of the exhibit is shown in Fig. 1. The exhibit consists of two light box displays that describe the scope of the project. A rear-projection slide show unit includes both a continuous 20-slide overview presentation and a random-access projector with an 80-slide set that can be used for detailed discussion of any task in the project. A lighted display box encloses a set of various ceramic engine parts loaned to us by numerous U.S. companies. An architect's model of the High Temperature Materials Laboratory completes the display. The purpose of the exhibit is to make the Ceramic Technology Project known to as many potential participants as possible. We plan to use the exhibit next at the Annual Meeting of the American Ceramic Society in Cincinnati, Ohio, in May 1985.

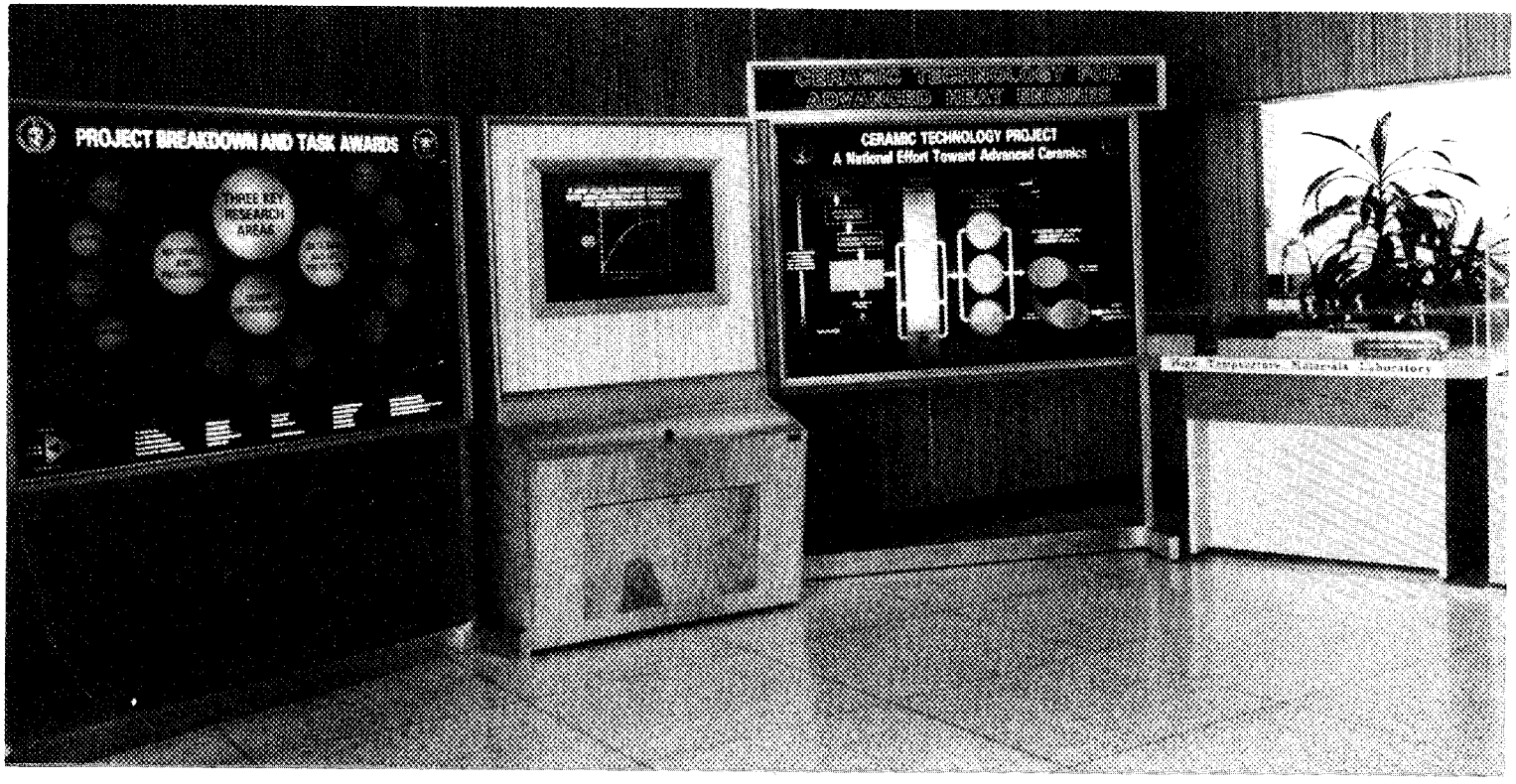

Fig. 1. Portable display for the Ceramic Technology for Advanced Heat Engines Project.

INTERNAL DISTRIBUTION

1-2. Central Research Library
3. Document Reference Section
4-5. Laboratory Records Department
6. Laboratory Records, ORNL RC
7. ORNL Patent Section
8. S. Baik
9. P. F. Becher
10. J. Bentley
11. A. Bleier
12. K. W. Boling
13. W. D. Bond
14. R. A. Bradley
15. C. R. Brinkman
16. A. J. Caputo
17. R. S. Carlsmith
18. P. T. Carlson
19. J. A. Carpenter
20. G. W. Clark
21. S. A. David
22. W. P. Eatherly
23. J. I. Federer
24. W. Fulkerson
25. R. L. Graves
26. D. L. Greene
27. M. P. Guthrie
28. M. A. Janney
29-33. D. R. Johnson
34. R. R. Judkins
35. M. A. Karnitz
36. K. C. Liu
37. E. L. Long, Jr.
38. R. W. McClung
39. J. W. Michel
40. A. J. Moorhead
41. C. R. Richmond
42. J M Robbins
43. M. W. Rosenthal
44-93. A. C. Schaffhauser
94. J. H. Schneibel
95. J. L. Scott
96. G. M. Slaughter
97. J. O. Stiegler
98. D. P. Stinton
99. R. W. Swindeman
100. V. J. Tennery
101-103. P. T. Thornton
104. T. N. Tiegs
105. J. R. Weir, Jr.
106. F. W. Wiffen
107. C. S. Yust
108. A. Zucker
109. R. J. Charles (Consultant)
110. G. Y. Chin (Consultant)
111. H. F. Cook (Consultant)
112. Alan Lawley (Consultant)
113. W. D. Nix (Consultant)
114. J. C. Williams (Consultant)

EXTERNAL DISTRIBUTION

115. Donald F. Adams
Composite Materials Research Group
Mechanical Engineering Department
University of Wyoming
Laramie, WY 82071

116. Anil K. Agarwal
Product Manager
High Performance Ceramics
Norton Company
One New Bond Street
Worcester, MA 01606

117. Richard T. Alpaugh
Department of Energy
Office of Transportation Systems
CE-131 FORSTL
1000 Independence Aven
Washington, DC 20585

118. James P. Arnold
U.S. Army Belvoir
R&D Center
ATTN: FTRBE-EMP
Fort Belvoir, VA 22060

119. V. S. Avva
Dept. of Mechanical Engineering
North Carolina Agricultural and Technical State University
Greensboro, NC 27411

120. John M. Bailey
Research Consultant, Research Dept.
Technical Center
Caterpillar Tractor Co.
100 NE Adams
Peoria, IL 61629

121. Murray Bailey
NASA Lewis Research Center
21000 Brookpark Road, MS 77-6
Cleveland, OH 44135

122. J. Gary Baldoni
GTE Laboratories, Inc.
40 Sylvan Road
Waltham, MA 02254

123. R. R. Baker
34819 Lyndon Street
Livonia, MI 48154

124. Ken Baumert
Air Products and Chemicals, Inc.
Box 538
Allentown, PA 18105

125. Ronald L. Beatty
ARCO Chemicals, Silag Operation
Route 6, Box A
Greer, SC 29651

126. A. L. Bement, Jr., Vice President
Technical Resources
TRW, Inc.
23555 Euclid Avenue
Cleveland, OH 44117

127. Clifton G. Bergeron, Head
Department of Ceramic Engineering
204 Ceramics Building
University of Illinois
Urbana, IL 61801

128. William D. Bjorndahl
TRW, Inc.
TRW Energy Development Group
Materials Characterization and Chemical Analysis Dept.
One Space Park
Building 01, Room 2060
Redondo Beach, CA 90278

129. Paul N. Blumberg
President
Intgegral Technologies Inc.
415 E. Plaza Drive
Westmont, IL 60559

130. Wolfgang D. G. Boecker
SOHIO Engineered Materials Co.
Niagara Falls R&D Center
PO Box 832
Niagara Falls, NY 14302

131. Seymour A. Bortz
Manager, Nonmetallic Materials and Composites
Materials and Manufacturing Technology
IIT Research Institute
10 West 35th Street
Chicago, IL 60616

132. H. K. Bowen
Department of Materials Science and Engineering, Room 12-009
Massachusetts Institute of Technology
Cambridge, MA 02139

133. Richard C. Bradt
University of Washington
Roberts Hall
FB-10
Seattle, WA 98195

134. Raymond J. Bratton
Manager, Ceramic Science
Westinghouse Research and Development Center
1310 Beulah Road
Pittsburgh, PA 15235

135. W. Bryzik
US Army Tank Automotive Command (TACOM)
R&D Center
Warren, MI 48090

136. S. T. Buljan
GTE Laboratories, Inc.
40 Sylvan Road
Waltham, MA 02154

137. Donald J. Campbell
Air Force Wright Aeronautical Laboratory
AFWAL/POX
Wright-Patterson AFB, OH 45433

138. Harry W. Carpenter
Rockwell International
Rocketdyne Division
J39-169:HC92
6633 Canoga Avenue
Canoga Park, CA 91304

139. David Carruthers
Garrett Turbine Engine Company
111 South 34 Street
PO Box 5217
Phoenix, AZ 85010

140. Se-Tak Chang
GTE Laboratories
40 Sylvan Road
Dept. 312
Waltham, MA 02254

141. Albert A. Chesnes
Director
Heat Engine Propulsion Division
Office of Transportation Systems
Department of Energy
CE-131 FORSTL
1000 Independence Avenue
Washington, DC 20585

142. Melvin H. Chiogioji
Director
Office of Transportation Systems
Department of Energy
CE-13 FORSTL
1000 Independence Avenue, SW
Washington, DC 20585

143. William L. Cleary
Associate Division Director
ORI, Inc.
1375 Piccard Drive
Rockville, MD 20850

144. Philip R. Compton
Energy Systems Office
National Aeronautics and
Space Administration
Code REC-1
Washington, DC 20546

145. John A. Coppola
Representative Director
Executive Vice President
Hitachi-Carborundum Company
Shinjuku-Mitsui Building
No. 1-1, 2-Chome, Nishishinjuku
Shinjuku-ku, Tokyo 160, JAPAN

146. C. H. Craig
Department of Energy
1000 Independence Avenue
CE-131 FORSTL
Washington, DC 20585

147. William J. Croft
Army Materials and Mechanics
Research Center (AMMRC)
Arsenal Street
Watertown, MA 02172

148. Gary M. Crosbie
Ford Motor Company
PO Box 2053, Room S-2079
Ceramics Materials Department
Dearborn, MI 48121

149. Floyd W. Crouse, Jr.
Department of Energy
Morgantown Energy Technology Center
PO Box 880
Morgantown, WV 26505

150. Raymond Cutler
Ceramatec, Inc.
163 West 1700 South
Salt Lake City, UT 84115

151. Stanley J. Dapkunas
Office of Technical Coordination
Fossil Energy Technical
Coordination Staff
FE-14, MS B127 GTN
Department of Energy
Washington, DC 20545

152. Robert F. Davis
North Carolina State University
Materials Engineering Department
232 Riddick Laboratory
Raleigh, NC 27607

153. Alan L. Dragoo
Materials Scientist, Inorganic
Materials Division
National Bureau of Standards
Center for Materials Science
Gaithersburg, MD 20899

154. Keith F. Dufrane
Battelle Columbus Laboratories
505 King Avenue
Columbus, OH 43201

155. Robert J. Eagan
Manager, Chemistry and Ceramics Department 1840
Sandia National Laboratories
Albuquerque, NM 87185

156. Christopher A. Ebel
Program Manager
Norton Company
High Performance Ceramics
1 New Bond Street
Worchester, MA 01606

157. J. J. Eberhardt
Office of Energy Utilization Research
Department of Energy
CE-142 FORSTL
1000 Independence Avenue
Washington, DC 20585

158. E. E. Ecklund
Office of Transportation Systems
Department of Energy
CE-131 FORSTL
1000 Independence Avenue
Washington, DC 20585

159. William A. Ellingson
Argonne National Laboratory
9700 South Cass Avenue
Argonne, IL 60439

160. Director, Applied Technology Laboratory
U.S. Army Research and Technology Laboratory (AVSCOM)
ATTN: SAVDL-ATL-ATP
(Graydon A. Elliott)
Fort Eustis, VA 23604

161. A. Erdely
Chemical Engineer
26 Av. Gare Des Eaux-vives
1208 Geneva, SWITZERLAND

162. Charles D. Estes
U.S. Senate
Professional Staff Member
Committee on Appropriations
Room SD-152 Dirksen Senate Office Building
Washington, DC 20510

163. Anthony G. Evans
Lawrence Berkeley Laboratory
University of California
264 Hearst Mining Building
Berkeley, CA 94720

164. Robert C. Evans, Asst. Manager
Vehicular Gas Turbine and Diesel Project Office
NASA-Lewis Research Center
21000 Brookpark Road
Cleveland, OH 44135

165. John Facey
National Aeronautics and Space Administration
Energy Systems Office
Washington, DC 20546

166. John W. Fairbanks
Office of Advanced Energy Conversion
Department of Energy
FE-22 GTN
Washington, DC 20545

167. Larry Farrell
Babcock and Wilcox
PO Box 1260
Lynchburg, VA 24505

168. Matthew K. Ferber
University of Illinois-Urbana
203 Ceramic Building
105 S. Goodwin Avenue
Urbana, IL 61801

169. R. E. Fisher
President
Amercom, Inc.
8948 Fullbright Avenue
Chatsworth, CA 91311

170. H. W. Foglesong
Dow Corning Corporation
3901 S. Saginaw Road
Midland, MI 48640

171. Robert G. Frank
Manager, Non-Metallic Materials
General Electric Company
One Neumann Way, Mail Drop M-87
PO Box 156301
Cincinnati, OH 45215-6301

172. Frank Gac
Department of Materials Science
and Engineering
University of Washington
Seattle, WA 98195

173. George E. Gazza
AMMRC, Ceramic Research Division
AMXMR-MT
Arsenal Street
Watertown, MA 02172

174. Paul Glance
Director, R&D
Concept Analysis Corporation
9145 General Court
Plymouth, MI 48170

175. Joseph W. Glatz
Naval Air Propulsion Center
Science and Technology Group
Systems Technology Division
Box 7176, PE 34
Trenton, NJ 08628

176. S. Goguen
Office of Transportation Systems
Department of Energy
CE-131 FORSTL
1000 Independence Avenue
Washington, DC 20585

177. Stephen T. Gonczy
Signal UOP Research Center
Materials Science Department
50 UOP Plaza
Des Plaines, IL 60016-6187

178. Robert J. Gottschall
Office of Material Sciences
Department of Energy
ER-131 GTN
Washington, DC 20545

179. Kenneth Green
Senior Development Engineer
Coors Porcelain Company
Golden, CO 80401

180. Michael Greenfield
National Aeronautics and
Space Administration
Energy Systems Office
Washington, DC 20546

181. L. E. Groseclose
General Motors Corporation
Allison Gas Turbine Division
P.O. Box 420
Indianapolis, IN 46206-0420

182. T. D. Gulden, Manager
Ceramics and Chemistry
GA Technologies, Inc.
PO Box 81608
San Diego, CA 92138

183. M. D. Gurney
NIPER
PO Box 2128
Bartlesville, OK 74005

184. H. T. Hahn
Mechanical Engineering Department
Washington University
at St. Louis
Lindell and Skinker
Box 1087
St. Louis, MO 63130

185. Nabil S. Hakim
Staff Research Engineer
Engineering R&D
General Motors Corporation
Detroit Diesel Allison Division
36880 Ecorse Road
Romulus, MI 48174

186. John M. Halstead
Manager, Business Development
Structural Ceramics Division
SOHIO Engineered Materials Company
PO Box 1054
AiResearch Manufacturing Company
2525 West 190th Street
Torrance, CA 90509

187. R. A. Harmon
25 Schalren Drive
Latham, NY 12110

188. Stephen D. Hartline
Norton Company
One New Bond Street
Worchester, MA 01606

189. Willard E. Hauth
Section Manager - Composite
Development Ceramics Program
Dow Corning Corporation
Midland, MI 48640

190. Norman L. Hecht
University of Dayton Research Institute
300 College Park
Dayton, OH 45469-0001

191. S. S. Hecker, Chairman
Center for Materials Science
Los Alamos National Laboratory
Mail Stop K765
Los Alamos, NM 87545

192. Peter W. Heitman
General Motors Corporation
Allison Gas Turbine Operations
PO Box 420, W-5
Indianapolis, IN 46206-0420

193. H. E. Helms
General Motors Corporation
Allison Gas Turbine Operations
PO Box 420
Indianapolis, IN 46206-0420

194. Thomas L. Henson, Director of Research and Engineering
Chemical & Metallurgical Division
GTE Products Corporation
Hawes Street
Towanda, PA 18848-0504

195. Thomas P. Herbell
NASA Lewis Research Center
21000 Brookpark Road
M/S 49-3
Cleveland, OH 44135

196. Robert V. Hillery, Manager
Coating Materials & Processes
General Electric Company
Cincinnati, OH 45215

197. Jonathan W. Hinton
Vice President and General Manager
Structural Ceramics Division
SOHIO Engineered Materials Company
PO Box 1054
Niagara Falls, NY 14302

198. Stephen M. Hsu
Inorganic Materials Div.
Center for Materials Science
U.S. Department of Commerce
National Bureau of Standards
Gaithersburg, MD 20899

199. Joseph E. Hunter, Jr.
Metallurgy Department
General Motors Research Lab.
12 Mile and Mound Road
Warren, MI 48090-9055

200. Louis C. Ianniello, Director
Office of Materials Sciences
Department of Energy
ER-13 GTN
Washington, DC 20545

201. Curtis A. Johnson
General Electric Company
Ceramics Branch
PO Box 8
Schenectady, NY 12301

202. Larry Johnson, Director
Center for Transportation Research
Argonne National Laboratory
Building 362
9700 S. Cass Avenue
Argonne, IL 60439

203. R. A. Johnson
General Motors Corporation
Allison Gas Turbine Division
P.O. Box 420
Indianapolis, IN 46206-0420

204. L. A. Joo
Associate Director of Research
Great Lakes Research Corp.
P.O. Box 1031
Elizabethton, TN 37643

205. Roy Kamo, President
Adiabatics, Inc.
630 S. Mapleton
Columbus, IN 47201

206. Allan Katz
Air Force Wright Aeronautical Laboratory
Materials Laboratory
Metals and Ceramics Division
AFWAL/MLLM
Wright-Patterson AFB, OH 45433

207. R. N. Katz
Chief, Ceramics Research Division
DRXMR-MC
Army Materials and Mechanics Research Center (AMMRC)
Arsenal Street
Watertown, MA 02172

208. P. Victor Kelsey
Ceramics Technical Leader
Materials Science Division
Alcoa Aluminum Company
of America
Alcoa Technical Center B
Alcoa Center, PA 15061

209. Frederick L. Kennard, III
Supervisor, Ceramic Research
AC Spark Plug Division of
General Motors
1300 N. Dort Highway
Flint, MI 48556

210. J. R. Kidwell
AGT 101 Assistant Project Engineer
Garrett Turbine Engine Company
111 S. 34th Street
P.O. Box 5217
Phoenix, AZ 85010

211. A. S. Kobayashi
Mechanical Engineering Dept.
MS FU10
University of Washington
Seattle, WA 98195

212. David M. Kotchick
AiResearch Manufacturing Company
2525 W. 190th Street
Torrance, CA 90509

213. Saunders B. Kramer
Manager, AGT Program
Office of Transportation Systems
Department of Energy
CE-131 FORSTL
1000 Independence Avenue
Washington, DC 20585

214. D. M. Kreiner
AGT 101 Project Manager
Garrett Turbine Engine Company
111 S. 34th Street
P.O. Box 5217
Phoenix, AZ 85010

215. Everett A. Lake
Air Force Wright Aeronautical
Laboratory
AFWAL/POOS
Wright-Patterson AFB, OH 45433

216. Fred F. Lange
Science Center
Rockwell International
1049 Camino Dos Rios
PO Box 1085
Thousand Oaks, CA 91360

217. John G. Lanning
Corning Glass Works
Advanced Engine Components
HP-BB-2
Corning, NY 14830

218. David C. Larsen
IIT Research Center
10 W. 35th Street
Chicago, IL 60616

219. E. M. Lenoe
Army Materials and Mechanics
Research Center
DRXMR-MC
Department of the Army
Arsenal Street
Watertown, MA 02172

220. Stanley R. Levine
NASA-Lewis Research Center
21000 Brookpark Road
Cleveland, OH 44135

221. David Lewis
Naval Research Laboratory
Code 6360, Materials Science &
Technology Division
4555 Overlook Avenue, S.W.
Washington, DC 20375

222. Winston W. Liang
Project Manager
Industrial Materials Research
Gas Research Institute
8600 W. Bryn Mawr Avenue
Chicago, IL 60631

223. Bill Long
Babcock and Wilcox
PO Box 1260
Lynchburg, VA 24505

224. L. A. Lott
EG&G, Inc.
Idaho National Engineering
Laboratory
PO Box 1625
Idaho Falls, ID 83415

225. Bryan K. Luftglass
Staff Consultant
Chem Systems, Inc.
303 S. Broadway
Tarrytown, NY 10591

226. Tai-il Mah
Technical Manager
Ceramics and Composites Research
Universal Energy Systems
4401 Dayton-Xenia Road
Dayton, OH 45432

227. John Mason
Vice President-Engineering
The Garrett Corporation
9851 Sepulveda Boulevard
PO Box 92248
Los Angeles, CA 90009

228. K. S. Mazdiyasni
Air Force Wright Aeronautical Laboratory
Materials Laboratory
Metals and Ceramics Division
AFWAL/MLLM
Wright-Patterson AFB, OH 45433

229. J. McCauley
Army Materials and Mechanics Research Center
DRXMR-MC
Department of the Army
Arsenal Street
Watertown, MA 02171

230. Thomas D. McGee
Department of Materials Science and Engineering
Iowa State University
Ames, IA 50011

231. Malcolm G. McLaren
Head, Department of Ceramics
Rutgers University
Busch Campus
Box 909, Bowser Road
Piscataway, NJ 08854

232. Arthur F. McLean
Ceramics Materials Department
Ford Motor Company
PO Box 2053
Dearborn, MI 48121

233. Brian L. Mehosky
Development Engineer
SOHIO
Research and Development
4440 Warrensville Ctr. Rd.
Cleveland, OH 44128

234. P. K. Mehrotra
Kennametal Inc.
P.O. Box 639
Greensburg, PA 15601

235. Donald Messier
Army Materials and Mechanics Research Center
DRXMR-MC
Department of the Army
Arsenal Street
Watertown, MA 02171

236. Arthur G. Metcalfe
Director, Research Department
Solar Turbines, Inc.
PO Box 80966
2200 Pacific Highway
San Diego, CA 92138

237. W. Miloscia
SOHIO
Research and Development
4440 Warrensville Ctr. Rd.
Cleveland, OH 44128

238. Helen Moeller
Babcock & Wilcox
P.O. Box 1260
Lynchburg, VA 24505

239. Peter E. D. Morgan
Member Technical Staff
Structural Ceramics
Science Center
Rockwell International
1049 Camino Dos Rios
PO Box 1085
Thousand Oaks, CA 91360

240. James I. Mueller
Ceramic Engineering Dept.
MS FB10
University of Washington
Seattle, WA 98195

241. Solomon Musikant
General Electric, VFSC
Building 100, U-3027
PO Box 8555
Philadelphia, PA 19101

242. Dale E. Niesz
Manager, Materials Department
Battelle Columbus Laboratories
505 King Avenue
Columbus, OH 43201

243. W. Richard Ott
New York State College of Ceramics
Alfred University
Alfred, NY 14802

244. Hayne Palmour III
Engineering Research Services Division
2158 Burlington Engineering Laboratories
North Carolina State University
PO Box 5995
Raleigh, NC 27607

245. Joseph N. Panzarino
Norton Company
Director, Research and Development
High Performance Ceramics
1 New Bond Street
Worcester, MA 01606

246. Pellegrino Papa, Manager
Technical and Business Development
Corning Technical Products Division
Corning Glass Works
Corning, NY 14831

247. Arvid E. Pasto
Member of Technical Staff
Precision Materials Technology
GTE Laboratories, Inc.
40 Sylvan Road
Waltham, MA 02254

248. James W. Patten
Director, Materials Engineering
Cummins Engine Company, Inc.
Mail Code 50183
Box 3005
Columbus, IN 47201

249. Dan Petrak
Babcock and Wilcox
PO Box 1260
Lynchburg, VA 24505

250. R. Byron Pipes
Center for Composite Materials
2001 Spencer Laboratory
University of Delaware
Newark, DE 19716

251. Robert C. Pohanka
Office of Naval Research
Code 431
800 North Quincy Street
Arlington, VA 22217

252. Karl M. Prewo
United Technologies Research Center
Silver Lane, MS 24
East Hartford, CT 06108

253. Hubert B. Probst
Chief Scientist
Materials Division, MS 49-1
NASA-Lewis Research Center
21000 Brookpark Road
Cleveland, OH 44135

254. Carr Lane Quackenbush
GTE Products Corporation
Hawes Street
Towanda, PA 18848-0504

255. George Quinn
AMMRV, Ceramic Research Div.
AMXMR-MV
Arsenal Street
Watertown, MA 02172

256. Dennis T. Quinto
Phillip M. McKenna Laboratory
Kennametal, Incorporated
Post Office Box 639
Greensburg, PA 15601

257. Dennis Readey
Department Chairman
Ceramic Engineering Department
Ohio State University
2041 College Road
Columbus, OH 43210

258. Robert R. Reeber
U.S. Army Research Office
PO Box 12211
Research Triangle Park, NC 27709

259. K. L. Reifsnider
Department of Engineering Science and Mechanics
Virginia Polytechnic Institute and State University
Blacksburg, VA 24061

260. K. T. Rhee
College of Engineering
Rutgers University
P.O. Box 909
Piscataway, NJ 08854

261. Roy W. Rice
W. R. Grace and Company
7379 Route 32
Columbus, MD 21044

262. David W. Richerson
Ceramatec, Inc.
163 West 1700 South
Salt Lake City, UT 84115

263. Paul Rieth
Ferro Corporation
661 Willet Road
Buffalo, NY 14218

264. Michael A. Rigdon
Babcock and Wilcox
1735 I Street, NW
Washington, DC 20006

265. John E. Ritter, Jr.
University of Massachusetts
Mechanical Engineering Department
Amherst, MA 01003

266. David J. Rowcliffe
SRI International
333 Ravenswood Avenue
Menlo Park, CA 94025

267. Donald W. Roy, Manager
Carbide and Optical Material
Research and Development
Coors Porcelain Company
Golden, CO 80401

268. Bruce Rubinger
Gobal
50 Milk Street
15th Floor
Boston, MA 02109

269. Robert Ruh
Air Force Wright Aeronautical
Laboratory
Materials Laboratory
Metals and Ceramics Division
AFWAL/MLLM
Wright-Patterson AFB, OH 45433

270. Robert J. Russell, Sr.
Divisional Vice President
Technology and Planning
High Performance Ceramics
Norton Company
One New Bond Street
Worchester, MA 01606

271. J. Sankar
North Carolina Agricultural
and Technical State University
Mechanical Engineering Dept.
Greenboro, NC 27411

272. Maxine Savitz
5019 Lowell Street, NW
Washington, DC 20016

273. Richard Schapery
Civil Engineering Department
Texas A&M University
College Station, TX 77843

274. Liselotte J. Schioler
AMMRC, Ceramic Research Div.
AMXMR-MC
Arsenal Street
Watertown, MA 02172

275. Matthew Schreiner
Gas Research Institute
8600 West Bryn Mawr Avenue
Chicago, IL 60631

276. Peter C. Schultz
Manager, Materials Research
Corning Research and Development
Division
Corning Glass Works
Corning, NY 14831

277. R. B. Schulz
Office of Transportation Systems
Department of Energy
CE-131 FORSTL
1000 Independence Avenue
Washington, DC 20585

278. Murray A. Schwartz
Bureau of Mines
2401 I Street, N.W.
Washington, DC 20241

279. Thomas M. Sebestyen
U.S. Army Tank Automotive Command
AMSTA-RGRT
Warren, MI 48397-5000

280. Brian Seegmiller
Senior Development Engineer
Coors Porcelain Company
17750 North 32 Street
Golden, CO 80401

281. Peter T. B. Shaffer
Executive Vice President
Advanced Refractory
Technologies, Inc.
699 Hertel Avenue
Buffalo, NY 14207

282. Jack D. Sibold
Coors Porcelain Company
17750 North 32 Street
Golden, CO 80401

283. Neal Sigmon
Appropriations Committee
Subcommittee on Interior and Related Events
U.S. House of Representatives
B-308 Rayburn Building
Washington, DC 20515

284. Richard Silberglitt
DHR, Inc.
6849 Old Dominion Drive
Suite 228
McLean, VA 22101

285. S. R. Skaggs
MS F-682, Program Office
Los Alamos National Laboratory
PO Box 1663
Los Alamos, NM 87545

286. J. Thomas Smith, Director
Precision Materials Tech.
GTE Laboratories, Inc.
40 Sylvan Road
Waltham, MA 02254

287. Jay R. Smyth
Senior Materials Engineer
Garrett Turbine Engine Company
111 South 34th Street
Phoenix, AZ 85010

288. Rafal Sobotowski
SOHIO Research and Development
3092 Broadway Avenue
Cleveland, OH 44115

289. Richard M. Spriggs
National Materials Advisory Board
National Research Council
2101 Constitution Avenue
Washington, DC 20418

290. M. Srinivasan
Sohio Engineered Materials Company
Niagara Falls R&D Center
P. O. Box 832
Niagara Falls, NY 14302

291. Gordon L. Starr, Manager
Metallic/Ceramic Materials Dept.
Cummins Engine Company, Inc.
Mail Code 50183
Box 3005
Columbus, IN 47202-3005

292. Harold L. Stocker, Manager
Low Heat Rejection Program
General Motors Corporation
Allison Gas Turbine Operations
PO Box 420, T-23
Indianapolis, IN 46206-0420

293. Roger Storm
Director, Niagara Falls R&D Center
SOHIO Engineered Materials Company
PO Box 832
Niagara Falls, NY 14302

294. E. E. Strain
Program Manager
Garrett Turbine Engine Company
111 S. 34th Street
PO Box 5217, Mail Stop 301-2N
Phoenix, AZ 85010

295. Thomas N. Strom
NASA Lewis Research Center
21000 Brookpark Road, 77-6
Cleveland, OH 44135

296. Karsten Styhr
AiResearch Casting Co.
19800 Van Ness Avenue
Torrance, CA 90509

297. Lewis Swank
Ford Motor Company
PO Box 2053
Building SRL, Room E3172
Dearborn, MI 48121

298. Anthony C. Taylor
Staff Director
Subcommittee on Transportation, Aviation and Materials
Committee on Science and Technology
U.S. House of Representatives
Room 2321 Rayburn Building
Washington, DC 20515

299. W. H. Thielbahr
Chief, Energy Programs Branch
Idaho Operations Office
U.S. Department of Energy
550 2nd Street
Idaho Falls, ID 83401

300. John K. Tien
Director of Center for
Strategic Materials
1137 S.W. Mudd Building
Columbia University
New York, NY 10027

301. T. Y. Tien
University of Michigan
Dept. of Materials &
Metallurgical Engineering
Dow Building
Ann Arbor, MI 48109-2136

302. Nancy J. Tighe
National Bureau of Standards
Inorganic Materials Division 420
Gaithersburg, MD 20899

303. Julian M. Tishkoff
Air Force Office of
Scientific Research
Directorate of Aerospace Sciences
Bolling AFB
Washington, DC 20332

304. Maurice L. Torti
Senior Scientist
High Performance Ceramics
Norton Company
One New Bond Street
Worchester, MA 01606

305. Louis E. Toth
Division of Materials Research
National Science Foundation
1800 G Street, N.W.
Washington, DC 20550

306. Richard E. Tressler
Chairman, Ceramic Science and
Engineering Department
The Pennsylvania State University
201 Steidle Building
University Park, PA 16802

307. V. Venkateswaran
SOHIO Engineered Materials Company
P.O. Box 832
Niagara Falls, NY 14302

308. John B. Wachtman, Jr.
Rutgers University
Department of Ceramics
PO Box 901
Piscataway, NJ 08854

309. Richard B. Wallace
Manager, Government Research
and Development Programs
General Motors Corporation
Detroit Diesel Allison Division
36880 Ecorse Road
Romulus, MI 48174

310. Harlan L. Watson
Subcommittee on Energy Research
and Production
U.S. House of Representatives
Committee on Science and
Technology
Suite 2321, Rayburn House
Office Building
Washington, DC 20515

311. Steven G. Wax
Materials Science Division
Advanced Research Projects Agency
Department of Defense
1400 Wilson Boulevard
Arlington, VA 22209

312. Albert R. C. Westwood
Corporate Director
Martin Marietta Laboratories
1450 South Rolling Road
Baltimore, MD 21227

313. Sheldon M. Wiederhorn
Inorganic Materials Division
Mechanical Properties Group
U.S. Department of Commerce
National Bureau of Standards
Gaithersburg, MD 20899

314. Roger R. Wills, Manager
Advanced Ceramic Components
TRW Inc.
Automotive Worldwide Sector
Valve Division
1455 East 185th Street
Cleveland, OH 44110

315. David Gordon Wilson
Massachusetts Institute of
Technology
Mechanical Engineering Department
Room 3-455
Cambridge, MA 02139

316. J. M. Wimmer, Supervisor
Nonmetallic Materials Group
Garrett Turbine Engine Company
111 S. 34th Street
P.O. Box 5217
Phoenix, AZ 85010

317. David Wirth, Vice President
Technical Operations and Engr.
Coors Porcelain Company
17750 North 32 Street
Golden, CO 80401

318. Thomas J. Wissing
Manager, Government
Contract Administration
Eaton Corporation
Engineering & Research Center
26201 Northwestern Highway
PO Box 766
Southfield, MI 48037

319. James C. Wood
NASA Lewis Research Center
21000 Brookpark Road
Mail Stop 77-6
Cleveland, OH 44135

320. Hun C. Yeh
Ceramic Supervisor
AiResearch Casting Company
A Division of the Garrett Corp.
19800 Van Ness Avenue
Torrance, CA 90509

321. Thomas M. Yonushonis
Cummins Engine Company
Box 3005, Mail Code 50183
Columbus, IN 47202-3005

322. Don Zabierek
Air Force Wright Aeronautical
Laboratory
AFWAL/POTC
Wright-Patterson AFB, OH 45433

323. Klaus M. Zwilsky
Executive Director
National Materials Advisory Board
National Research Council
2101 Constitution Avenue
Washington, DC 20418

324. Department of Energy
Oak Ridge Operations Office
Office of Assistant Manager for
Energy Research and Development
PO Box E
Oak Ridge, TN 37831

325-351. Department of Energy
Technical Information Center
Office of Information Services
PO Box 62
Oak Ridge, TN 37831